

2013

Application Of Nano-Imprint Lithography For Next Generation Carbon Nanotube-Based Devices

Svitlana Fialkova
North Carolina Agricultural and Technical State University

Follow this and additional works at: <https://digital.library.ncat.edu/dissertations>



Part of the [Mechanical Engineering Commons](#), and the [Nanoscience and Nanotechnology Commons](#)

Recommended Citation

Fialkova, Svltana, "Application Of Nano-Imprint Lithography For Next Generation Carbon Nanotube-Based Devices" (2013). *Dissertations*. 139.

<https://digital.library.ncat.edu/dissertations/139>

This Dissertation is brought to you for free and open access by the Electronic Theses and Dissertations at Aggie Digital Collections and Scholarship. It has been accepted for inclusion in Dissertations by an authorized administrator of Aggie Digital Collections and Scholarship. For more information, please contact iyanna@ncat.edu.

Application of Nano-Imprint Lithography for
Next Generation Carbon Nanotube-based Devices.

Svitlana Fialkova

North Carolina A&T State University

A dissertation submitted to the graduate faculty
in partial fulfillment of the requirements for the degree of

DOCTOR OF PHILOSOPHY

Department: Mechanical Engineering

Major: Mechanical Engineering

Major Professor: Dr. Jagannathar Sankar

Greensboro, North Carolina

2013

School of Graduate Studies
North Carolina Agricultural and Technical State University
This is to certify that the Doctoral Dissertation of

Svitlana Fialkova

has met the dissertation requirements of
North Carolina Agricultural and Technical State University

Greensboro, North Carolina
2013

Approved by:

Dr. Jagannathan Sankar
Major Professor

Dr. Sergey Yarmolenko
Major Research Advisor
Committee Member

Dr. Dhananjay Kumar
Committee Member

Dr. Salil Desai
Committee Member

Dr. Yeoheung Yun
Committee Member

Dr. Samuel Owusu-Ofori
Department Chairperson

Dr. Sanjiv Sarin
Dean, Graduate School

© Copyright by
Svitlana Fialkova
2013

Biographical Sketch

Svitlana Fialkova was born on March 9, 1972, in Kharkiv, Ukraine. She received a Master of Science degree in Chemistry (with honor) from Karazin Kharkiv National University (Ukraine) in June 1994. During her student years in Ukraine, she worked as a part-time laboratory technician and then as an engineer at the Research Institute of Chemistry at Kharkiv National University. Her research resulted in two scientific publications. Svitlana has impressive industrial experience, having worked as a quality engineer and manager in the food, pharmaceutical and information technology industries. Her employment record includes international corporations such as JSC Philip Morris Ukraine, Arterium and Validio LLC.

Svitlana joined the MS program in Mechanical Engineering at North Carolina Agricultural and Technical State University in August 2007. She successfully completed MS program in December 2009 with the thesis topic “Magnetron Sputtering Deposition of Thin Films Catalytic Surfaces for Carbon Nanotubes Growth”. She continued her research work on catalyst surface modifications while pursuing PhD degree Mechanical Engineering since January 2010. Svitlana works in a close collaboration with the research group of University of Cincinnati and General Nano LLC.

Dedication

I dedicate this doctoral dissertation to my family.

Acknowledgments

I would like to express my sincere gratitude to my advisors: Dr. Sergey Yarmolenko, for his invaluable supervision and help, comments and suggestions, and critical reviews during this research and Dr. Jagannathan Sankar for his and continued financial support of my Ph.D. program. I truly appreciated the assistance, support, and cooperation I had received from the great research team: Dr. Mark Schulz and Dr. Vesselin Shanov, and their student Arvind Krishnaswamy (University of Cincinnati) and Lucy Lee and Joe Springfield (General Nano LLC).

I would like to thank my committee members Dr. Dhananjay Kumar, Dr. Salil Desai, and Dr. Yeoheung Yun for their invaluable assistance, support, and contribution towards the success of this research. I truly appreciate all the guidance and support I received from them throughout my graduate studies.

Friends: I am also grateful for the help and support from my lab-mates and friends: Dr. Suhaila Abdalla, Dr. Sudir Nareela and Ruben Kotoka and the student body of ERC-RBM: Leon White and Chris Smith.

I am grateful to National Science Foundation Engineering Research Center for Revolutionizing Metallic Biomaterials (ERC-RMB) and Office of Naval Research for funding our research project.

Finally and most importantly, I would like to express my heartfelt thanks to my family for their support, patience, sacrifice, and love.

Table of Contents

List of Figures	x
List of Tables	xvi
Abstract	2
CHAPTER 1. Introduction.....	3
1.1 Recent Advances in Nanotechnology and Nano-devices	3
1.2 Industrial, Research and Economical Needs for Nano-sensors	4
1.3 Research Rationale and Benefits	8
1.4 Research Objectives and Goals	12
1.5 Dissertation Layout.....	12
CHAPTER 2. Theoretical Background and Literature Review	14
2.1 Nano-sensors	14
2.2 Carbon Nanotubes	16
2.2.1 Structure of carbon nanotubes.	17
2.2.2 Synthesis of carbon nanotubes.....	19
2.2.3 Characterization of carbon nanotubes.....	19
2.2.4 CNT biosensors.....	20
2.3 Magnetron Sputtering	25
2.3.1 RF sputtering.....	26
2.3.2 DC sputtering.....	27
2.3.3 Pulsed DC sputtering.	28

2.4 Nano-Imprint Lithography	29
2.4.1 Thermal NIL.	32
2.4.1.1 Thermal resists materials.	33
2.4.1.2 Process parameters of thermal NIL.....	38
2.5 Reactive Ion Etching	41
2.6 Chemical Vapor Deposition	41
CHAPTER 3. Materials, Manufacturing and Characterisation Techniques	43
3.1 Magnetron Sputtering Deposition System.....	43
3.2 Nano-Imprint Lithography	45
3.3 Chemical Vapor Deposition	45
3.4 Structural Characterization Techniques.....	47
3.4.1 Film thickness measurement.....	47
3.4.2 Crystal structure characterization.	48
3.4.3 Scanning electron microscopy and energy dispersive X-ray.....	49
3.4.4 Surface morphology characterization.	51
3.5 Carbon Nanotubes characterisation.....	52
3.5.1 Raman Spectroscopy.....	52
CHAPTER 4. Results and Discussion	56
4.1 Optimization of Magnetron Sputtering Deposition Parameters	56
4.1.1 Deposition rates.	56

4.1.2 Structural characterization of deposited films.	58
4.1.2.1 Phase composition of alumina films.	59
4.1.2.2 Surface topology of alumina films.....	59
4.1.2.3 Catalyst deposition.....	63
4.2 Optimization of Nano-Imprint Lithography Parameters	66
4.2.1 Spin-coating optimization.....	66
4.2.2 Stamp cleaning and release agent deposition.....	67
4.2.3 Imprint time and temperature optimization.	69
4.3.2.1 Effect of thermal resist type and stamp geometry on imprint quality.....	73
4.3.2.1 Effect of alumina layer on imprint quality.....	77
4.3 Optimization of Reactive Plasma Etching.....	78
4.4 Optimization of Lift- off Procedure.....	80
4.5 Three Process Approaches to Pattern Catalytic Surface	82
4.5.1 Overview of 3 process approaches.	82
4.5.1 Approach 1.....	82
4.5.2 Approach 2.....	83
4.5.3 Approach 3.....	84
4.6 Carbon Nanotube Grown on Patterned Catalyst.....	86
4.6.1 Synthesis of CNT patterns.	86
4.6.2 Characterization of CNT patterns.	89

CHAPTER 5. Conclusions and Future Work	94
5.1 Conclusions	94
5.2 Recommendations for Future Research.....	95
References.....	96
Appendix A.....	107
Appendix B.....	109
Appendix C.....	110
Appendix D.....	111

List of Figures

<i>Figure 1.1.</i> Trends in CNT research and commercialization. Journal publications and issued worldwide patents per year, along with estimated annual production capacity.	6
<i>Figure 1.2.</i> Market revenues for CNT of year 2008.	7
<i>Figure 1.3.</i> Industrial application of CNT materials.	8
<i>Figure 1.4.</i> Vertically aligned CNT arrays on a substrate patterned with optical lithography.	10
<i>Figure 1.5.</i> The aligned nano-scale tubular carbon arrays (a –c), and d) - their fabrication process.	10
<i>Figure 1.6.</i> Dimensions correspondence between biological objects and manmade nanomaterials.	11
<i>Figure 2.1.</i> The 2D graphene sheet. The diagram is constructed for $(n,m) = (4,2)$	17
<i>Figure 2.2.</i> Sketches of three different SWNT structures that are examples of (a) a zig-zag-type nanotube, (b) an armchair-type nanotube, (c) a helical nanotube.	18
<i>Figure 2.3.</i> Schematic picture of two electrodes connecting a semiconducting SWCNT with GOD enzymes immobilized on its surface.	21
<i>Figure 2.4.</i> Schematic Schematic diagram showing (a) CNT fiber based glucose biosensor, (b) CNT bundles, (c) DWNT and (d) working principle of biosensor.	23
<i>Figure 2.5.</i> Schematic surface functionalization of CNT (or QD) with oligonucleotide/Angibody (Ab), forming CNT-DNA (or -Ab) probe and QD-DNA (or-Ab) probe, and subsequent addition.	24
<i>Figure 2.6.</i> Patterned CNT arrays and their emission characteristic.	25
<i>Figure 2.7.</i> The schematic of the typical magnetron sputtering system.	27

<i>Figure 2.8.</i> Schematics of imprint techniques.	31
<i>Figure 2.9.</i> Imprint process diagram.....	33
<i>Figure 2.10.</i> Mechanical resistance to deformation as a function of the temperature for an amorphous polymer.	35
<i>Figure 2.11.</i> Temperature dependent shift factor, compared to literature data.	36
<i>Figure 2.12.</i> Geometrical definitions used for the description of the flow process for a stamp with line cavities and protrusions. (a) before molding, (b) after de-molding.	39
<i>Figure 3.1.</i> AJA International ATC 1800F Magnetron Sputtering system at NCAT (a), and internal view of plasma, guns and heated substrate (b).	43
<i>Figure 3.2.</i> Nanonex 2000 imprint system at NCAT (a), and sample holder (b).	45
<i>Figure 3.3.</i> The EasyTube™ 3000EXT system Sputtering system at General Nano LLC: (a) –overall view and (b) – inside quartz reactor.	46
<i>Figure 3.4.</i> XRR data fitting with the LEPTOS software.....	48
<i>Figure 3.5.</i> Bruker AXS D8 Discover XRD machine at NCAT.	49
<i>Figure 3.6.</i> Diagram of detectors used in Hitachi SU8000 FE-SEM.	50
<i>Figure 3.7.</i> NT-MDT NTEGRA platform atomic force microscope at NCAT.....	52
<i>Figure 3.8.</i> Raman spectra from a metallic (top) and a semiconducting (bottom) SWNT at the single nanotube level.....	54
<i>Figure 3.9.</i> Curve fit with band combination for the first-order Raman spectra ($\lambda_0 =$ at 514 nm).	54
<i>Figure 4.1.</i> Energy dispersion X-ray spectroscopy for Al ₂ O ₃ deposited from Al target by reactive PDC deposition at 100Watts, 2mTorr with O ₂ content 10%.	57

<i>Figure 4.2.</i> XRD diffraction patterns of alumina deposited by: (a) RF sputtering and (b) Pulsed DC sputtering.	59
<i>Figure 4.3.</i> SEM images of alumina films deposited by Pulsed DC sputtering at working pressures: a)-d) 2 mTorr and e)-h) 4 mTorr.....	60
<i>Figure 4.4.</i> AFM study of alumina films deposited by Pulsed DC sputtering at working pressure 2 mTorr, a) at room temperature, and substrate heating at: b) 200°C, c) 400 °C and d) 600 °C.	61
<i>Figure 4.5.</i> AFM study of alumina films deposited by Pulsed DC sputtering at working pressure 4 mTorr, a) at room temperature, and substrate heating at: b) 200°C, c) 400 °C and d) 600 °C.	62
<i>Figure 4.6.</i> Roughness of alumina films studied by AFM: a) deposited by RF sputtering; b) deposited by reactive pulsed DC sputtering.	63
<i>Figure 4.7.</i> AFM study of catalyst deposition. DC sputtering at working pressures a) 1 mTorr b) 2 mTorr, c) 4 mTorr, and d) 6 mTorr; and deposited with substrate bias at: e) 1 mTorr f) 2 mTorr, g) 4 mTorr, and h) 6 mTorr.....	64
<i>Figure 4.8.</i> AFM particles analysis of deposited catalyst.....	65
<i>Figure 4.9.</i> Catalyst size (a), and density (b) at different deposition pressure.	65
<i>Figure 4.10.</i> Spin-curves for NRX1025 thermal resist from Nanonex.....	67
<i>Figure 4.11.</i> Spin-curves for PMMA mr-I 35k thermal resist.....	67
<i>Figure 4.12.</i> Setup for vacuum deposition of mold release agent.	68
<i>Figure 4.13.</i> Drops of DI water on pieces of silicon before and after 5, 10 and 15 minutes of deposition of release agent.	69
<i>Figure 4.14.</i> AFM study of imprint patterns on silica substrate.	70

<i>Figure 4.15.</i> Calculation of PMMA viscosity using WLF model.	71
<i>Figure 4.16.</i> Model of residual layer thickness change during imprint of PMMA resist with the lines stamp at different temperature regimes.	71
<i>Figure 4.17.</i> Model of residual layer thickness change during imprint of PMMA resist with the post stamp at different temperature regimes.	71
<i>Figure 4.18.</i> Model of residual layer thickness change during imprint of PMMA resist with the stamp with holes at different temperature regimes (model and measured data).....	72
<i>Figure 4.19.</i> AFM studies of PMMA imprint optimization.	73
<i>Figure 4.20.</i> Imprint patterns on silica substrate with the 70 nm line stamp: a), b) – low and high magnification of NRX1025 2.5% resist and (c), (d) –PMMA resist.	74
<i>Figure 4.21.</i> Imprint patterns on silica substrate with the NSPP33 stamp: SEM image of two imprint areas 5x5 mm, (a) holes from posts and (b) –lines replication, (c) and (d) – AFM images of holes and lines.	75
<i>Figure 4.22.</i> Imprint patterns on silica substrate with the stamp features 20nm, imprint areas 30x30 microns: (a -c) SEM images (d-f) – AFM study of imprinted pattern.....	76
<i>Figure 4.23.</i> Imprint patterns for PMMA resist with the 100nm lines stamp on: a), b) Silica substrate and c), d) substrate with the alumina layer of 10 nm.	77
<i>Figure 4.24.</i> Plasma etching rates for NRX1025: a) effect of plasma power b) effect of oxygen content.	78
<i>Figure 4.25.</i> Plasma etching rates for PMMA.....	79
<i>Figure 4.26.</i> AFM study of plasma etching effect.....	79
<i>Figure 4.27.</i> SEM study of plasma etching effect a) imprinted; b) etched at for 5 minutes; c) etched for 8 minutes.....	80

<i>Figure 4.28.</i> SEM study of lift-off process a) imprinted; b) ammonia solvent; c) ultrasonic and d) wipe-off methods.	81
<i>Figure 4.29.</i> Schematic of three process approaches.....	82
<i>Figure 4.30.</i> Imprinted substrate (a) and (b) catalyst pattern made by first approach.....	83
<i>Figure 4.31.</i> Imprinted substrate (a) and (b) catalyst pattern made by second approach.	84
<i>Figure 4.32.</i> The catalyst patterns: a) imprint with the line stamp (70 nm, 143 nm period); b) imprint with the post stamp (160 nm, 500 nm period).	85
<i>Figure 4.33.</i> Schematic of lift-of (separation) process for approach 3.	86
<i>Figure 4.34.</i> CNTs on 70nm lines: a) – side view; b) – top view.....	86
<i>Figure 4.35.</i> SEM images of short CNTs arrays fabricated by first approach with the catalyst patterned by stamp with holes of 290 nm diameter.	87
<i>Figure 4.36.</i> SEM images of short CNTs arrays fabricated by first approach with the catalyst patterned by stamp with lines of 500 nm width.....	87
<i>Figure 4.37.</i> SEM images of short CNTs arrays fabricated by second approach with the catalyst patterned by stamp with dots of 160 nm diameter.....	87
<i>Figure 4.38.</i> SEM images of long CNTs arrays fabricated by first approach with the catalyst patterned by stamp with lines of 70 nm width, 140 nm pattern period.	88
<i>Figure 4.39.</i> SEM images of long CNTs arrays fabricated by second approach with the catalyst patterned by stamp with lines of 455 nm width, 843 nm pattern period.	88
<i>Figure 4.40.</i> HR-SEM images of individual CNTs.	89
<i>Figure 4.41.</i> Raman spectra of reference and patterned CNT arrays.	90
<i>Figure 4.42.</i> SEM (a) and AFM (b) images of CNT pattern.	90

<i>Figure 4.43.</i> STM scan of CNT pattern a) height mode; b) I-low mode and C) I-profile on a scan.....	91
<i>Figure 4.44.</i> Carbon atoms on a single CNT scan.....	92

List of Tables

Table 2.1. <i>Various of lithographic patterning techniques, practical and theoretical resolution limits.</i>	31
Table 2.2. <i>Common resist materials for thermal NIL.</i>	37
Table 3.1. <i>First-order Raman bands and vibrational modes.</i>	55
Table 4.1. <i>Deposition rates measured by XRR technique.</i>	58
Table 4.2. <i>Imprint process parameters.</i>	72
Table 4.3. <i>Summary of three process approaches.</i>	93

Abstract

This research report addresses the development of 3D carbon nanostructures that can provide unique capabilities for manufacturing carbon nanotube (CNT) electronic components, electrochemical probes, biosensors and tissue scaffolds. The shaped CNT arrays were grown on patterned catalytic substrate by chemical vapor deposition (CVD) method. The new fabrication process for catalyst patterning based on combination of nano-imprint lithography (NIL), magnetron sputtering and reactive etching techniques was proposed and studied. The optimal process parameters for each technique were evaluated.

The catalyst was made by deposition of Fe and Co nanoparticles over alumina support layer on Si/SiO₂ substrate. The metal particles were deposited using direct current (DC) magnetron sputtering technique, with the particles size from 6 nm to 12 nm and density from 70 to 1000 particles/micron². Alumina layer was deposited by radio frequency (RF) and reactive pulsed DC sputtering, and the effect of sputtering parameters on surface roughness was studied. The pattern was developed by thermal NIL using Si master-molds and PMMA and NRX1025 polymers as a thermal resists. Catalyst patterns of lines, dots and holes ranging from 70 nm to 500 nm were produced and characterized by scanning electron microscopy (SEM) and atomic force microscopies (AFM).

Vertically aligned CNTs were successfully grown on patterned catalyst and their quality was evaluated by SEM and micro-Raman. The results confirm that the new fabrication process has ability to control the size and shape of CNT arrays without loss of their quality.

CHAPTER 1

Introduction

This chapter provides with a brief overview of recent advances in nano-technology and nano-devices, focusing on carbon nanotubes and their applications. The research objectives, and the rational and benefits of this work have been elaborated in the next two sections. The chapter concludes with a brief description of the layout of the dissertation.

1.1 Recent Advances in Nanotechnology and Nano-devices

Coming to 21st century, the prefix “nano-“overflow the scientific titles and media news. The exciting discoveries of previous era provide us with the tools to observe and manipulate with matter on atomic level as in nature. Hereby, someone can define the “nanotechnology” as the creation and utilization of materials, devices and systems through the manipulation of matter at scales of less than 100 nanometers. In a nut shell nanotechnology represents a very broad area and is composed of three main fields, i.e. nano-materials, nano-tools and nano-devices. So far, the only nano-materials area was developed in nano-science and achieved a significant level of commercialization. The first consumer products containing manufactured nanoparticles have approached market shelves in millennium. Early studies show a wide array of goods and items with nanomaterial ingredients, including several personal care products like cosmetics, sunscreens, and other daily products. Advances in nanotechnology have indeed revolutionized our thinking from science and research concepts to engineering and business perspectives. Nowadays nanotechnology is addressing unmet needs in the bio-, medical and pharmaceutical sectors. Nanotechnology for biotechnological products and pharmaceutical applications has progressed from the stage of concept development to commercialization. The development of a wide spectrum of nano-scale materials: nano-particles, wires, arrays and quantum dots; and

technologies is changing the basis of disease diagnosis, treatment, and prevention. Furthermore, the recent scientific and engineering community became more focused on nano- materials and technologies that are capable of targeting different cells and specific cellular elements in the body to deliver drugs, genetic materials, and diagnostic agents.

Research into novel biosensors for use in healthcare and related fields continues unabated and several university groups, particularly in the US, are starting to combine nanotechnology with various bio-sensing techniques to develop the so-called “nano-biosensors”. This strategy is seen by many researchers as the key to yielding devices that exhibit rapid responses combined with very high sensitivity. Indeed, these features have become standard attributes of this technological combination and arise principally from the exceedingly small size and high surface areas of nanostructures such as nanoparticles, nanotubes and nanowires (Rahman et al., 2009; Roy & Gao, 2009; Zhang et al., 2009). Some of these nano-biosensor projects are aimed at potentially high volume applications in the public health sector, where markets could be significant, whilst others aim to improve on existing clinical practices by allowing the more rapid detection and quantification of viruses and bacteria. After glucose sensors, “gene chip” or “DNA chip” microarrays probably represent the largest sector of today’s biosensor market: an experiment conducted with a single-DNA chip can provide researchers with information on thousands of genes simultaneously – a dramatic increase over earlier techniques (Bogue, 2005).

1.2 Industrial, Research and Economical Needs for Nano-sensors

Nanotechnology, which is defined as the application of nano-science in technological devices, processes and products, is fast emerging and enabling technology capable of impacting almost all the sectors including human health, industries and consumer products. Therefore, all governing bodies and industries over the world are investing in the development of

nanotechnology based processes, products and systems. Managing the introduction of nanotechnologies by both industry and government is becoming more and more typical as greater numbers of parties have shown interests in the economic, social, and environmental outcomes. Thus, the US Federal Budget for 2013 provided \$1.8 billion for the National Nanotechnology Initiative (NNI), reflecting steady growth in the NNI investment. The cumulative NNI investment since fiscal year 2001, including the 2013 request, now totals over \$18 billion. Cumulative investments in nanotechnology-related environmental, health, and safety research since 2005 now total nearly \$650 million. Cumulative investments in education and in research on ethical, legal, and other societal dimensions of nanotechnology since 2005 total more than \$350 million (*National Nanotechnology Initiative's Budget Brief for FY 2013*). The importance of economic, environmental and ethical aspects of nanotechnology reflected in US Federal Budget for next year: according to NNI (*Supplement to the President's 2014 Budget Request, 2013*) :

“The President’s 2014 Budget provides over \$1.7 billion for the National Nanotechnology Initiative, a sustained investment in support of the President’s priorities and innovation strategy. Cumulatively totaling almost \$20 billion since the inception of the NNI in 2001 (including the 2014 request), this support reflects nanotechnology’s potential to significantly improve our fundamental understanding and control of matter at the nano-scale and to translate that knowledge into solutions to critical national issues. NNI research efforts are guided by two strategic documents developed by the Nanoscale Science, Engineering, and Technology (NSET) Subcommittee of the National Science and Technology Council (NSTC), the 2011 NNI Strategic Plan and the 2011 NNI Environmental, Health, and Safety Research Strategy.”

One of the biggest player on nano-technology market and the most promising nano-material is carbon, shaped in single- and multi-walled tubes and graphene sheets. The latest review by Hart et al. (2013a) shows how competitive the area of carbon nanomaterials research: the number of scientific publications grown 3 times for the past 6 years, the same trend is observed with the production capacity of CNT. However, the number patents have a steady but slow growth compare to the publications and the reported production capacity is only 50% of estimated, which indicates how challenging the commercialization process of nanotechnologies, particularly CNT commercialization (Figure 1.1).

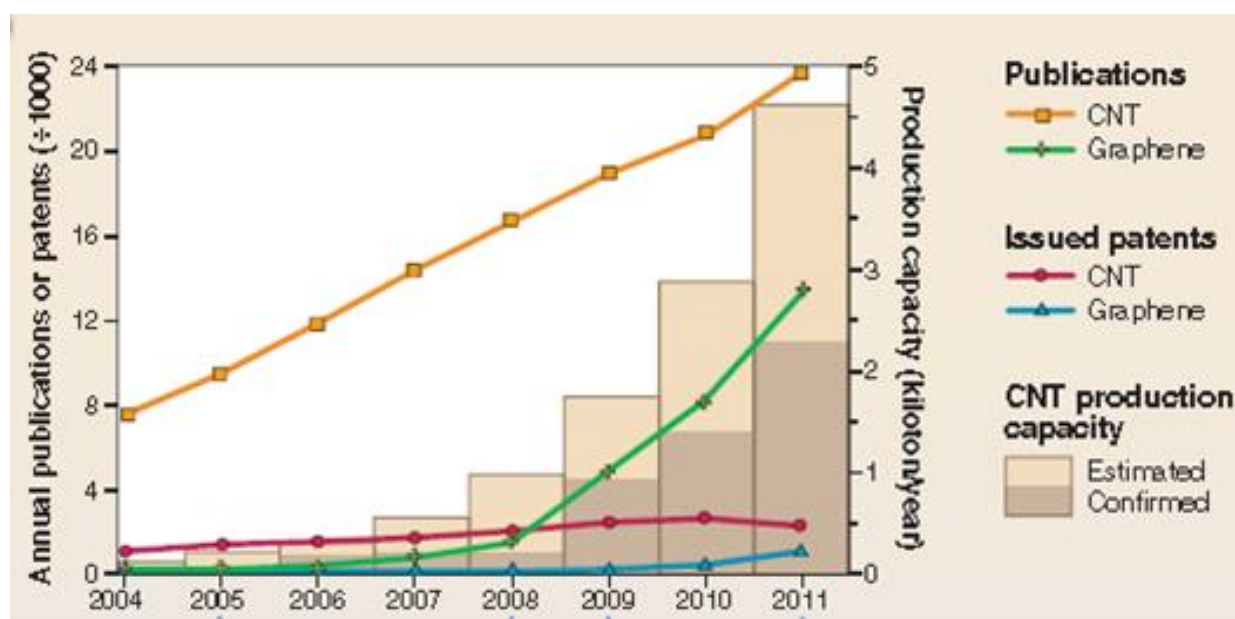


Figure 1.1. Trends in CNT research and commercialization. Journal publications and issued worldwide patents per year, along with estimated annual production capacity.

According to press reports, many companies are investing in diverse applications of CNTs, such as transparent conductors, thermal interfaces, antiballistic vests, and wind turbine blades (Figure 1.3) However, the companies tend to keep technical details as a trade secret for a very long time after commercialization, which makes it challenging to predict market success and unlikely attracts the majority of investors who are considering it as a high-risk market.

Hence, the increases in nanotube production capacity and sales are an especially important metric for emerging CNT applications. Further industrial development demands health and safety standards for CNT manufacturing and use, along with improved quantitative characterization methods that can be implemented in production processes. So far the biggest success in commercialization of CNT materials was achieved in defense, electronics and transport industries (Figure 1.2). Contrary, time the healthcare and pharmaceutical industries have long-term cycle of product development due to strict FDA regulation, so in a next decade someone could expect the economic boost of CNT products in those market sections.

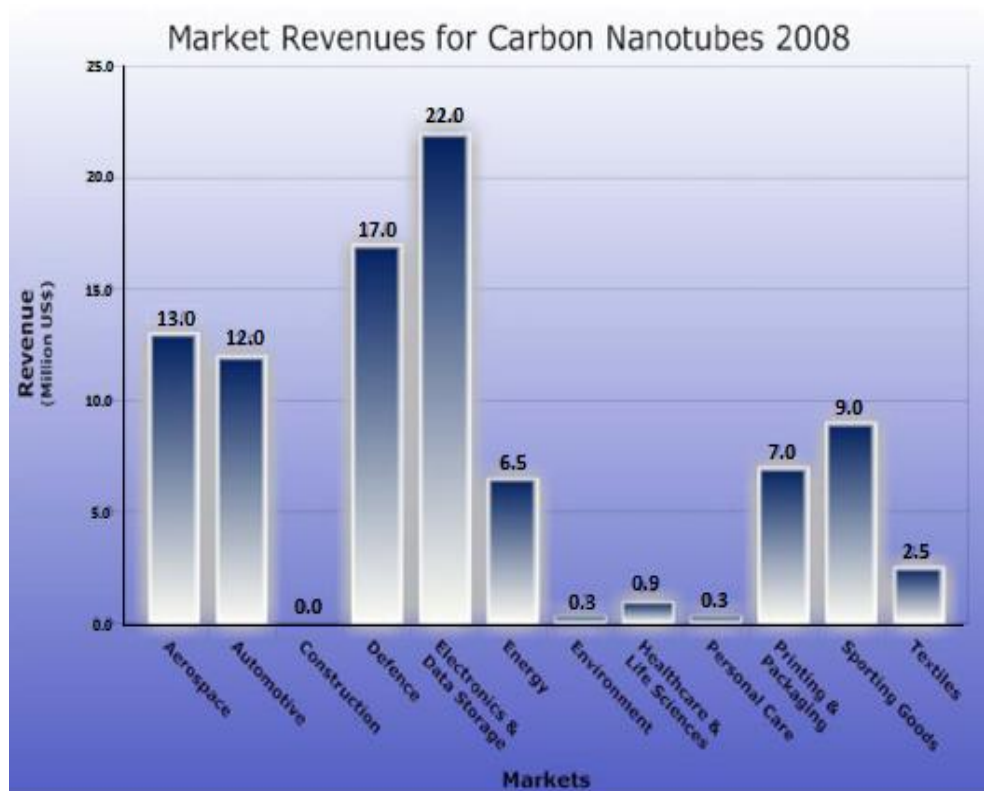


Figure 1.2. Market revenues for CNT of year 2008. ("Research and Markets Adds Report: Global Carbon Nanotube Market 2011-2015," 2012)

as forests and yarns are beginning to bridge the gap between the nano-scale properties of CNTs and the length scales of bulk engineering materials. However, the properties of CNT yarns and sheets, like thermal conductivity and mechanical strength, remain far lower than the properties of individual CNTs, so the placement of individual CNTs having desired structure with lithographic precision over large substrates would be a breakthrough for electronic devices. So far, the several successful attempts were achieved in controlling the size and location of CNT arrays at micro-level: Y. H. Yun et al. (2005) reported on MWCNT towel electrochemical actuator, then using optical lithography method his group developed a high-sensitive electrode with the size of 100 microns (Figure 1.4) and used it for cancer cell detection (Y. Yun et al., 2006; Y. Yun et al., 2007). The approach to pattern the catalyst on a substrate and then synthesize CNT was used by (Yin et al., 2009). The CNT arrays were prepared by the pyrolysis of iron phthalocyanine on the patterned by UV NIL substrates, the lateral dimension of arrays were 20 microns. The similar results were obtained by (Hart et al., 2012, 2013b): the aligned CNT arrays were synthesized on patterned substrate and post-processed with organic solvent to shrink and improve aligning within individual bundle of CNTs.

Recently, the 3D carbon nanostructures with the sizes below 1 micron were fabricated. Thus, a vertically formed and hexagonally aligned nano-scale tubular carbon array was fabricated through carbon deposition inside an anodic aluminum oxide nano-template, followed by controlled chemical etching of the alumina layer Figure 1.5. The obtained nano-scale carbon pillars with their controlled diameters, down to 25nm, and protruded lengths of 100nm were successfully used as a master-mold for UV-NIL. (Kim et al., 2008)

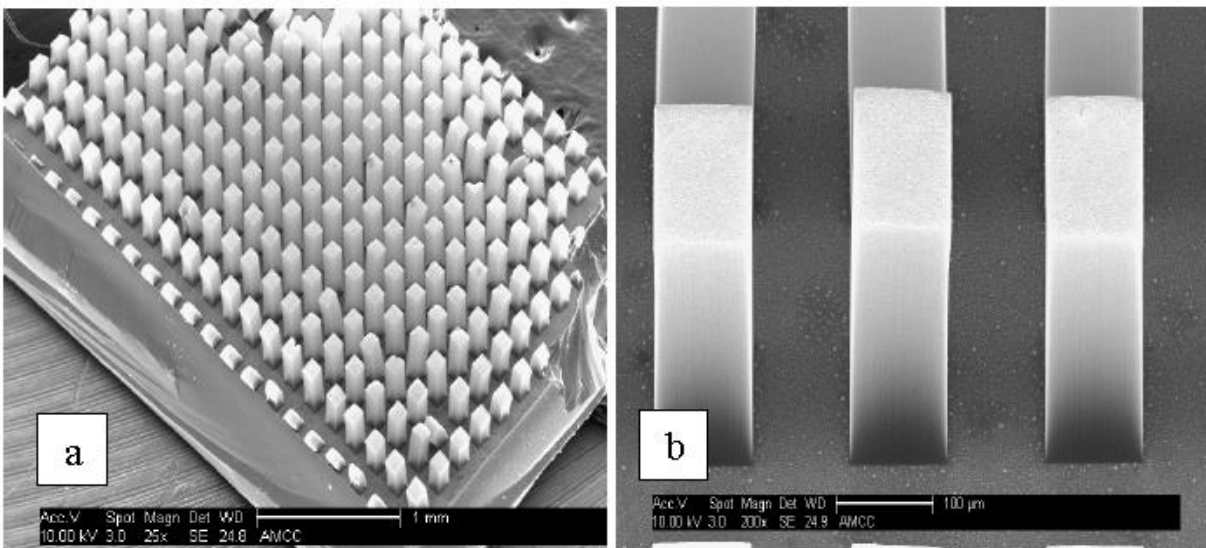


Figure 1.4. Vertically aligned CNT arrays on a substrate patterned with optical lithography (Y. H. Yun et al. (2005).

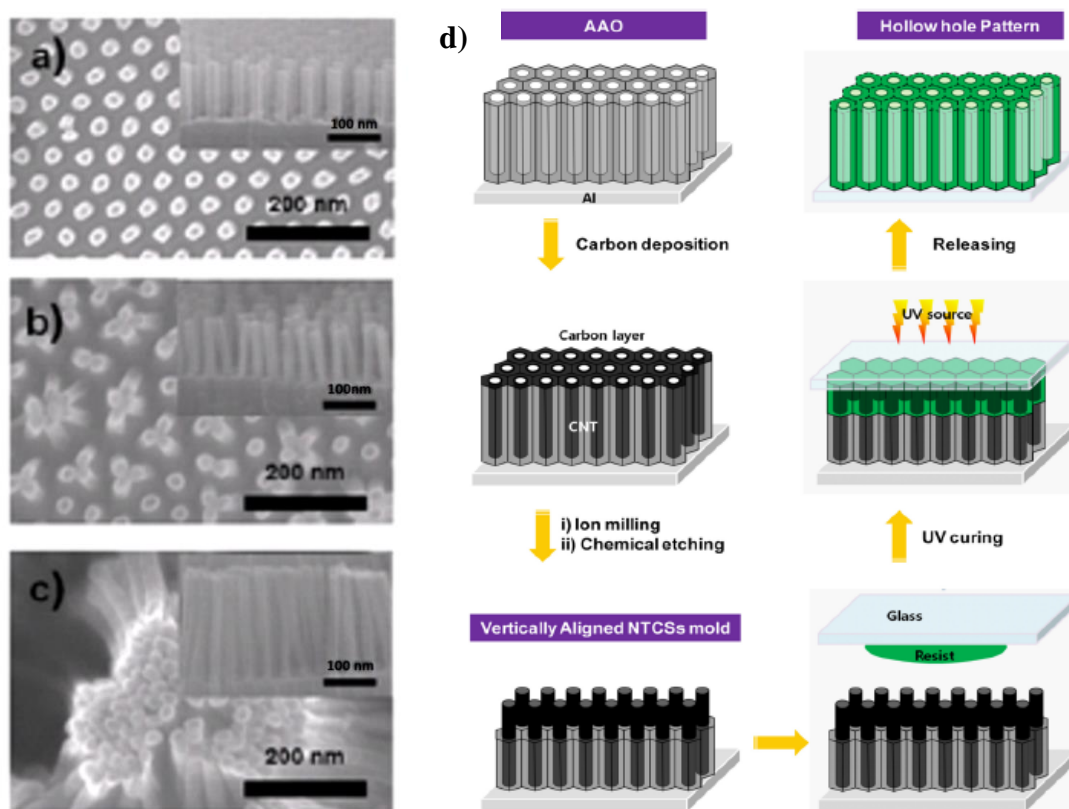


Figure 1.5. The aligned nano-scale tubular carbon arrays (a –c), and d) - their fabrication process (Kim et al., 2008)

Ongoing interest in CNTs as components of biosensors and medical devices is motivated by the dimensional and chemical compatibility of CNTs with biomolecules, such as DNA and proteins (Figure 1.6). At the same time, CNTs unique mechanical, electrical, thermal and optical properties enable fluorescent and photo-acoustic imaging, as well as localized heating using near-infrared radiation (Allen et al., 2007; Minot et al., 2007; Muguruma & Kase, 2006; Pumera et al., 2007) . SWNT biosensors can exhibit large changes in electrical impedance and optical properties in response to the surrounding environment (Chen et al., 2003; Choong et al., 2009; Gao et al., 2003; Y. H. Yun et al., 2007). Low detection limits and high selectivity require engineering the CNT surface modification by functional groups and coatings and appropriate sensor design. Similar CNT sensors have been used for gas and toxin detection in the food industry, military, and environmental applications (Arribas et al., 2006; Chowdhury et al., 2009; Trojanowicz, 2006).

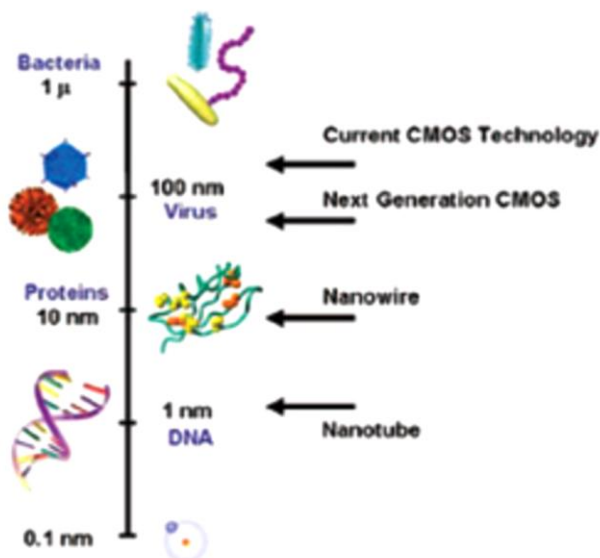


Figure 1.6. Dimensions correspondence between biological objects and manmade nanomaterials (Gruner, 2006).

1.4 Research Objectives and Goals

This research work is aimed to create novel 3D carbon nanotube materials/devices by modifying catalyst surface at nano-level using combination of technologies: Magnetron Sputtering Deposition and Nano Imprint Lithography.

The goals of this research are:

- ✓ Fabricate 3D carbon nanotube-structures with different shapes and patterns within a size range below 1 micron.
- ✓ Develop the process flow of catalyst patterning that will be repeatable and controllable that is included but not limited to optimization of process parameters for applied techniques.
- ✓ Finally, evaluate the different process approaches/flows to determine the best way to scale the lab production to the manufacturing level.

The ability to control the shape and size of catalyst gives a possible solution to manipulate with the shape of CNTs arrays, sizing them to the required dimensions and place them on specified location. The ultimate goal of further research will be controlling individual CNT growth.

1.5 Dissertation Layout

This dissertation has been organized under five chapters. Chapter 1 is dedicated to the introduction of the subject matter and provides a brief analysis of market needs and economic trends in nanotechnology and specifically in nano-sensors development. The main objective and goals of this research work were stated on.

Chapter 2 presents a comprehensive theoretical background of carbon nanotubes properties and examples of their applications as bio-sensors. The relevant theories behind the

Magnetron Sputtering deposition and Nanoimprint Lithography techniques and procedures are provided.

Chapter 3 provides with the detailed description of technology used and equipment available at NC A&T SU and its limitations that need to be considered to succeed in current research. The processes' parameters, experimental methods and sample preparation are described. This is followed by descriptions of all the characterization techniques used in this research.

Chapter 4 presents the results and discussion of experimental techniques used in this research work.

The conclusions and potential future research work are discussed in Chapter 5.

CHAPTER 2

Theoretical Background and Literature Review

This chapter provides the review of recent publications relevant to the carbon nanotube – based devices. The theoretical background of carbon nanotubes properties and applications is provided. The relevant theories behind the Magnetron Sputtering and Nano imprint Lithography and Reactive Plasma Etching techniques and procedures are discussed.

2.1 Nano-sensors

The very first speech about nanotechnology was given by Richard Feynman on December 29th, 1959 to the American Physical Society at California Institute of Technology. In his lecture “There's Plenty of Room at the Bottom” Feynman was amazingly prophetic and he told us to make things “small and smaller” such as the Moore’s law proposed by Gordon Moore in 1965. Among many visionary things, Feynman said in his speech: “What would happen if we could arrange the atoms one by one the way we want them?”. At that time the technology were targeting the micron sizes of matter control, analysis and fabrication. Nowadays, modern materials science has reached ability to synthesize and control materials on the submicron and nanometer scales, as a result novel advanced functional materials with custom properties can be created. When scaled down to a nano-scale, most materials exhibit novel properties that cannot be extrapolated from their bulk behavior. The new scientific and technological development has flourished on interdisciplinary boundary between materials science, molecular biology and nanotechnology.

The latest review by Zhang et al. (2009) provides a comprehensive definition of a biosensor: “ A biosensor is a device incorporating a biological sensing element either intimately connected to or integrated within a transducer. Specific molecular recognition is a fundamental

prerequisite, based on affinity between complementary structures such as enzyme-substrate, antibody-antigen and receptor- hormone, and this property in biosensor is used for the production of concentration–proportional signals. Biosensor’s selectivity and specificity highly depend on biological recognition systems connected to a suitable transducer.”

Interest in the development of new bio-sensing and high-throughput screening technologies has been largely driven by recent developments in two different application areas. The first application area is focused on biomarkers associated with specific disease states and pharmacological responses (Growdon 1999; Sander 2000; Srinivas et al. 2001, 2002). The second broad application area relates to the needs in fast detection and identification of pathogenic threats. Viral detection, like influenza (Dawson et al. 2006; Liu et al. 2006; Lu 2006), adenovirus (McCaman et al. 2001; Gu et al. 2003) and dengue hemorrhagic fever (Guzman and Kouri 2004; Zaytseva et al. 2005) requires the development of new sensors with very low limits of detection. The high specificity, sensitivity and ability to process large volumes of samples are necessity for sensors in environmental and safety control of water- (Straub and Chandler 2003), food- (Rasooly and Herold 2006) or air-borne pathogens (McBride et al. 2003; Stetzenbach et al. 2004). The further development of advanced biosensor expected to bring autonomous and networked systems that will be able to operate with as little or no human interaction. Achieving the new level of required sensors performance and miniaturization has not been possible without development of new nanomaterials with enhanced electrical and optical properties.

Biological molecules possess special structures and functions, and determining how to fully use the structure and function of nanomaterials and biomolecules to fabricate single molecule multifunctional nano-composites, nano-films, and nano-electrodes, is still a great challenge. The mechanism of interaction between biomolecules and nanomaterials is still a

complex problem to solve for current research community. Future work should concentrate on clarifying the mechanism of interaction between nanomaterials and biomolecules on the surface of electrodes or nano-films and using novel properties to fabricate a new generation of biosensors.

2.2 Carbon Nanotubes

Carbon nanotubes are remarkable objects that revolutionized science and boosted the nano-technology development to new level. As a silicon-based technologies changed the world in last century to a new era of information technology and globalization, it is expected that nano-shaped materials (tubes, wires, particles and dots) and their applications will change our life tomorrow's. Current state of art of carbon nanotube science predicts the future development of artificial nerves and muscles, super-strongest lightweight cables, new memory storage devices and others technological marvels(M.S. Dresselhaus & Dai, 2004; Vashist et al., 2011). The excitement of new possibilities brought by discover of CNTs should not overshadow the reality of current technology state and possibility of real application and mass-production, as discussed in Chapter 1. The lesson learned from fullerenes – molecules closely related to nanotubes. The fullerenes, first reported in 1985, the winners of a Nobel Prize in Chemistry in 1996, still a product for science lab and just few applications of fullerenes have reached the market. Thus, the similar enthusiasm about nanotubes should be approached with caution ("Nanotechnology: A Realistic Market Assessment," 2012). However, the expectations from carbon nanotubes are very high, as many believe that nanotube-based technologies are the road-map for further miniaturization microchips and new energy-transfer devices. Carbon nanotubes are considered the new building blocks for further technological progress.

2.2.1 Structure of carbon nanotubes. The simplest way to imagine a carbon nanotube is as a rolled sheet of graphene. Then the tips of the tube are sealed by two caps, each cap being a hemi-fullerene of the appropriate diameter. The geometry of CNT defines their unique properties. First, starting from graphene hexagons which is built from sp^2 -hybridized carbon atoms that are involved in aromatic rings with the C=C bond length 1.42 angstrom. The following terms used to describe geometry and symmetry of CNT: the tubule diameter d_t and the chiral angle θ , chiral vector C_h and the basis vectors a_1 and a_2 of the honeycomb lattice, as pictured in Figure 2.1. The 2D graphene sheet. The diagram is constructed for $(n,m) = (4,2)$ (M. S. Dresselhaus et al., 1995).

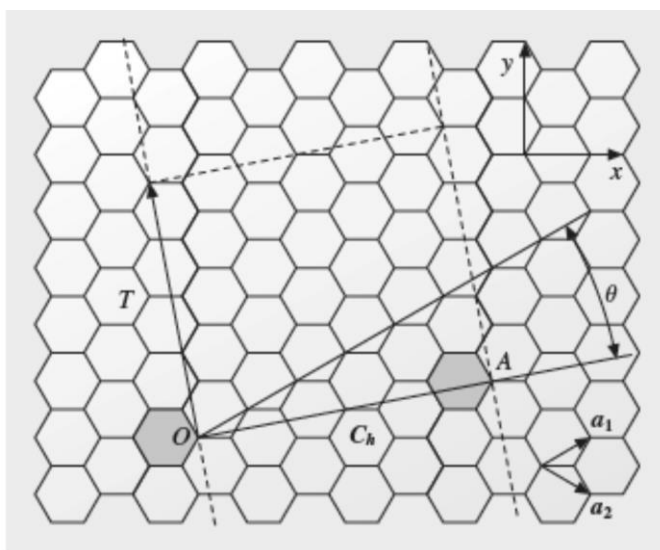


Figure 2.1. The 2D graphene sheet. The diagram is constructed for $(n,m) = (4,2)$ (M. S. Dresselhaus et al., 1995).

The pair of integers (n,m) is used to describe the position of distinct caps (carbon atoms in hexagon) that can be joined continuously to the cylindrical carbon tubule. The integers (n,m) specify chiral vectors C_h (2.1) and uniquely determine the diameter of carbon nanotube d_t and chiral angle θ (2.2).

$$C_h = na_1 + ma_2 \quad (2.1)$$

where a_1 and a_2 are unit vectors with the length $a = \sqrt{3} a_{c-c} = \sqrt{3} * 1.42 = 2.46$ angstrom

$$d_l = \frac{\sqrt{n^2 + m^2 + nm}}{\pi} a \quad (2.2)$$

The length L of the chiral vector C_h is actually a tube circumference and can be calculated from the diameter d_l . The chiral angle θ between the C_h direction and the zigzag direction of the honeycomb lattice $(n,0)$. Since C_h , θ , and d_l are all expressed as a function of the integers n and m , they are sufficient to define any particular SWNT by denoting them (n, m) . The values of n and m for a given SWNT can be simply obtained by counting the number of hexagons that separate the extremities of the C_h vector following the unit vector a_1 first and then a_2 . The same way as lattice vectors in crystals (hkl) are used for symmetry description, the lattice vectors (n, m) describe the symmetry type of nanotubes (zigzag, armchair or chiral tubules) but also used for prediction of the properties of carbon nanotubes: metallic ($n - m = 3p$, where p is an integer) or semiconducting ($n - m = 3p \pm 1$). (M. S. Dresselhaus et al., 2004).

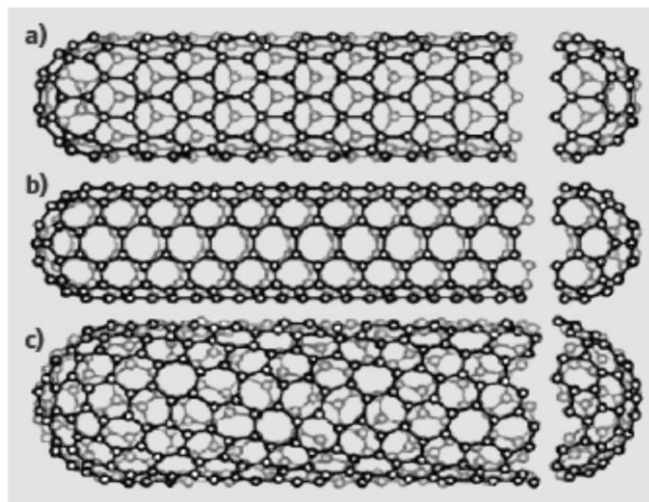


Figure 2.2. Sketches of three different SWNT structures that are examples of (a) a zig-zag-type nanotube, (b) an armchair-type nanotube, (c) a helical nanotube, adapted from (M. S. Dresselhaus et al., 1995).

2.2.2 Synthesis of carbon nanotubes. Conventional atmospheric pressure CVD reactors are frequently used for growing CNT from carbon precursors. There are many modifications of CVD reactors for MWCNT growth on supported catalyst that are reported in the literature (Lamouroux et al., 2007).

Since Iijima (1991) first reported TEM evidence of CNT synthesis in 1991, a huge number of studies has been devoted to the growth process of MWCNT and SWCNT on supported catalytic surfaces. In spite of the tremendous amount of efforts towards clarification and understanding of the mechanism of catalytic growth of CNTs on supported catalysts, the key problem – how to control diameter, length and density of CNTs arrays is still unsolved. There are several mechanisms of catalytic growth: base and tip growth mechanism (Lamouroux et al., 2007); mixed (Kunadian et al., 2009) and carbon diffusion through a bulk Fe₃C nanoparticle or film (Ago et al., 2000; Pérez-Cabero et al., 2004). It is believed that the key parameters of CVD process that have to be taken into consideration for the control of CNT growth are: the choice of the catalyst, the particle size, the temperature, the composition of the gas phase and the partial pressure of the carbon source. It was quickly found that catalyst material has to be precisely justified together with its geometry (particle size) to achieve repeatable results. Small changes in size (or thickness) of catalyst components (catalyst as well as support material) can have a dramatic influence on CNT growth, though (a) metal or alloy (b) support material and (c) particle size of metallic catalyst have to be selected (Chai et al., 2007; Chai et al., 2009; Chesnokov et al., 2009; Nasibulin et al., 2005; Noda et al., 2006).

2.2.3 Characterization of carbon nanotubes. CNTs are extremely small objects and their characterization requires sophisticated techniques and instruments. The morphology of the CNTs, their dimensions and orientation can be easily revealed using electron microscopes with

high resolution. High resolution FE-SEM and TEM is used for diameter and nanotube morphology. TEM and SEM are routinely used in CNT research, and almost all papers refer to these techniques. Atomic force microscopy (AFM) has been widely used to measure the diameters of individual SWNTs, while low temperature, atomic resolution scanning tunneling microscopy (STM) images can be used to measure the chiral angles of individual SWNTs (Scheerlinck et al.). The STM mode allow to measure voltage-current characteristics (I/V), (dI/dV) for individual SWNTs, thereby yielding scans of the electronic density of states from which the (n, m) indices for individual SWNTs can be determined (M. S. Dresselhaus et al., 2004).

Optical techniques, including optical absorption, photoluminescence, and Raman scattering have been widely used to characterize carbon nanotubes by studying both their electronic and phonon (lattice vibrational) spectra. Micro-Raman spectroscopy is frequently employed to study the quality and chirality of the CNTs. It also provides information about the number of the walls and the presence of crystalline or amorphous carbon, including the inner diameter of the CNTs. The details about Raman spectroscopy of CNTs are provided in section 3.5.

2.2.4 CNT biosensors. The general applications of carbon nanotubes in a modern world were discussed in Chapter 1. This section focused on examples of CNT-based sensors developed in a last decade.

Comparing to the traditional electrodes the CNTs-based ones demonstrate higher sensitivity and shorter response time. The better performance of CNT electrodes can be explained by the efficient capture and electron transfer from analytes due to their one-dimensional hollow tubular nano structure that benefits electrochemical reactions. Furthermore,

the dramatic decrease in the over-potentials of hydrogen peroxide observed at CNT-modified electrodes show great promise for application in the glucose sensing area. Thus, Xu et al. (2004) firstly introduced SWCNTs into field effect transistor bio sensing device. Controlled attachment of glucose oxidase (GOD) to the nanotube sidewall was achieved through a linking molecule, which on one side bonded to the SWCNT through Van der Waals coupling with a pyrene group and on the other side covalently bonded the enzyme through an amide bond, as depicted in Figure 2.3. The groups in the enzyme temporarily change their charge state during a catalytic reaction cycle of redox enzymes, that can be detected by the CNT-electrode. The immobilization of GOD can be observed in real time by step-like response in current-voltage characteristic signal of device. The latest success in glucose sensing belongs to potentiometric glucose biosensor based on a gate field effect transistor, reported by Li et al. (2005). The biosensor was constructed using a SnO₂ sensing thin film on an indium tin oxide/polyethyleneterephthalate substrate, chitosan and a mediator of MWCNTs was used. Meanwhile, GOD was entrapped by 3-glycidoxypropyltrimethoxysilane (3-GPTS) using a one-step simple fabrication. The reported characteristics of the potentiometric glucose biosensor were: output voltage responses were from 150 mV to 200 mV, and the detection linear range was from 100 mg/dL to 300 mg/dL. The biosensor had a 4-day life time and 25-times operational stability.

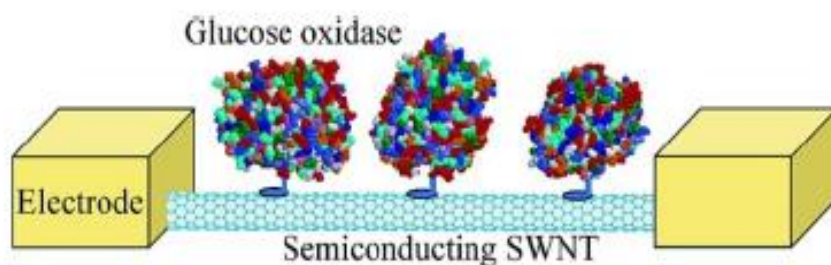


Figure 2.3. Schematic picture of two electrodes connecting a semiconducting SWCNT with GOD enzymes immobilized on its surface (Xu et al., 2004).

Recently, the new CNT-based product become available even in a mass-production: continuous yarns were fabricated from CNT arrays by direct spinning. The common way to produce CNT yarns was to synthesize the CNTs arrays by the CVD process at high temperature, and then to spun into nano-yarns along the fiber axis. Thus the direct spinning of the pure CNT fiber helped to maintain their properties in terms of strength, stiffness, toughness, electrical and thermal conductivities. The CNT micro-fiber obtained by this method can be easily post-processed: functionalized or covered by materials that create a barrier between electrode and host body. Those modifications eliminate toxicity concerns of CNTs and make possible the development of long-term implantable CNT biosensors. A comprehensive study about CVD-synthesized CNT fibers used as sensing electrodes to detect glucose was introduced by Zhu et al. (2010). The specific fiber used was composed of double-walled CNTs that are compacted into concentric layers of CNT bundles organized as nano-yarns, as shown in Figure 2.4. The CNT fiber acts as an electric wire, but because of its' nano-scale surface topography and porosity it can capture and promote electron transfer reactions more efficiently and facilitate molecular-scale interactions with enzymes.

The research group from China (Zhang et al., 2009) reported a highly selective, ultrasensitive, fluorescent detection method for DNA and antigen based on self-assembly of multi-walled carbon nanotubes and CdSe quantum dots (QD) via oligonucleotide hybridization; its principle is shown in Figure 2.5. Multi-walled carbon nanotubes and QDs, their surfaces are functionalized with oligonucleotide (As-ODN) or antibody (Ab), can be assembled into nano-hybrid structures upon the addition of a target complementary oligonucleotide or antigen (Ag). As shown in Figure 2.5 nanomaterial building blocks that vary in chemical composition, size or shape are arranged in space on the basis of their interactions with complementary linking

oligonucleotide. Thus, system 1 presents the formation of CNT-QD hybrid in the presence of complementary DNA target; system 2 allows to detect three different DNA target simultaneously; and system 3 is a CNT-QD protein detection system based on antigen-antibody immunoreactions. The final analysis was conducted by centrifugation separation of unbound QDs probe and monitoring QDs fluorescence intensity by spectrofluorometer. It was shown that oligonucleotide directed assembly strategy could be used to prepare binary assembly materials comprising two different shaped oligonucleotide-functionalized nanomaterials. The reported results suggest that this strategy could be extended to a variety of multicomponent systems.

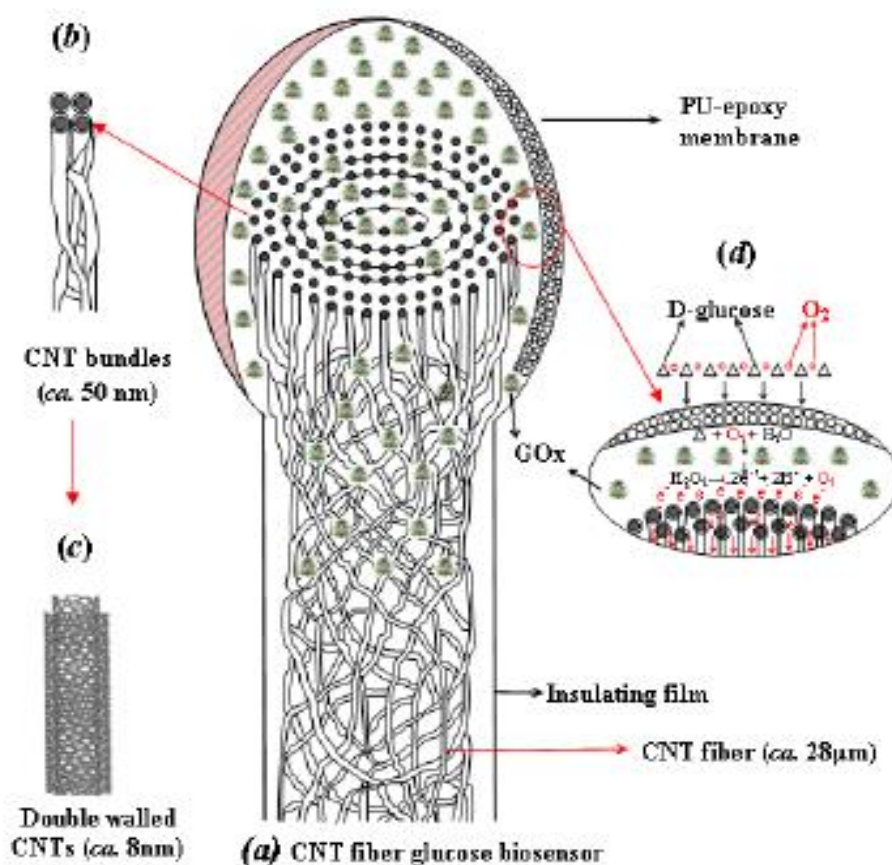


Figure 2.4. Schematic Schematic diagram showing (a) CNT fiber based glucose biosensor, (b) CNT bundles, (c) DWNT and (d) working principle of biosensor (Zhu et al., 2010).

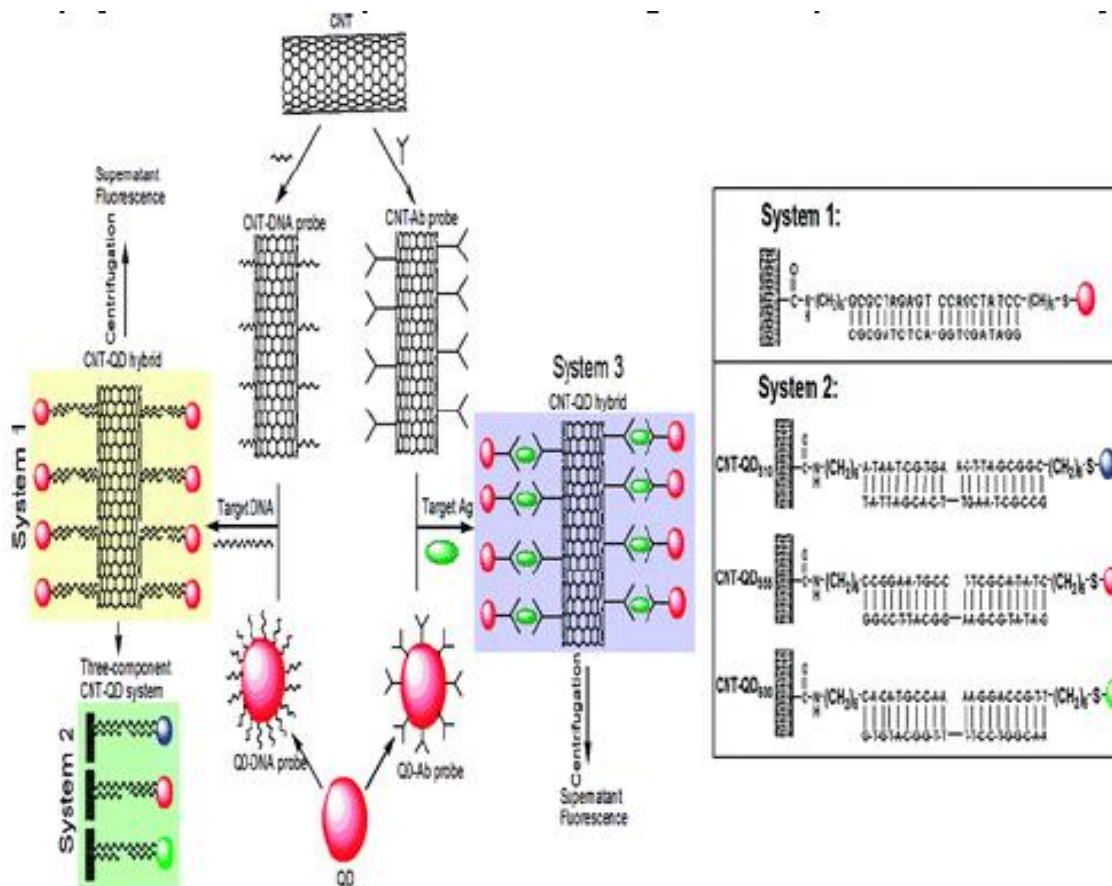


Figure 2.5. Schematic surface functionalization of CNT (or QD) with oligonucleotide/Angibody (Ab), forming CNT-DNA (or -Ab) probe and QD-DNA (or-Ab) probe, and subsequent addition of target oligonucleotide (or Antigen) to form CNT-QD assembly (Zhang et al., 2009).

Field emission device was prepared by (Yin et al., 2009), using one of the approaches this research work is focused on. The CNT- field-emission cathode was prepared on patterned silicon wafer area. To reveal the field-emission properties of the patterned and aligned CNTs as emitters, a conventional diode structure was tested. A sufficient intense electric field is applied to the cathode of CNTs film and the anode of the ITO film with the insulation spacer of polyvinyl film. The fabricated cathode and field emission characterization of the specimen is shown in. The light emission images of electron emission for patterned and aligned CNTs were observed using a green-colored zinc oxide phosphor.

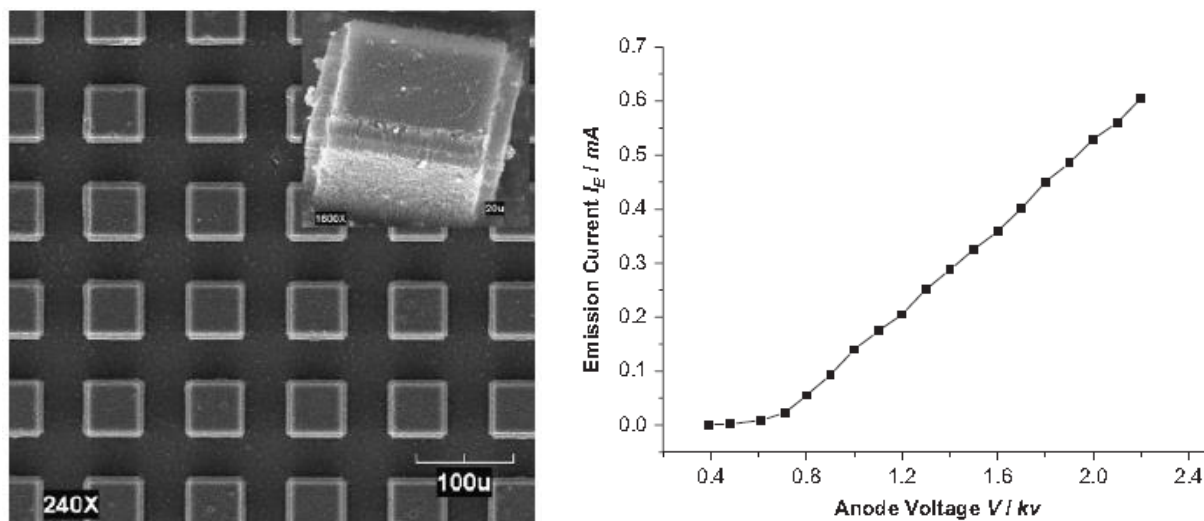


Figure 2.6. Patterned CNT arrays and their emission characteristic (Yin et al., 2009).

The given example of CNT-based devices just a small part of their potential that could be realized in nano-medicine. The other applications of CNTs are: drug-delivery agents (Cevc & Vierl, 2010; Singh et al., 2009), a culture substrate for neural cells (Bitirim et al., 2013) and molecular systems for recognition and targeting tumorous cells (Yang et al., 2007; Zeng et al., 2006).

2.3 Magnetron Sputtering

Sputtering is the ejection of atomized material from a solid target by energetic bombardment of its surface with the ions of sputtering (commonly argon) and/or reactive (oxygen or nitrogen) gas.

The sputtering deposition process involves three main steps that occur on:

- 1) on a target surface – production (ejection) of the appropriate atomic, molecular or ionic species,
- 2) in a medium - transport of ejected species to the substrate,
- 3) on a substrate - condensation and forming a solid film (Wasa, 1992).

Magnetron sputtering uses strong magnetic fields to trap electrons and ionized sputtering gas close to the surface of the target. The substrates for deposition can range from silicon wafers to glass. The typical schematic of modern magnetron sputtering system with different power supplies is presented in Figure 2.7 . The benefits of magnetron sputtering are:

- ✓ high deposition rates;
- ✓ the possibility to deposit several materials simultaneously;
- ✓ large variety of film materials available - nearly all metals and compounds;
- ✓ uniform coating on a large areas;
- ✓ broadly tunable film properties;
- ✓ cost-effective
- ✓ easy to scale-up for industrial application.

The drawbacks of sputtering technology includes: low target utilization; variation of deposition rate of dielectric materials during long-time process; and incorporation of gas molecules into the sputtered films (Ginsburg, 2002(Depla et al., 2006; Depla et al., 2009; Posadowski et al., 2008).

2.3.1 RF sputtering. With radio frequency (RF) sputtering, when an RF potential, with a large peak-to-peak voltage, is capacitively coupled to an electrode, an alternating positive/negative potential appears on the surface. Due to this alternating potential, it is possible to use RF sputtering to sputter electrically insulating materials (Mattox, 2010). RF sputtering also offers advantages in that film depositions can be carried out at low temperatures while yielding preferred orientation and uniform properties (Dang, Fu, Luo, Flewitt, & Milne, 2007). One disadvantage of sputtering dielectric targets using RF sputtering is the generation of large thermal gradients that can fracture or even melt the target if high power levels are used. Large

thermal gradients develop due to electrically insulating materials have poor thermal conductivity (Mattox, 2010).

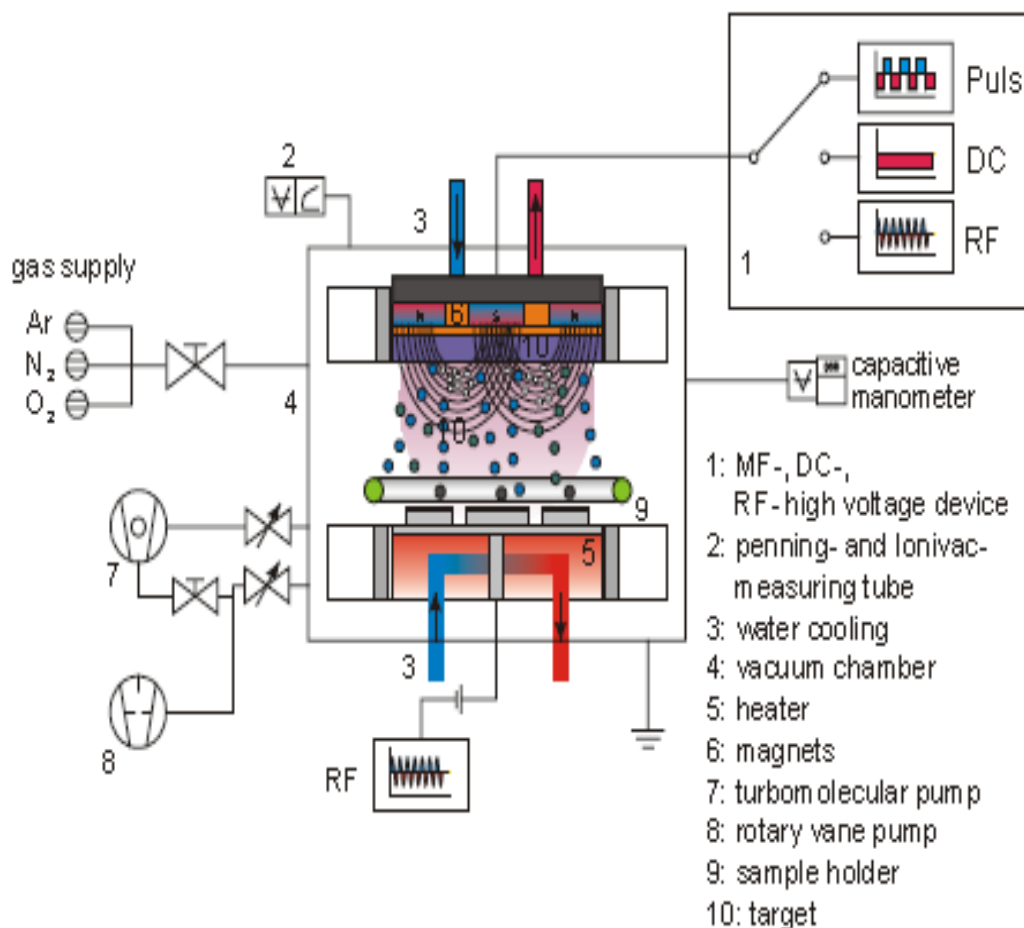


Figure 2.7. The schematic of the typical magnetron sputtering system.

2.3.2 DC sputtering. Direct current (DC) sputtering is a form of material deposition that involves bombarding a target with ionized gas molecules. When the target is bombarded with gas molecules, a displacement of target atoms occurs. These free target atoms adhere to a negatively charged substrate creating a thin film on its surface. DC sputtering technique can be non-reactive or reactive. If a ceramic target is being utilized, to ensure that the resulting film will also be a ceramic, oxygen can be flowed into the system to ensure that the metal ions will react with oxygen to form a ceramic.

Reactive sputtering occurs when a gas is purposely added to the sputtering chamber to react with the sputtered material (Sproul, Christie, & Carter, 2005). The reactive sputtering process can be divided into three modes: (a) metallic, (b) transition and (c) reactive. A typical characteristic of the reactive magnetron sputtering is a low deposition rate of compounds produced in the reactive mode compared to that of the pure metallic films produced in the metallic mode. The decrease in deposition rate of films sputtered in the reactive mode is due to a reaction of the reactive gas with the surface of the sputtered target and its conversion to a compound (Musil, Baroch, Vlcek, Nam, & Han, 2005). Reactive sputtering can occur in three different locations within the sputtering chamber: (a) on the substrate, (b) within the plasma or (c) on the metal target, which is highly undesirable. If the reaction between metal ions and reactive gas occurs on the metal target, a thin dielectric layer will form on the metal target; often referred to as target poisoning. With the buildup of an insulating layer on the surface, positive ions accelerated in the plasma collect on the target surface and charge the insulating layer. The voltage buildup is referred to as arcing and can cause serious problems to the target. When arcing occurs, the target material can melt at localized points. This erosion can contaminate the source as well as degrade the target (Grove, 2000). There are two ways to suppress or eliminate arcing: (1) to eliminate un-eroded areas and (2) to remove the accumulated charge from insulated surfaces on the un-eroded areas (Musil et al., 2005). It is the second solution that was utilized in this study. The accumulated charge was removed from the insulated surface by using pulsed dc sputtering.

2.3.3 Pulsed DC sputtering. PDC sputtering can be used to prevent arcing. PDC power interrupts the voltage buildup by applying a short positive pulse to the target (Kelly, Henderson, Arnell, Roche, & Carter, 2000). The power is applied to the target for a time on, the ‘on-time’

during which a negative voltage pulse of a few hundred volts is applied to the target. At the end of an 'on-time', the power is switched to a small positive voltage. Electrons are attracted to the target through this positive pulse and these flux negative particles will partially or fully discharge the insulating layer (Belkind et al., 2005). Fully discharging the insulating layer on the target will result in a pure metal target again. Kelly et al. found that periodic target voltage reversals effectively discharge poisoned regions on the target (Kelly et al., 2000). This finding is important because target poisoning leads to arcing. If the occurrence of poisoning is decreased or diminished, then the occurrence of arc events at the target will also decrease. The decrease in occurrence of arcing will stabilize the deposition process. Using PDC sputtering, high-quality defect-free metal oxide films can be deposited without fear of target poisoning and arcing.

2.4 Nano-Imprint Lithography

Nanoimprint lithography (NIL) is an emerging nano-patterning method, combining nanometer-scale resolution and high throughput. NIL is a top-down method where a pattern with nano- to micrometer scale features can be replicated on another surface, commonly on thermo- or UV- curable polymer film, and the stamp may be reused many times. Thus, the volume manufacturing of nanostructured components become possible using NIL technique. At present, structures with feature sizes down to 5nm have been realized, and the resolution is limited by the ability to manufacture the stamp (Schvartzman & Wind, 2009; Xia et al., 2008). The variations in the imprint techniques based primarily on the type of material used for the replicated template (stamp) and for the imprintable resist material. The review by Costner et al.(2009) of recent advances of lithography techniques highlights three major ones: thermal- also called hot embossing; soft-lithography also referred as "ink" imprinting; and step and flash imprint lithography is a room temperature and low-pressure imprint technique in which the stamp is

transparent for UV-light and the imprint material is a photo-curable. The other review (Balla, Spearing, & Monk, 2008) adds an optical lithography to classifications of imprint techniques and provides some assessment criteria for imprinting process, such as: line width, relief height, initial resist thickness, residual layer thickness, and imprint area and line width tolerances. According to the review, the higher accuracy of alignment and uniformity over the entire wafer is achievable using UV-NIL, while the high aspect ratios of 10:1 with feature widths of below 250 nm have been formed using thermal-NIL, which introduces the capability to imprint a wider variety of devices. Nanoimprint lithography (NIL) is a replication technique which has proven to provide a resolution unmatched by many other techniques, while at the same time offering parallel and fast fabrication of micro- and nanostructures. The resolution achieved so far by NIL is much higher than that used in the industrial fabrication of processors and memory chips with high-end photolithography. Apart from mentioned advantages NIL offers even more possibilities: creating a three-dimensional resist pattern; and patterning of specific functional materials and polymers, without losing their chemical properties. Furthermore this ability can be used to fabricate more complex structures, e.g. by building up devices with imbedded channels (Xia et al., 2008). The advantages of thermal NIL are: the high resolution of the smallest feature sizes; simple mask fabrication; high throughput and low cost of ownership. The sheer financial and physical barriers of other techniques are now so high, that alternatives such as NIL are considered as best way to low down the investments for the manufacturing of next generation of chips with the nano-scale feature sizes (Table 2.1). This means that all technical issues connected with NIL for integration into chip manufacturing bear the task of full compatibility, similar specifications, yield and throughput.

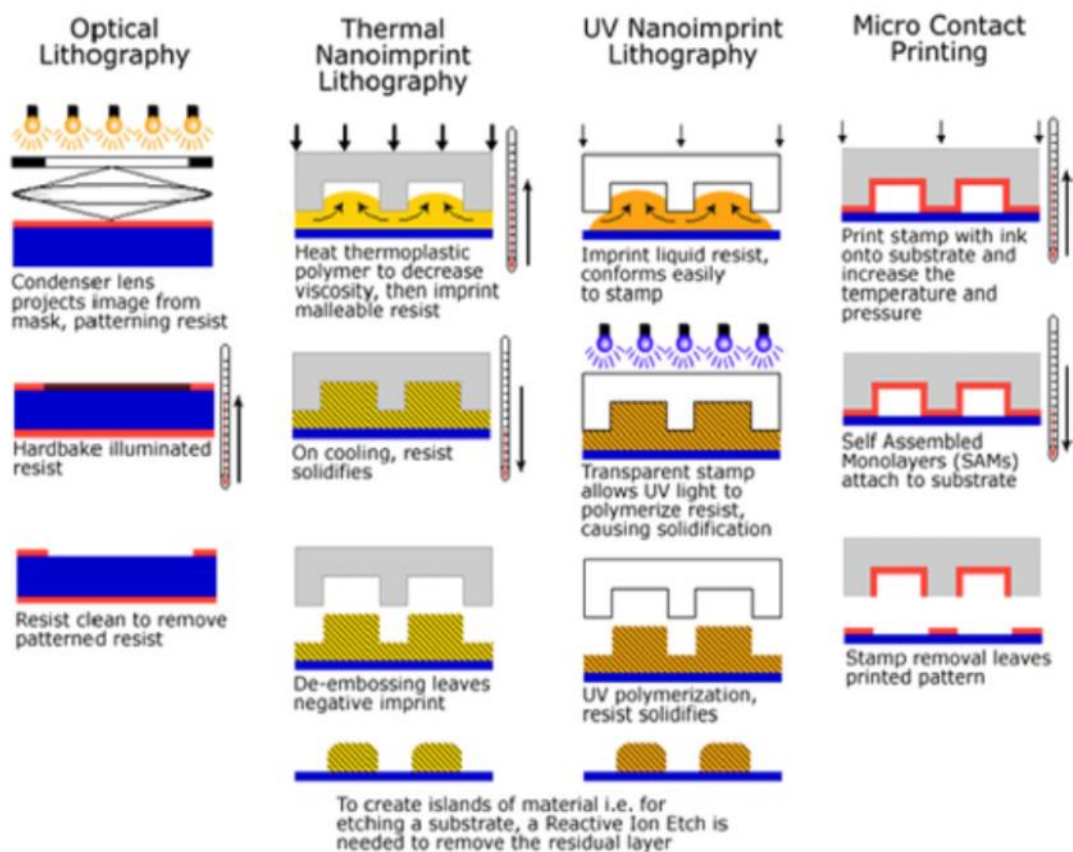


Figure 2.8. Schematics of imprint techniques, adapted from (Balla et al., 2008).

Table 2.1.

Various of lithographic patterning techniques, practical and theoretical resolution limits.

Adapted from (Handbook of Nanotechnology, 2007)

Lithography type	Practical resolution limit	Ultimate resolution limit
UV -contact	2500 nm	125 nm
UV projection	150 nm	50 nm
EUV projection (soft X-rays)	90 nm	30 nm
X-rays / proximity / 1:1 mask (with parallel X-rays)	70 nm	10 nm
Ion beam	30–50 nm	10–20 nm
Electron beam (low-energy beam arrays)	40–50 nm	7–20 nm
Electron beam projection (SCALPEL)	90 nm	35 nm
Imprinting (embossing)	20–40 nm	5–10 nm
Printing (contact)	30–50 nm	10 nm
Scanning probe microscopy methods	15 nm	0.5 nm

2.4.1 Thermal NIL. The thermal NIL has unique advantage of using of thermoplastic polymers those changes between a solid and a highly viscous state is possible within a range of some tens of °C. The typical thermal NIL process includes following steps:

- 1) coating the substrate with the thermoplastic polymer (thermal resist);
- 2) aligning the stamp (commonly made from Si by e-beam lithography) with the coated substrate;
- 3) heating the substrate above the glass transition temperature when a resist material became viscous and applying pressure. The viscous polymer is forced to flow into the cavities of the stamp by the pressure applied on the stamp and substrate. The resist materials can be cured during heating so after certain amount of time they hardened and keep the shape of the stamp;
- 4) cooling down the polymer, while maintaining the pressure;
- 5) the pressure release, and de-molding (stamp retrieving);
- 6) removing the residual layer remaining in the thin areas of the resist for pattern transfer, using an (ideally) anisotropic etching process.

Based on the process description given above, the following parameters are important and should be controlled during process: temperature, pressure and time for imprinting. The typical diagram of imprint process is given in Figure 2.9. It is obvious that process parameters directly depend on what kinds of materials are used for stamp and thermal resist.

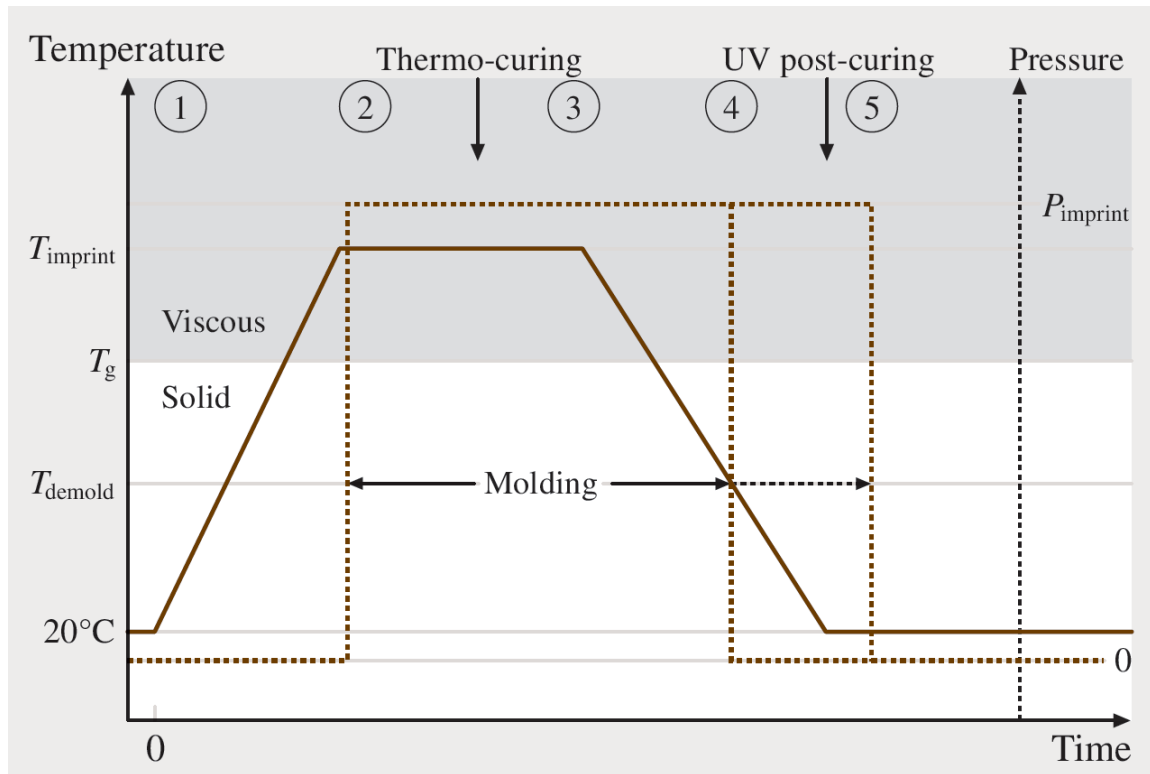


Figure 2.9. Imprint process diagram.

2.4.1.1 Thermal resists materials. Resists used in NIL are polymers defined by their chemical composition and physical properties. The thermoplastic polymers whose mechanical properties can be repeatedly and reversibly changed from a solid into a viscous state by simply varying the temperature are mostly used in NIL process. Therefore it is important to know the properties of polymers such as the temperatures for transitions from liquids over viscoelastic rubbers to solids, and how the mechanical properties such as stiffness, strength, viscoelasticity, toughness, and viscosity changes during NIL process.

A polymer is a large molecule made up of many small, repeated, simple chemical units, joined together by chemical reaction. The typical polymer is a repetitive sequence of particular atomic groups, and can be presented in a form of sequence $(-A-A-A-)$ or $-(A)_N-$. Where A is the basic unit, is also called the monomer unit, and the number of units N in the sequence is

called the degree of polymerization. The molecular weight of a polymer is defined by the weight of a molecule expressed in atomic mass units (amu). For example, a classical resist material, poly-methyl-methacrylate (PMMA) exhibits very good resolution for both electron-beam lithography (EBL) and thermal NIL. A high-molecular-weight PMMA, typically above 500 kg/mol (also 500 k), is normally used for EBL, since the development contrast between exposed and unexposed areas increases with molecular weight (Dobisz, Brandow, Bass, & Mitterender, 2000). A lower molecular weight, of some tens of kg/mol, is patterned in NIL, due to the strong increase in temperature-dependent viscosity with molecular weight (Khoury & Ferry, 1996).

It is important to note that viscoelastic properties of polymers are critical for thermal NIL process. In general, the reduced viscosity of polymers at higher temperatures is a result of the increasing ability of the chains to move freely. The viscoelastic behavior of polymers is described by glass transition temperature (T_g), which is related to the thermal energy required to allow changes in the conformation of the molecules at a microscopic level. The transition is not sharp, meaning it is not thermodynamically well defined. It is therefore different from melting, (T_m), which is an equilibrium transition between crystalline and liquid state. A distinct change from rubbery (above T_g) to glassy (below T_g) behavior is commonly observed in a wide range of polymers over a relatively narrow temperature range. For thin films, however, the T_g can be different from bulk values.

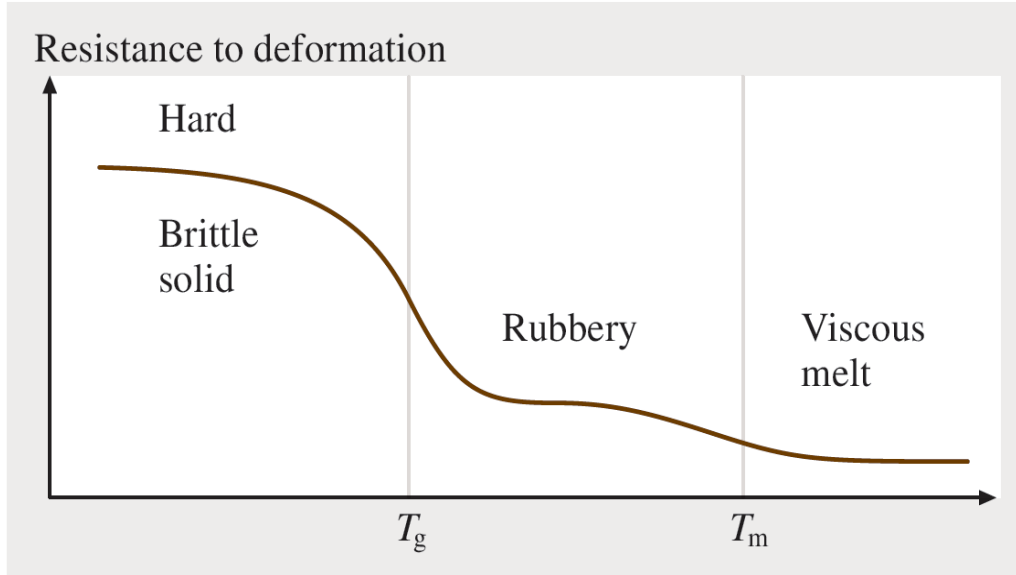


Figure 2.10. Mechanical resistance to deformation as a function of the temperature for an amorphous polymer.

The rheological data of polymers is a crucial issue, especially for thermal NIL, as it allows optimization and control of the imprint process as it discussed in next section. Since the viscosity of thermoplastic polymers are highly depends on temperature, the difference could be 2-3 orders, it is important to know the rheological data of resist for correct estimation of imprint temperature and time. Generally, the temperature behavior of viscosity for amorphous polymers is described by Williams-Landel-Ferry (WLF) equation(Krevelen, 1990):

$$\log a_T = \log \frac{\eta_o(T)}{\eta_o(T_{ref})} = \frac{c_1 (T - T_{ref})}{c_2 - (T - T_{ref})} \quad (2.3)$$

Where a_T called the temperature shift factor and the constants c_1 and c_2 depends on the reference temperature (T_{ref}) chosen.

Scheer et al. (2008) was noticed that even for well-known and well-studied PMMA polymer literature reports a wide range of WLF constants (Figure 2.11). He modeled the viscous behavior of PMMA by imprintability test, using single cavity square stamps 400 nm and 5

micron sizes. The results of his work confirmed that generalized parameters of WLF are precise enough for the stamp features down to 400 nm size.

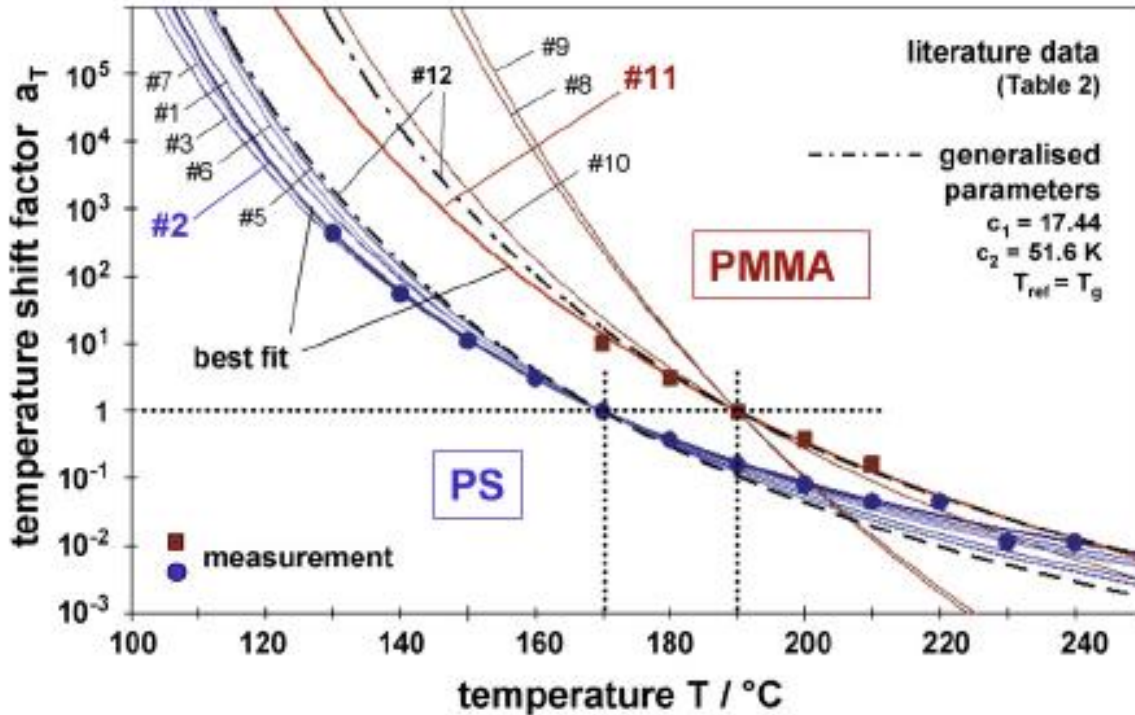


Figure 2.11. Temperature dependent shift factor, compared to literature data (Scheer et al., 2008).

A wide range of polymers with thermoplastic behavior could be used as thermal resists. In addition to thermoplastic behavior they should be easily solvable by safe solvents and at the same time chemically resistant to the etchants of substrate materials; and, preferably, available at low cost. For the last decades, when NIL been developed, a number of resists have been created, improved and studied (Grigorescu & Hagen, 2009; Hwang et al., 2008; Perez Toralla et al., 2009; Simon et al., 2009). A typical NIL resists and their properties are listed in Table 2.2

Table 2.2.

Common resist materials for thermal NIL. Adapted from (Handbook of Nanotechnology, 2007).

Material	Solvent	Tg at Mw	Viscosity at Temperature	Comments
Poly-methyl-metacrylate (PMMA)	anisole, ethylactate	108 °C at 25-950k	10 ⁵ -10 ⁹ Pas at 170 °C	the classic NIL resist
Polystyrene (PS)	toluene	100 °C at 50k		integrated optics
Polycarbonate (PC)	cyclohexanone	145 °C at 34k	2350 MPas	integrated optics, n = 1.6; high etching resistance
Cyclo-olefine copolymer (COC)	toluene	60-180 °C	2600 MPas	highly transparent, chemically resistant, low water absorption.
mr-L 6000	safe solvents	30 °C at 7k		UV curable, low-Tg NIL resist, used for polymer stamps and mix-and-match, multilevel patterning
mr-I 8000	safe solvents	115 °C		high-etch-resistance NIL resist

The mechanical and chemical properties of stamp materials are also important for successful NIL process. The critical mechanical parameters of stamps are: hardness and thermal stability, thermal expansion coefficients, roughness and notch resistance. The performance and life-time of stamp can be significantly improved by applying good anti-sticking coating on stamp surface. Because the molded polymer film is squeezed between the two surfaces of the stamp and substrate, they need to exhibit opposed surface properties. The adhesion at both interfaces must be different to an extent that, while the polymer film adheres perfectly at the substrate surface, the stamp can be separated from the structures without any damage at any location of the stamp. A low-surface-energy release layer on stamp surfaces not only helps to improve imprint qualities, but also significantly increases the stamp lifetime by preventing surface contamination. An anti-adhesive coating has to be chemically inert and hydrophobic, but at the same time allow

a filling of the mold cavities when the polymer is in its viscous state. The most common silicon stamps can be coated with anti-sticking films using silane chemistry (Okada et al., 2009).

Fluorinated trichlorosilanes with different carbon chain lengths are commonly used due to their low surface energy, high surface reactivity, and high resistance against temperature and pressure. They support multiple, long embossing sequences with repeated temperature cycles higher than 200 °C. The silane coating can be performed by immersion in a solution of iso-octane, or by chemical vapor deposition (CVD), either at ambient pressure by heating the silane on a hot plate or by applying a moderate vacuum of a few mbar. The advantage of the vapor deposition method is that it is not affected by the wetting ability of a surface, so that it is suitable for stamps with extremely small nanostructures (Truffier-Boutry et al., 2009).

2.4.1.2 Process parameters of thermal NIL. Most of our considerations here are valid for a range of practical process parameters, as used in current hot embossing processes, where linear behavior can be assumed (Newtonian flow regime). This is in particular the case at molding temperatures well above the T_g (50 °C above T_g). During embossing the linear movement of a stamp is transformed into a complex squeeze flow of viscous material. In the thin polymer films used in NIL, a small vertical displacement of the stamp results in a large lateral flow. The two surfaces of the stamp and the substrate have to come entirely into contact with each other and maintain this contact until the desired residual layer thickness is reached.

In Figure 2.12 the embossing of a stamp with line cavities is schematically shown. Before embossing, the polymer film has an initial thickness h_0 and the depth of the micro-relief is h_r . For a fully inserted stamp, the film thickness under the single stamp protrusions with width s_i is h_f . Applying the continuity equation with the assumption that the polymer melt is incompressible

(conservation of polymer volume), we get a specific residual layer height h_f . This can be directly deduced from the fill factor v , the ratio of the area covered by cavities to the total stamp area.

$$h_f = h_0 - v h_r \quad (2.4)$$

Where $v = \frac{\sum_i w_i}{\sum_i (s_i + w_i)}$

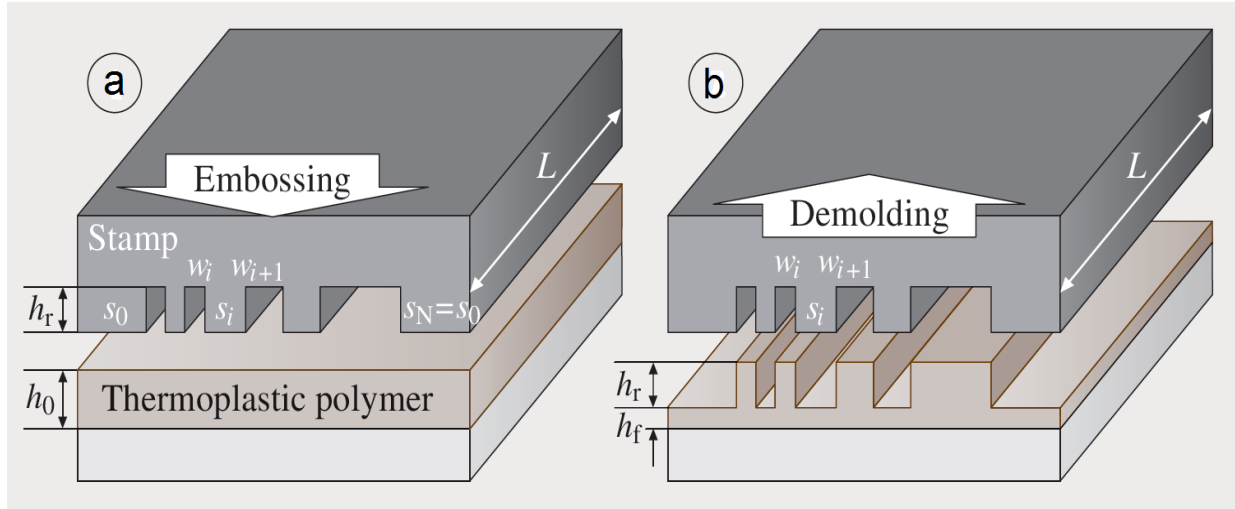


Figure 2.12. Geometrical definitions used for the description of the flow process for a stamp with line cavities and protrusions. (a) before molding, (b) after de-molding.

The formula (2.4) applies for rigid stamps with a constant fill factor. A simple model for the squeezed polymer flow underneath the stamp protrusion is obtained by treating the polymer as an incompressible liquid of constant viscosity, and solving the Navier–Stokes equation with nonslip boundary conditions at the stamp and substrate surfaces. According to this model, given for line-shaped stamp protrusions and cavities in, we find the following expression, known as the Stefan equation (*Handbook of Nanotechnology*, 2007), for the film thickness $h(t)$ underneath the stamp protrusion when a constant imprint force F is applied to the stamp protrusion:

$$\frac{1}{h^2(t)} = \frac{1}{h_0^2} + \frac{2F}{\eta_0 L s^3} t \quad (2.5)$$

Inserting the final thickness $h_f = h(t)$ and applying a constant pressure during molding $P = F/(sL)$ someone can estimate the embossing time as:

$$t = \frac{\eta_0 s^2}{2P} \left(\frac{1}{h_f^2} - \frac{1}{h_0^2} \right) \quad (2.6)$$

As a direct consequence of the Stefan equation it can be seen that, for the same pressure, small (narrow) stamp protrusions will sink faster than large (wide) ones. Therefore the stamp geometry can be chosen with the reduced size of the protrusions. The strong dependence of the embossing time on the pressing area has the consequence that, for a fully inserted stamp relief (full contact over the total stamp area), the flow practically stops. For this case, s becomes large and the flow continues only towards the stamp borders. It is also evident that the embossing force has only a weak influence ($t \approx 1/F$). At first sight there is a similar weak influence for η_0 . However, the viscosity can be changed significantly by varying the temperature (section 2.4.1.1). Thus the simplified formula can be used for the estimation of the embossing times.

According to formulas (2.3 – 2.6), there are different areas for optimization of imprint process: initial resist film thickness; temperature regime; stamp geometry and conditions; cooling regime.

The final step of imprint process is de-molding (stamp and substrate separation). It is normally performed after cooling-down, when thermal resist material is considered solid. For thermoplastic materials this happens at a temperature well below T_g . A successful de-molding process relies on a controlled balance of forces at the interfaces between stamp, substrate and molded polymer film. Therefore mechanical, physical and chemical mechanisms responsible for adhesion have to be overcome. This effect can only be solved by coating the stamp surface with sufficient anti-adhesive coating. The thermal expansion coefficient of the substrate and of the stamp should be similar; to avoid a distortion due to mechanical stress induced by the cooling. In

the case of very thin polymer layers, the lateral thermal expansion of the resist is determined by the substrate. For structures with a higher aspect ratio the de-molding temperature should be well below T_g , to enable the de-molding of a hardened resist without distortion. Consequently, the size, shape, and placement of the replicated features may be affected. If a solid curable resist exhibits thermoplastic behavior, it can be molded at an elevated temperature and then cross-linked, either before or after de-molding. Thermoset resists can be cross-linked by heat. Here it is advantageous that the temperature for molding is lower than the curing temperature. Then the structure is first molded and then heated to its cross-linking temperature to induce crosslinking, before the hardened stamp is de-molded.

2.5 Reactive Ion Etching

Mechanism of plasma etching process somewhat similar to the sputtering process from target (ejection of material from surface by ionized plasma), but it also includes the chemical reaction between reactive gas (commonly oxygen for polymers and CHCl_3 for metals). The process can be summarized as follows: dissociated oxygen atoms initiate etching by extracting hydrogen atoms from a polymer chain leaving a radical species on the surface. These radicals react with oxygen molecules from the plasma to form carbonyl and alcohol groups. The resulting volatile products are provided sufficient energy either by ion bombardment or sample heating for desorption and eventual pump-away from the chamber (Hartney et al., 1988).

2.6 Chemical Vapor Deposition

The synthesis of carbon nanotubes (either single- or multi-walled) by CVD methods involves the catalytic decomposition of a carbon-containing precursor on small metallic particles or clusters. This technique involves either a heterogeneous process if a solid substrate is involved or a homogeneous process if everything takes place in the gas phase. The metals generally used

for these reactions are transition metals, such as Fe, Co and Ni (Deck & Vecchio, 2006). It is a rather low-temperature process compared to arc discharge and laser ablation methods, with the formation of carbon nanotubes typically occurring between 600 °C and 1000 °C. Because of the low temperature, the selectivity of the CCVD method is generally better for the production of MWNTs with respect to graphitic particles and amorphous-like carbon, which remain an important part of the raw arc discharge SWNT samples. Both homogeneous and heterogeneous processes appear very sensitive to the nature and the structure of the catalyst used, as well as to the operating conditions (Liu et al., 2007; Zarabadi-Poor et al., 2010). Carbon nanotubes prepared by CVD methods are generally much longer, up to a centimeter (Di et al., 2011; Liu et al., 2007), than those obtained by arc discharge, a few micrometers (Yao et al., 2005).

Depending on the experimental conditions, it is possible to grow dense arrays of nanotubes. It is a general statement that MWNTs from CVD contain more structural defects than MWNTs from arc discharge, due to the lower temperature of the reaction, which does not allow any structural rearrangements (Lamouroux et al., 2007). These defects can be removed by subsequently applying heat treatments in vacuum or inert atmosphere to the products. CVD provides reasonably good perspectives on large-scale and low-cost processes for the mass production of carbon nanotubes, a key point for their application at the industrial scale.

CHAPTER 3

Materials, Manufacturing and Characterisation Techniques

Chapter 2 provided us with the recent advances in technologies chosen to create our nano-devices; this chapter gives the detailed description of technology used and equipment available at NC A&T State University and its limitations that need to be overcome to achieve a final goal of this research. The Magnetron Sputtering, Nano-Imprint and Plasma Etching systems used for the experiments are described and parameters optimizations for each system are discussed. Sample preparation and characterization techniques are also explained.

3.1 Magnetron Sputtering Deposition System

Throughout the study, the AJA International, Inc. ATC 1800 F magnetron sputtering system was used to deposit the catalytic films and can be seen in Figure 3.1.

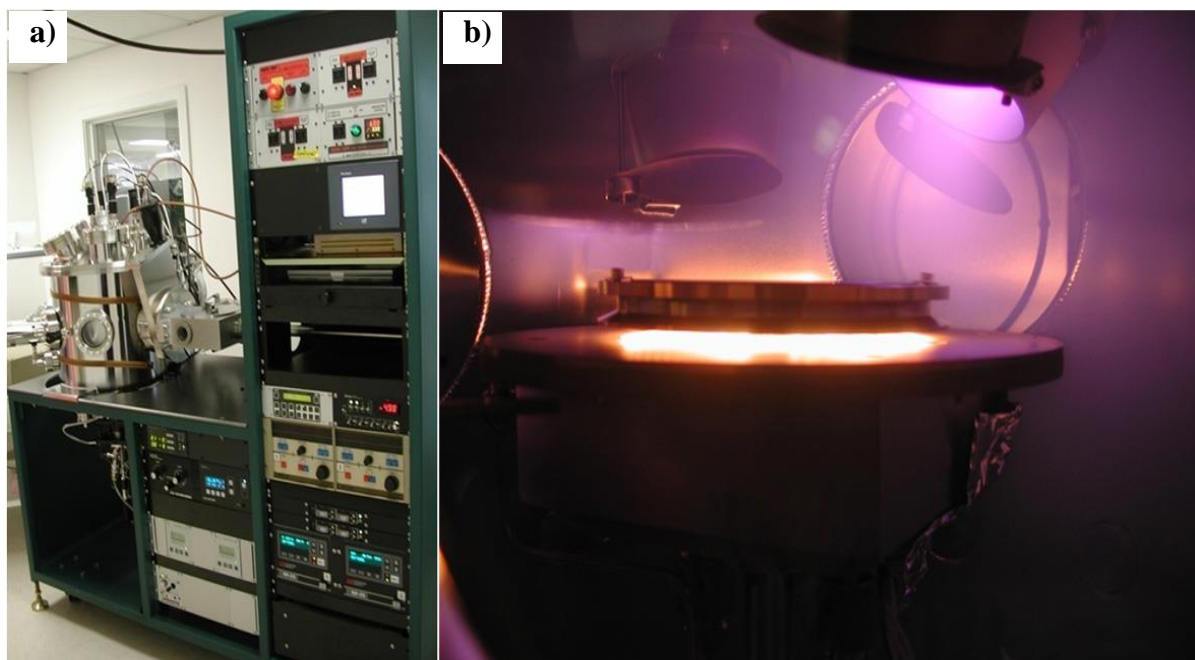


Figure 3.1. AJA International ATC 1800F Magnetron Sputtering system at NCAT (a), and internal view of plasma, guns and heated substrate (b).

The AJA International magnetron sputtering system is composed of three targets and can be used to perform radio frequency (RF) sputtering, direct current (DC) sputtering or pulsed-direct current (PDC) sputtering. RF sputtering can be utilized at a maximum power level of 500 W while the DC sputtering power level is much higher at 1000 W; still higher is the maximum power level of PDC sputtering which is 5000 W. However, it is not recommended to use power more than 50% of maximum level in order to prevent high-voltage breakthrough and target overheating. Although RF sputtering is known to produce high quality thin film coatings that are good for insulating materials, it is a slow process with a very low deposition rates. DC reactive sputtering has relatively low deposition rates and is known for being problematic when depositing oxides by reactive sputtering. Also, when using DC reactive sputtering, arcing can occur at the target, poisoning the target. To avoid low deposition rates and possible arcing, PDC reactive sputtering was used to produce high quality films with high deposition rates.

The substrates were loaded into the AJA International magnetron sputtering system via the loading dock. Once placed into the loading dock, the substrates were loaded into the main chamber. The magnetron sputtering system is operated under a high vacuum, which is maintained by a turbo molecular pump. The base pressure in a deposition chamber maintained at 10^{-7} mTorr, and the gage system allows controlling the working pressure during deposition process at the range 0.5 to 40 mTorr. Located in the main deposition chamber, a stand for the substrate holder has a heater up to the 800 °C and can rotate at a constant speed to ensure a uniform film deposition. Along with substrate rotation and heating, the system has a residual gas analyzer (RGA). The RGA monitors the distribution of the gases within the chamber and it is this constant monitoring that allows for deposition parameters to be precisely copied at a later time resulting in the development of reproducible coatings.

3.2 Nano-Imprint Lithography

The Nanonex 2000 is a single-sample nano-imprint lithographer, equipped with the Xe lamp for expose of UV-curable resists and high temperature (up to 300 °C) and pressure (250 psi) embossing system. Pattern replication is performed by mechanically deforming resist material using stamps with the micro- or nano-scale protrusions. The system is designed to provide consistent and uniform pressure across the surface of a sample. The sample holder designed to hold one 4" wafer. Common resist polymers include PMMA and PDMS, pattern can be transferred on Si, glass or Pyrex wafers.

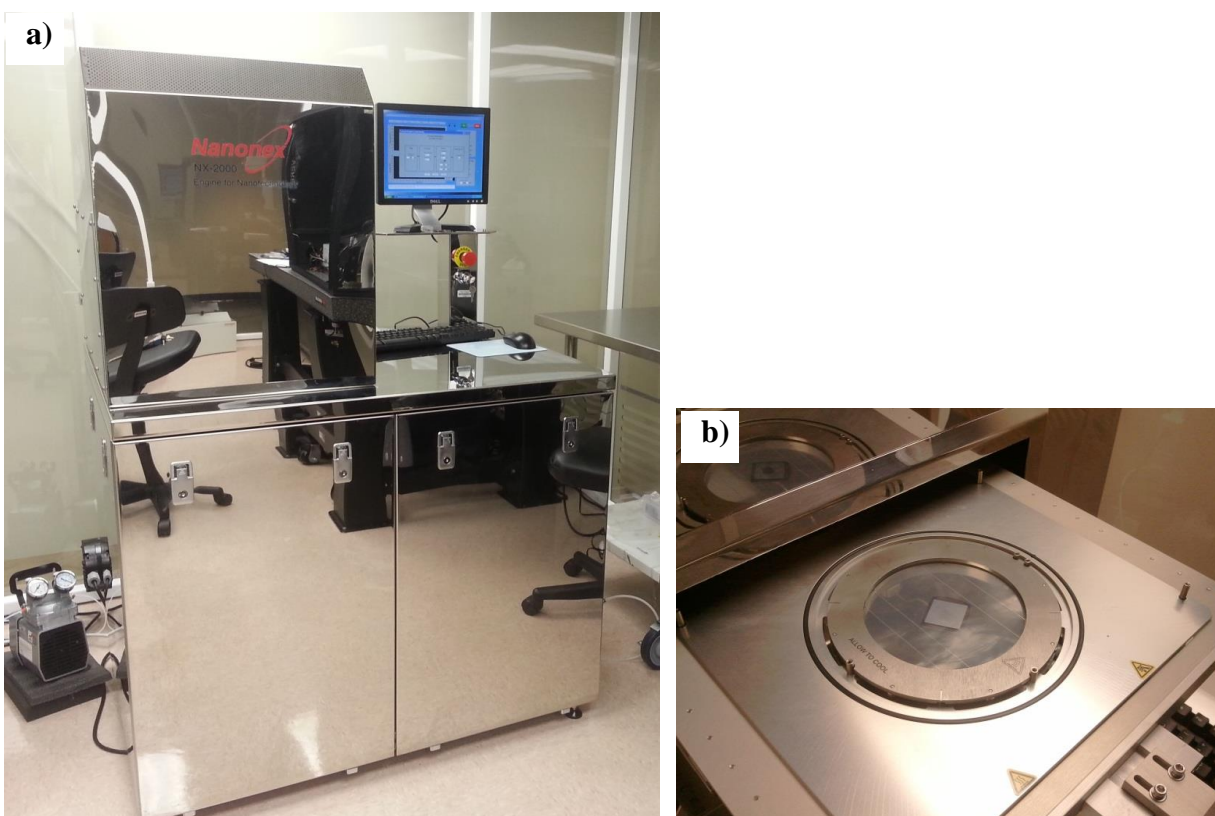


Figure 3.2. Nanonex 2000 imprint system at NCAT (a), and sample holder (b).

3.3 Chemical Vapor Deposition

The EasyTube™ 3000EXT system consists of a furnace rolling around 48 inch long and 6 inch diameter quartz process tube and cooling fan, which allows reducing the synthesis time by

at least 2 hour for each run/experiment. The furnace could be pre-heated up to the process temperature then the furnace moves towards the process zone. This will reduce by 1 hour the temperature ramp-up time. After CNT deposition, the furnace, which maintains the process temperature, will move back to the outlet zone and the cooling fan would drop the substrate temperature as fast as possible. This configuration will let the process zone cool down to room temperature within 10 minutes and save about 1~2 hours' time compared to conventional methods. Then, we can load a new batch of wafers for CNT synthesis and move the furnace towards the process zone, and then start a new circle of experiments.

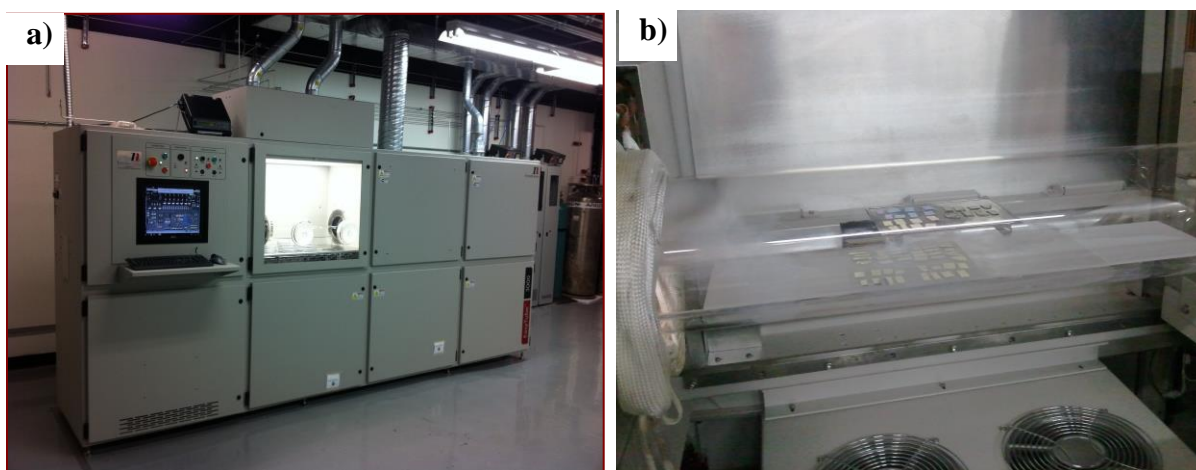


Figure 3.3. The EasyTube™ 3000EXT system Sputtering system at General Nano LLC: (a) – overall view and (b) – inside quartz reactor.

The substrates were set in a tubular CVD reactor (EasyTube™ Nanofurnace system) for growth of vertically aligned Carbon Nanotubes. The CVD reactor was heated up to 700°C in under flow of Argon which created an inert environment. After reaching 700°C, 200scm of hydrogen was introduced for 10min in order to bring the catalyst back in reduced state which is the active state. Then CVD was carried out by introducing the following gas mixture into the reactor: ethylene (acetylene), hydrogen, argon through water bubbler (water vapor) and argon as

carrier for deposition. After that, the reactor was purged with Ar during the final cooling step.

The optimized synthesis parameters were:

- ✓ Gases flow: H₂ 300 sccm; Ar+H₂O 380 sccm; C₂H₂ 85 sccm; Ar 3500 sccm.
- ✓ Temperature: 780 °C.

3.4 Structural Characterization Techniques

Several structural characterization techniques were used during this research. The following sections have been dedicated to discussing the experimental techniques that have been used to structurally characterize the fabricated samples.

3.4.1 Film thickness measurement. The XRR of the fabricated films were observed to verify the film thickness. The observed micrographs are shown in It must be noted that, depending on the spatial distribution of the film on the substrate, insignificant differences were observed compared to the profilometer data. A low-angle X-ray reflectometry (XRR) is a great non-destructive technique for the study of thicknesses, density and smoothness of thin film structures with thicknesses from 2 to 50 nm.

LEPTOS is a software package designed to display, analyze and fit the data from High-Resolution X-Ray Diffraction (HRXRD), specular X-Ray Reflectivity (XRR), off-specular X-Ray Diffuse Scattering (XRDS), Grazing-Incidence Diffraction (GID), Grazing-Incidence Small-Angle Scattering (GISAXS) and Stress measurements as well as Wafer Area Mapping using all the above-mentioned techniques. LEPTOS uses the dynamical theory to simulate X-ray diffraction in various geometries and glancing-incidence X-ray specular reflectivity, calculates coplanar X-ray diffuse scattering and non-coplanar grazing-incidence small-angle scattering on the basis of the distorted-wave Born approximation. Real experiment conditions may be taken into account, including instrumental and resolution effects, background noise, and so on. The

software also integrates a sophisticated fit module for fully automated data fitting and extended capabilities for interpretation of wafer area mapping measurements. All the data interpretation procedures can be processed by LEPTOS in a fully automated script mode, both in foreground and background regimes.

LEPTOS operates with the objects, which are designed to imitate the real objects used in X-ray analysis, like samples, X-rays, diffractometer, etc. This concept helps to build a convenient and logical interface for data interpretation. An example of the use of LEPTOS for NRX1025 film thickness evaluation is presented in Figure 3.4.

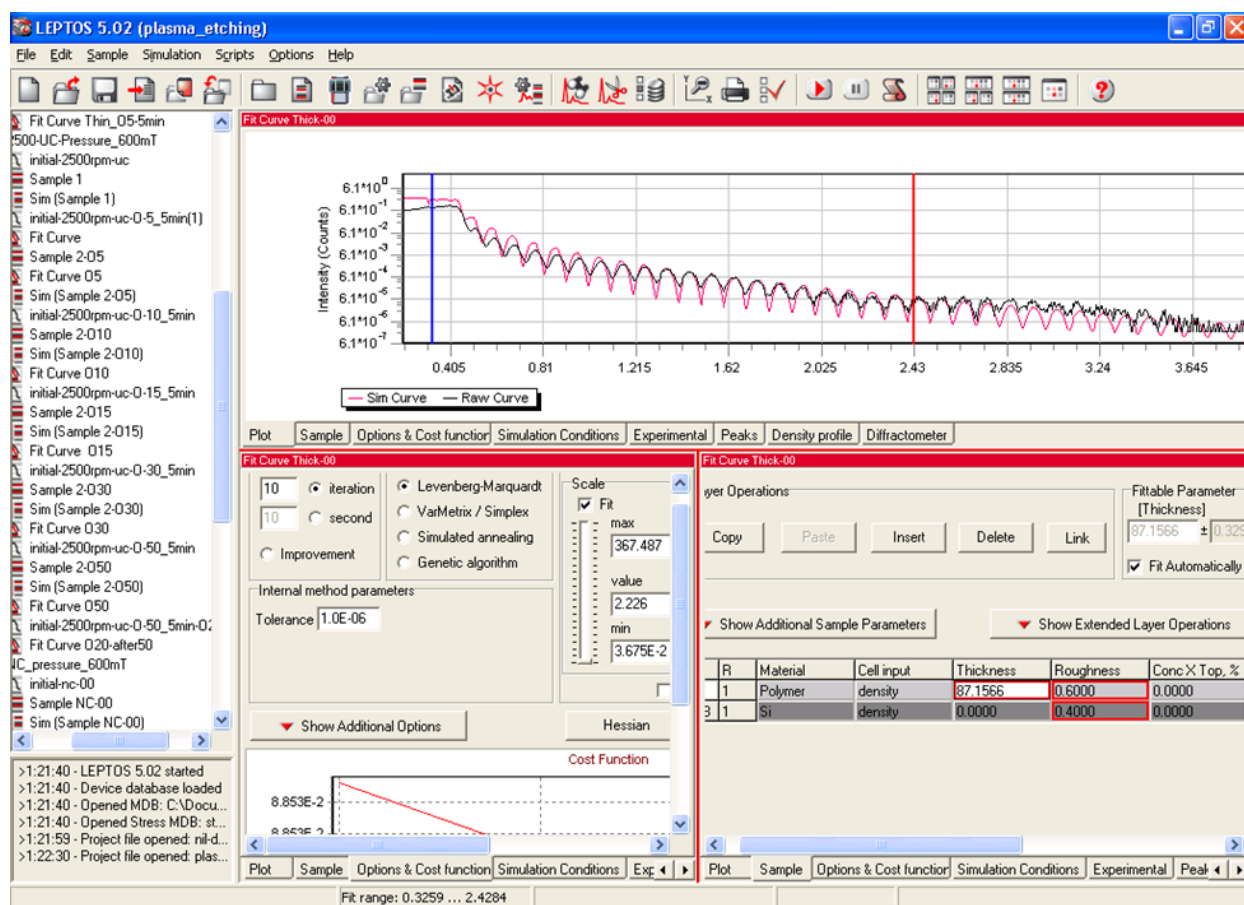


Figure 3.4. XRR data fitting with the LEPTOS software.

3.4.2 Crystal structure characterization. X-ray diffraction was performed throughout the duration of this study using the Bruker AXS D8 Discover, which can be seen in Figure 3.5.

XRD is a high-tech, non-destructive technique for analyzing a wide range of materials with thin-films being just one example (Bruker, 2012). The diffractometer operates on a 40 kV and 40 mA CuK_α radiative source with a wavelength of 1.54 \AA . It is equipped with a couple of exchangeable slits (0.1; 0.2 and 0.5 mm) on both the source and detector.

X-ray diffraction is the best tool to investigate the composition, structure and stresses in materials. Nowadays using them we are able to analyze the structure and composition of thin films (down to 20 nm thickness) and determine the thicknesses of multilayered films with the precision of 1nm and stresses inside thin film structure.



Figure 3.5. Bruker AXS D8 Discover XRD machine at NCAT.

3.4.3 Scanning electron microscopy and energy dispersive X-ray. Scanning electron microscope (SEM) is the most widely employed thin film and coating characterization instrument (Ohring, 2002). Hitachi® SEM SU8000 was used to visualize the fabricated patterns and CNT arrays. Depending on the particular sample, appropriate voltage and current were

selected to capture high quality images. Elemental compositions of the alumina films produced by reactive sputtering were also evaluated using the attached energy dispersive X-ray analyzer.

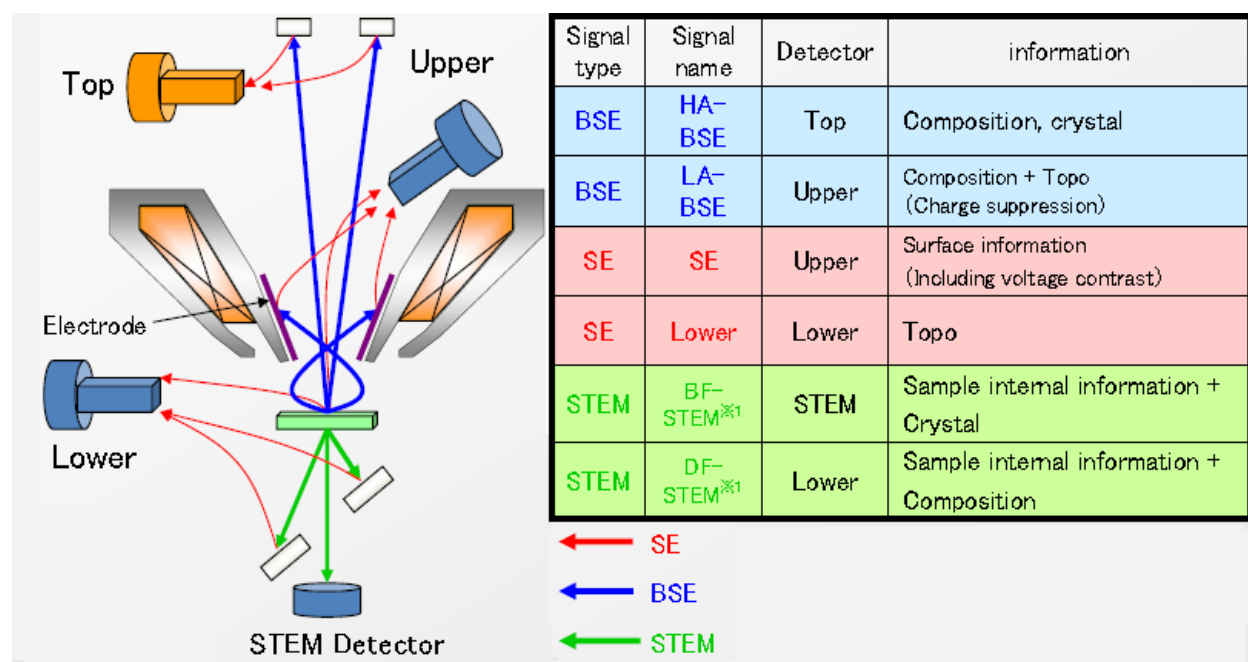


Figure 3.6. Diagram of detectors used in Hitachi SU8000 FE-SEM (Hitachi, 2012).

In a conventional SEM, electrons are thermionically emitted from a cathode filament; they are drawn towards an anode and focused by two successive condenser lenses. The beam is deflected by a pair of scanning coils embedded in the objective lens, which causes the beam to either raster or move linearly over a rectangular area of the sample surface. The electron beam typically has an energy ranging from 0.2 keV to 40 keV, and the beam spot size is typically 10 Å in diameter. Primary electrons from the landing beam decelerate and lose energy; the lost energy is transferred inelastically to other atomic electrons and the lattice. When the primary electron beam interacts with the sample, the lost energy due to repeated random scattering and absorption effectively spreads and fill a teardrop-shaped interaction volume within the sample. The size of the interaction volume depends on the electron's landing energy, the atomic number of the specimen and the specimen's density (Goldstein, 2003).

Typical signals produced by SEM during scanning include secondary electrons (SE), back-scattered electrons (BSE), characteristic X-rays, light, heat and specimen current (Reimer, 1998). Backscattered electrons consist of high-energy electrons which are elastically scattered and essentially possess the same energy as the incident electron beam. These are reflected or back-scattered out of the specimen interaction volume. The production of backscattered electrons varies directly with the specimen's atomic number. This variation rates causes higher atomic number elements to appear brighter than lower atomic number elements. This interaction is utilized to differentiate parts of the specimen that have different average atomic number (Krinsley et al., 2005). Another advantage of using backscattered/deceleration mode is ability to observe the non-conductive samples without gold coating and charging effect.

When the sample is bombarded by the electron beam, electrons are ejected from the atoms on the specimens' surface. A resulting electron vacancy is filled by an electron from a higher shell, and an X-ray is emitted to balance the energy difference between the two electrons. The X-ray detector measures the number of emitted X-rays versus their energy. Instrumentation for X-ray spectroscopy technique, known as X-ray dispersive spectroscopy (EDS or EDX), is practically always attached to the SEM column. The energy of the X-ray is a characteristic of the element from which the X-ray was emitted (Goldstein, 2003).

3.4.4 Surface morphology characterization. Surface roughness was measured using a NT-MDT NTEGRA platform atomic force microscope, shown in Figure 3.7. Images were taken using semi-contact mode using a super sharp tip with a curvature radius of 3-6 nm. Semi-contact mode is a mode in which the cantilever tip only makes contact with the sample surface occasionally. Semi-contact mode is often the preferred method of contact when completing surface roughness measurements because the force of pressure of the cantilever on the sample

surface is low. The lower contact pressure allows measurements to be completed on softer and easy-to-damage materials such as polymers as well as reduces the risk of the cantilever tip breaking. Along with measuring surface roughness, semi-contact mode is used to determine other surface characteristics, such as elasticity and viscosity of the surface (NT-MDT, 2012). Images were processed using Nova software supplied by NT-MDT.

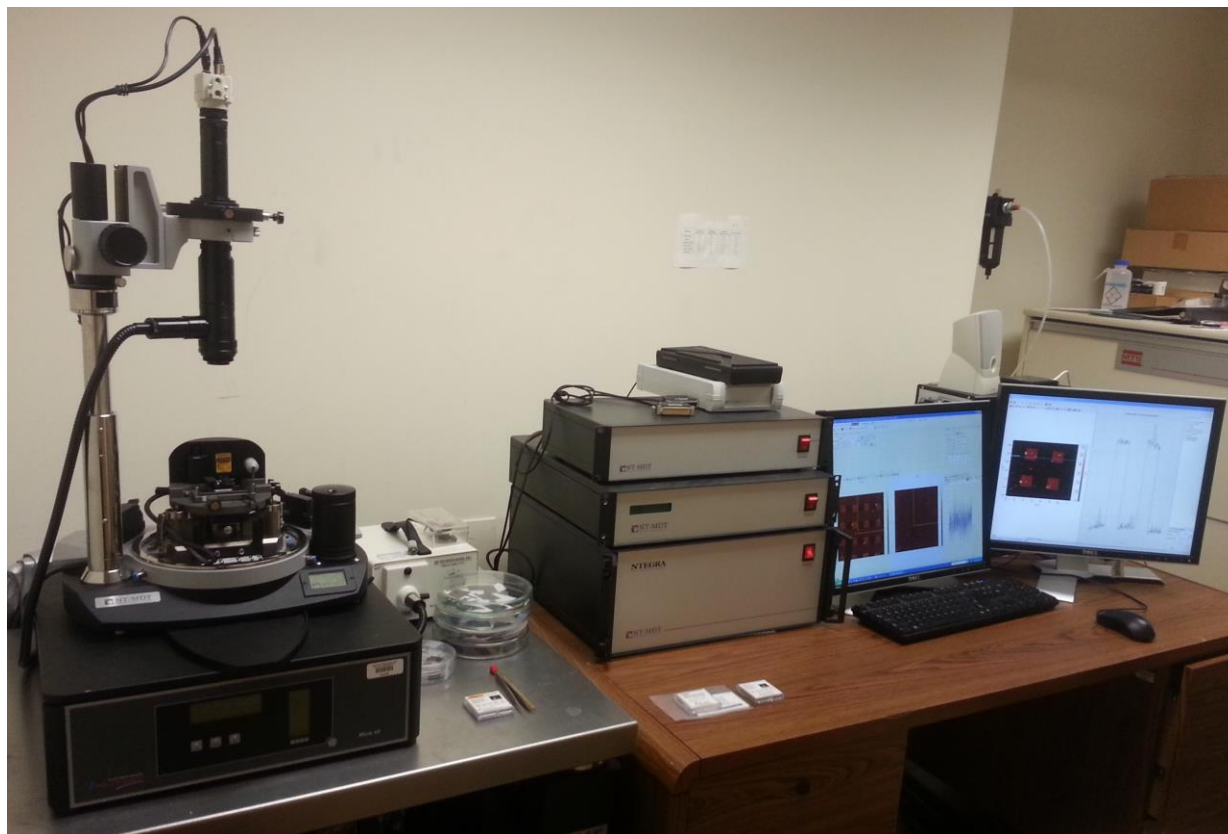


Figure 3.7. NT-MDT NTEGRA platform atomic force microscope at NCAT.

3.5 Carbon Nanotubes characterisation

3.5.1 Raman Spectroscopy. Raman spectroscopy is used in qualitative and quantitative analysis of carbon nanotubes. SWCNTs have offered a unique system for the study of Raman spectra in one-dimensional systems, and at the same time Raman spectroscopy has provided a widely used and powerful tool for the characterization of SWCNTs. The Raman spectra of CNTs, particularly at the single-nanotube level, have been especially rich (M. S. Dresselhaus et

al., 2007). Detailed information about Raman spectroscopy of SWCNTs can be found in the fundamental works of Dresselhaus (M. S. Dresselhaus et al., 2004; M. S. Dresselhaus et al., 2006; M. S. Dresselhaus et al., 2007). The Raman spectroscopy of SWCNTs are referred in, Figure 3.8 which demonstrate the capability of Raman spectroscopy to resolve critical questions regarding SWCNT structure – their chirality indices m and n and their diameter as described in Chapter 2.

Analysis of radial breathing modes (RBM) frequencies allow the determination of the diameter of SWCNTs (M. S. Dresselhaus et al., 2007). For larger diameter tubes (above 3 nm), the RBM feature becomes too broad and cannot be observed. This characteristic thus limits the use of the RBM feature to study large diameter multiwall carbon nanotubes. The RBM from MWNTs is only observed when they have very small diameter inner tubes (below 3 nm).

The Raman spectroscopy of MWCNTs is much more complicated. Several publications specifically are devoted to Raman spectroscopy of MWCNTs (Rao et al., 2000; Sato et al., 2006; Wang et al., 2009). In most of the cases, the Raman spectroscopy of MWCNTs is used to estimate “quality” of nanotubes by separating G and D bands, which are associated with ordered graphitic and disordered graphitic and amorphous components. The ratio I_D/I_G is widely used for this purpose.

The Raman spectra of MWCNTs can be analyzed using model described by Dresselhaus (M. S. Dresselhaus et al., 2002; M. S. Dresselhaus et al., 2005) and Sadezky (Sadezky et al., 2005). The model of spectra fitting and the correspondence of Raman bands are introduced in Figure 3.9 and Table 3.1.

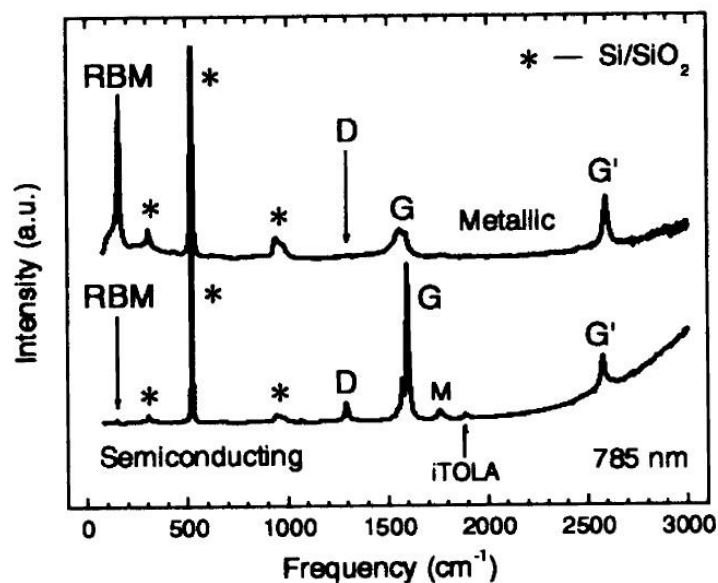


Figure 3.8. Raman spectra from a metallic (top) and a semiconducting (bottom) SWNT at the single nanotube level (M. S. Dresselhaus et al., 2007).

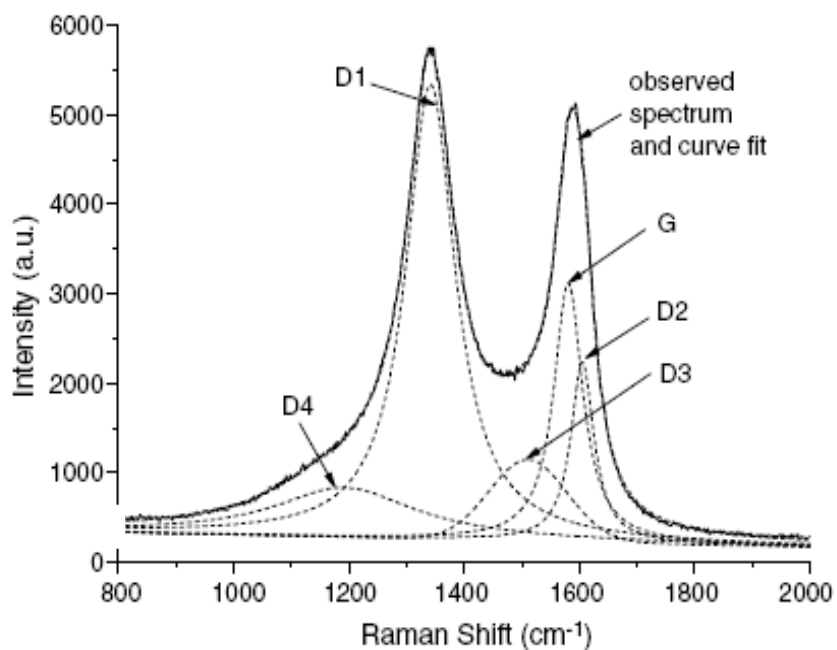


Figure 3.9. Curve fit with band combination for the first-order Raman spectra ($\lambda_0 =$ at 514 nm) from (Sadezky et al., 2005).

Table 3.1.

First-order Raman bands and vibrational modes. Adapted from (Sadezky et al., 2005)

Band	Raman shift (cm ⁻¹)		Vibration mode
	Disordered graphite	Highly ordered graphite	
G	~1580	~1580	Ideal graphitic lattice (E _{2g} -symmetry)
D1 (D)	~1350	-	Disordered graphitic lattice (graphene layer edges, A _{1g} symmetry)
D2 (D')	~1620	-	Disordered graphitic lattice (surface graphene layers, E _{2g} -symmetry)
D3 (D'', A)	~1500	-	Amorphous carbon (Gaussian or Lorentzian line shape)
D4 (I)	~1200	-	Disordered graphitic lattice (A _{1g} symmetry) , polyenes, ionic impurities

CHAPTER 4

Results and Discussion

This chapter is dedicated to the collection of data and their interpretation during this research. All the experimental techniques used to collect data throughout this research work are explained, along with schematic models to elucidate the method. The main characterization techniques used include profilometry, X-ray diffractometry, scanning electron microscopy, atomic force microscopy and micro-Raman spectroscopy.

4.1 Optimization of Magnetron Sputtering Deposition Parameters

4.1.1 Deposition rates. The alumina and metal layers were deposited using all three available power sources. The deposition rates were calculated by formula (4.1). The film thickness was measured by XRR methods (section 3.4.1).

$$\text{Deposition rate} = \frac{\text{Average film thickness}}{\text{Deposition time}} \quad (4.1)$$

Iron and cobalt were deposited by DC sputtering. Alumina was deposited by two sputtering techniques: RF sputtering from alumina target and pulsed DC reactive sputtering from aluminum target with presence of oxygen as a reactive gas. The following deposition parameters were varied in order to find the deposition rates: working pressure, applied power and substrate biasing. For reactive sputtering the oxygen content in reactive gas mixture was maintained at 10% which is the optimum to form clear alumina film without incorporation of aluminum and prevent the poisoning effect on target (Cremer et al., 1999); (Zywitzki & Hoetzsch, 1997). The composition of deposited alumina was confirmed by EDX analysis see Figure 4.1.

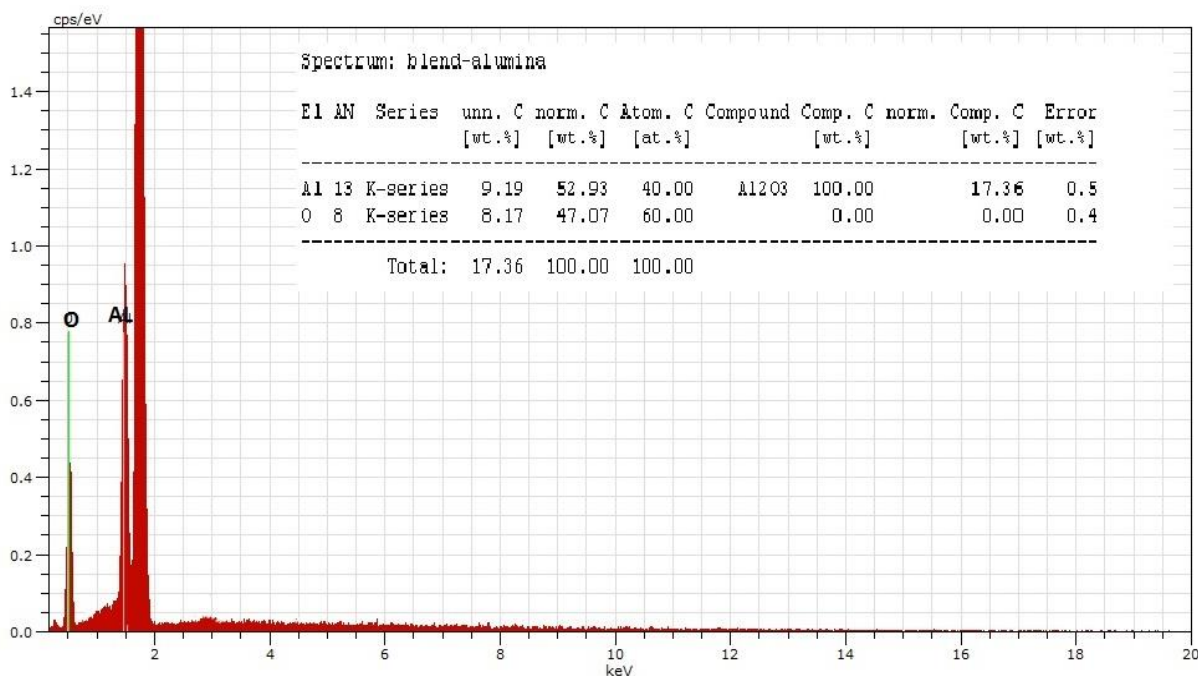


Figure 4.1. Energy dispersion X-ray spectroscopy for Al₂O₃ deposited from Al target by reactive PDC deposition at 100Watts, 2mTorr with O₂ content 10%.

The Table 4.1 presents the deposition parameters, measured thickness of deposited films and estimated deposition rates of alumina, iron and cobalt. As can be seen, increasing the working pressure negatively effecting on deposition rates, since increasing pressure in system cause more collisions of particles on their way to substrate or, in other words, shorten the mean free path of depositing particles. As can be seen from Table 4.1, the increasing the working pressure from 1 to 6 mTorr decreases deposition rate of alumina by approximately 20% from 6 to 4.6 nm per minute. The same tendency was observed for the metals – raising pressure from 1 to 4 mTorr decreases deposition rate by approximately 6%. The deposition rate of material significantly depends on type of source and applied target power. The deposition rate of reactive sputtering is three times higher than alumina deposited from alumina target by RF sputtering.

Thus, the reactive sputtering gives a benefit of faster and cheaper (considering the cost of ceramics over metal targets) manufacturing of alumina coatings.

Table 4.1.

Deposition rates measured by XRR technique.

Target	Power source	Power (W)	Working pressure (mTorr)	Deposition Time (minutes)	Average film thickness (nm)	Deposition rate (nm/min)
Al ₂ O ₃	RF	100	1	20	39.6	2.0
Al ₂ O ₃	RF	100	4	20	35.8	1.8
Al ₂ O ₃	RF	250	1	10	61.2	6.1
Al ₂ O ₃	RF	250	2	10	54.6	5.5
Al ₂ O ₃	RF	250	4	10	49.8	5.0
Al ₂ O ₃	RF	250	6	10	46.2	4.6
Al	PDC	100	2	10	64.8	6.5
Al	PDC	100	4	10	38.4	3.8
Al	PDC	200	2	5	75.9	15.2
Al	PDC	200	4	5	55.2	11.0
Fe	DC	100	1	10	49.3	4.8
Fe	DC	100	4	10	45.1	4.5
Co	DC	100	1	10	52.2	5.2
Co	DC	100	4	10	48.6	4.9

4.1.2 Structural characterization of deposited films. The topology of alumina layer is very important (plays significant role) for catalyst system performance in further chemical reaction of carbon cracking in CVD chamber. So it is important to control the thickness, roughness and phase composition of alumina layer. The best results so far were achieved with the catalyst (Fe or Fe/Co combinations) deposited over smooth, amorphous alumina layer with the thickness of 5-10nm. The smooth film is also benefits during spin-coating process of thermal resist for future NIL patterning; allow spinning the thin and uniform resist layer (section 4.2.1).

4.1.2.1 Phase composition of alumina films. The XRD analysis of alumina films deposited at room temperature, 200, 400, and 600C shows that the phase composition of alumina changes as the temperature rises (Figure 4.2). The obtained x-Ray patterns correspond to the data from Joint Committee on Powder Diffraction Standards (JCPDS): 00-050-0741. It should be noted that amorphous alumina cannot be detected by XRD method. The formation of crystalline γ -alumina started at substrate heated more than 300C for RF deposition. It was also noted that for reactive PDC sputtering the deposition/working pressure also plays a significant role – the γ -alumina appears at 400C when the pressure in deposition chamber maintained at 2mTorr and at 600C with the pressure of 4mTorr.

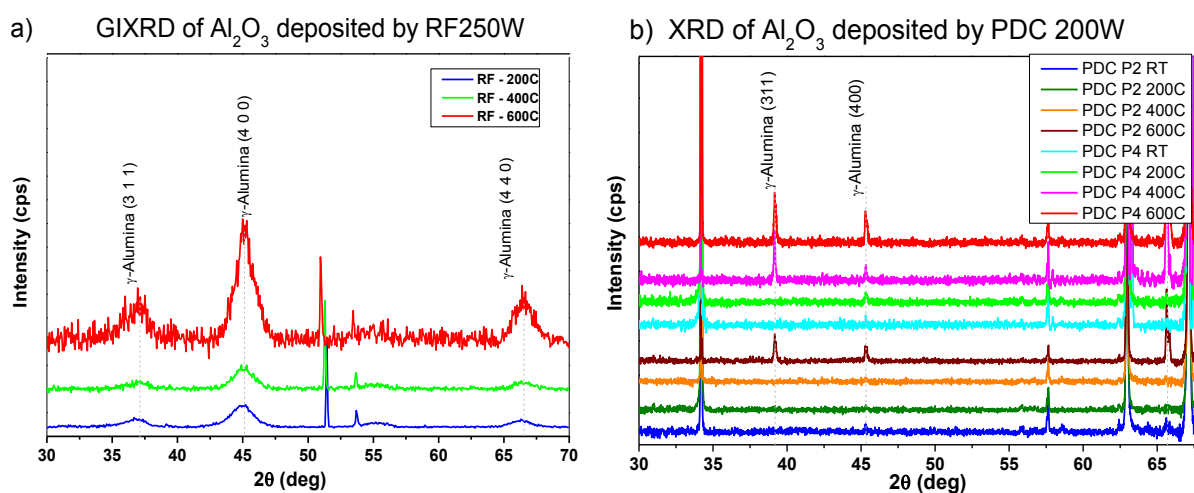


Figure 4.2. XRD diffraction patterns of alumina deposited by: (a) RF sputtering and (b) Pulsed DC sputtering.

4.1.2.2 Surface topology of alumina films. The SEM analysis conducted on alumina films deposited by pulsed DS sputtering shows that increasing the substrate temperature during deposition increases the porosity and roughness of the films (Figure 4.3) it was also confirmed by AFM analysis (Figures 4.4 and 4.5).

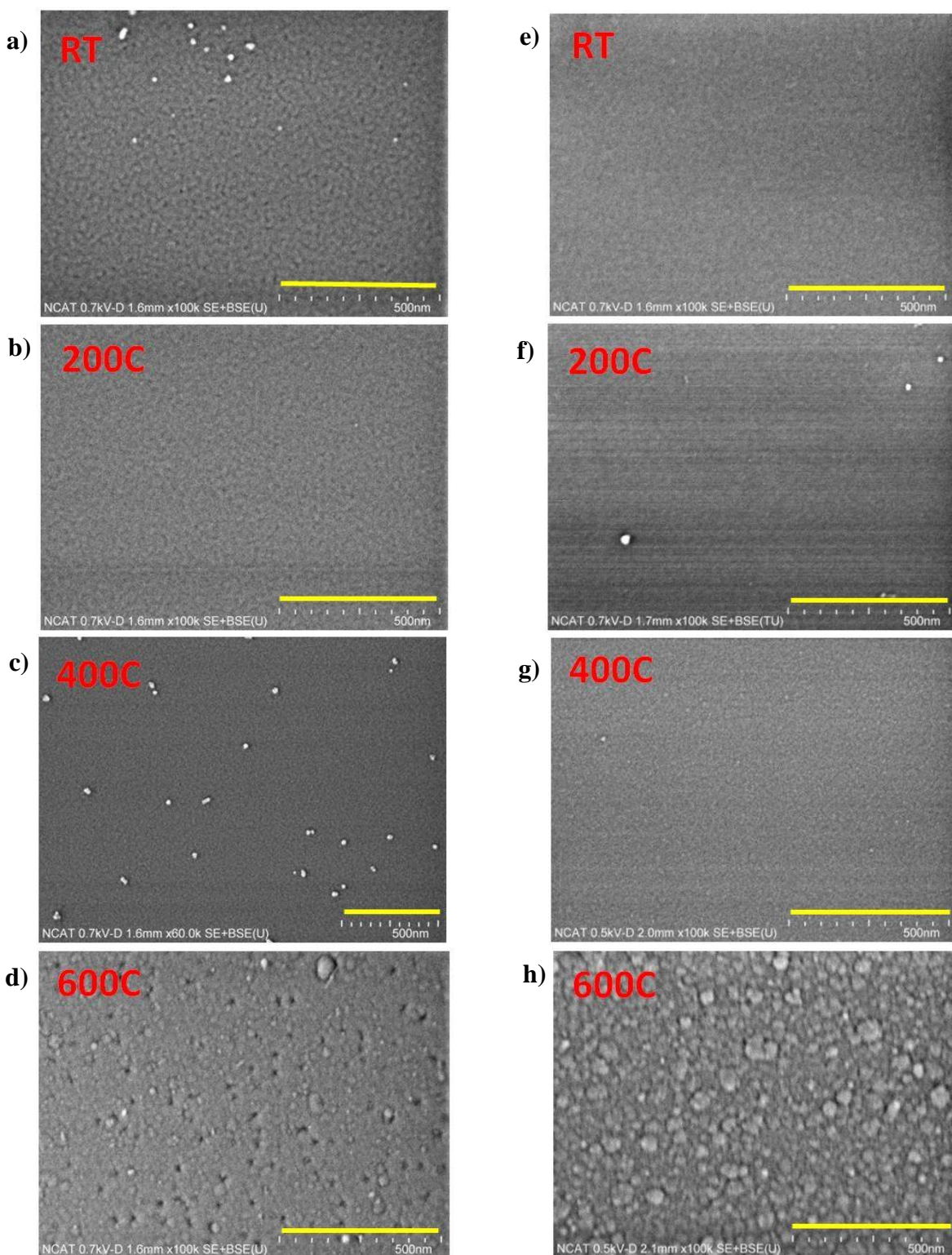


Figure 4.3. SEM images of alumina films deposited by Pulsed DC sputtering at working pressures: a)-d) 2 mTorr and e)-h) 4 mTorr.

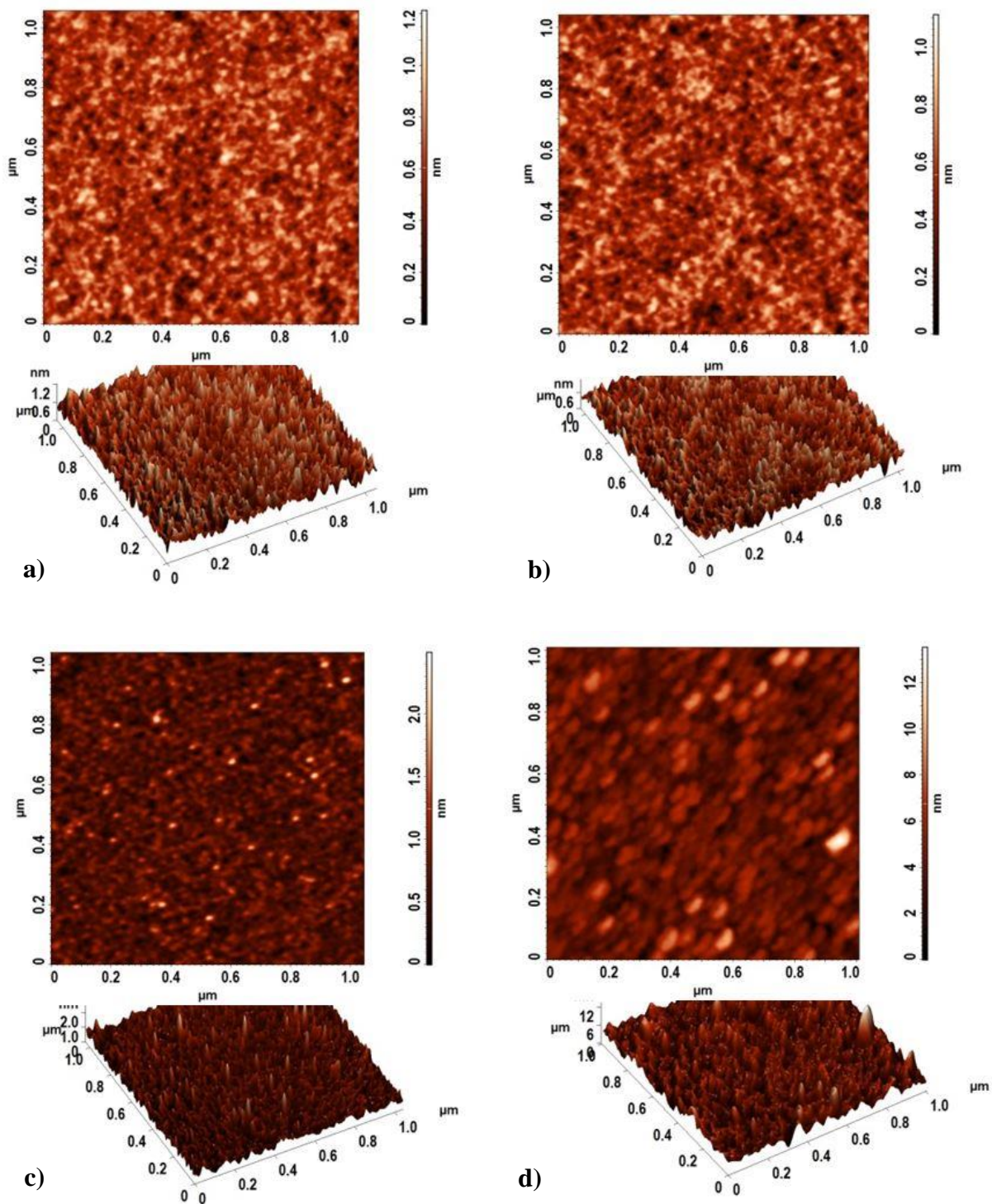


Figure 4.4. AFM study of alumina films deposited by Pulsed DC sputtering at working pressure 2 mTorr, a) at room temperature, and substrate heating at: b) 200°C, c) 400 °C and d) 600 °C.

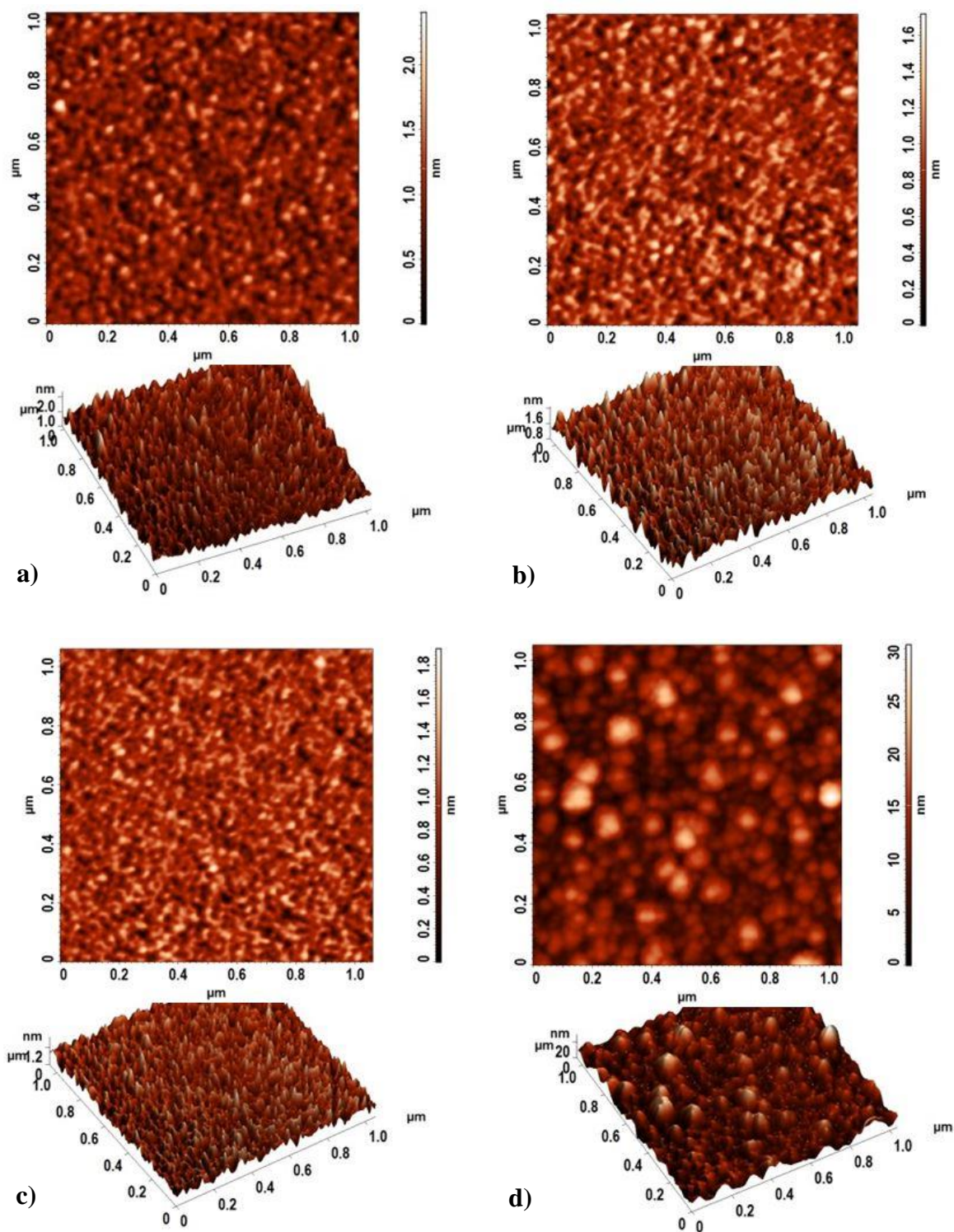


Figure 4.5. AFM study of alumina films deposited by Pulsed DC sputtering at working pressure 4 mTorr, a) at room temperature, and substrate heating at: b) 200°C, c) 400 °C and d) 600 °C.

The AFM study of 10nm thick alumina films deposited by both reactive PDC and RF sputtering methods reveals that the working pressure, power supply, substrate heating and biasing have a significant effect on surface roughness (Figure 4.6). In general, the reactive PDC sputtering produces rougher film, which can be explained by oxygen incorporation into film. The roughness of RF sputtered film increases with the increasing of working pressure and slightly decreases with the applying substrate bias (RF 10W, 96V).

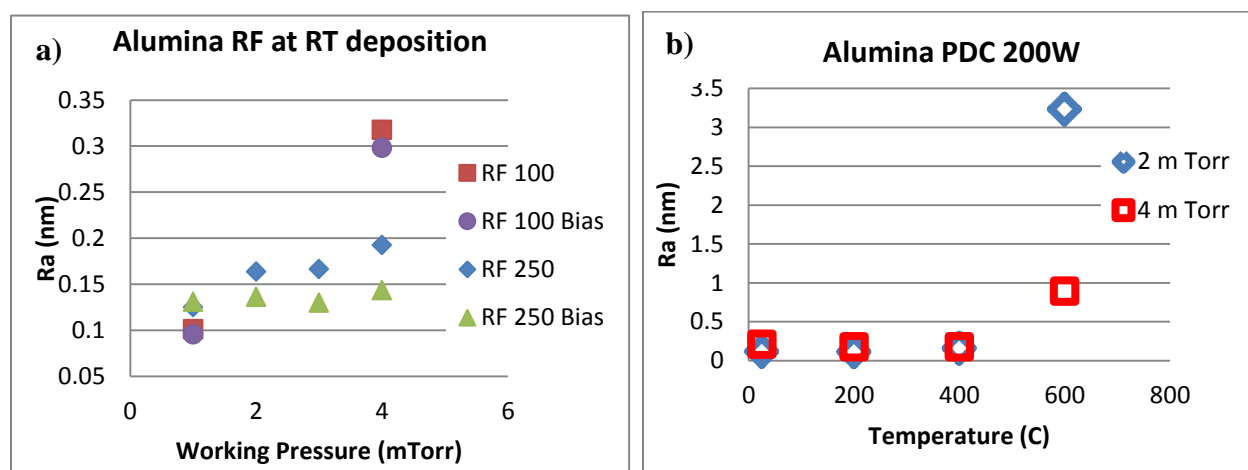


Figure 4.6. Roughness of alumina films studied by AFM: a) deposited by RF sputtering; b) deposited by reactive pulsed DC sputtering.

4.1.2.3 Catalyst deposition. As discussed in chapter 2, the catalyst properties play a significant role in CVD synthesis of CNT. It is believed that catalyst size defines the diameter of CNT and the particle distribution is responsible for density of CNTs' array. In order to determine the effect of deposition pressure and substrate biasing on catalyst properties the AFM study was conducted on Fe-Co catalyst deposited by DC sputtering on 10nm thick alumina films. Figure 4.7 presents the AFM scans of catalyst samples made with super-sharp NSG01_DLC tip, and particles analysis was conducted using NT-MDT Nova software as shown in Figure 4.8. The results show that lower deposition pressure result in closely seeded particles with the size 6 – 12 nm (Figure 4.9).

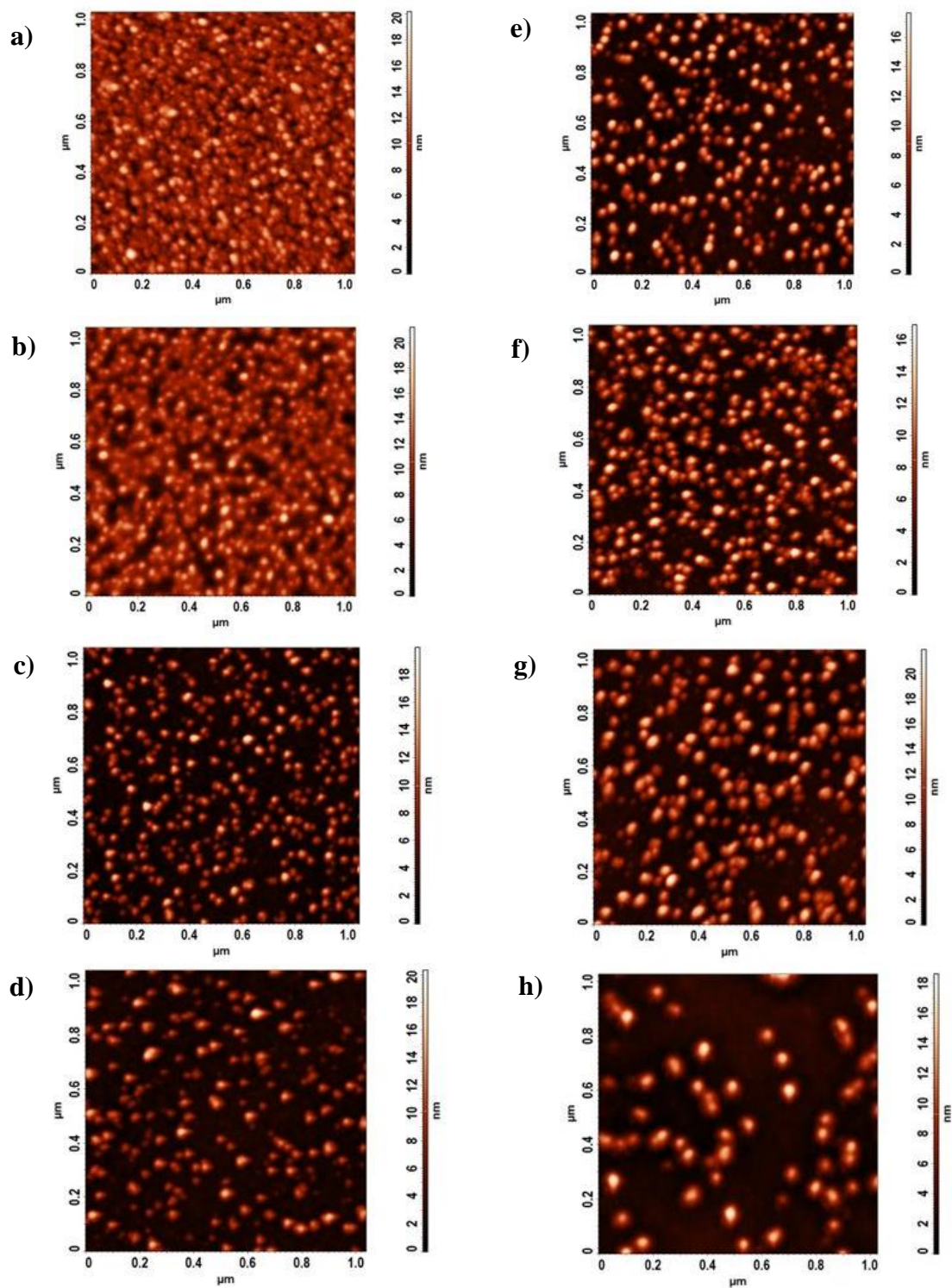


Figure 4.7. AFM study of catalyst deposition. DC sputtering at working pressures a) 1 mTorr b) 2 mTorr, c) 4 mTorr, and d) 6 mTorr; and deposited with substrate bias at: e) 1 mTorr f) 2 mTorr, g) 4 mTorr, and h) 6 mTorr.

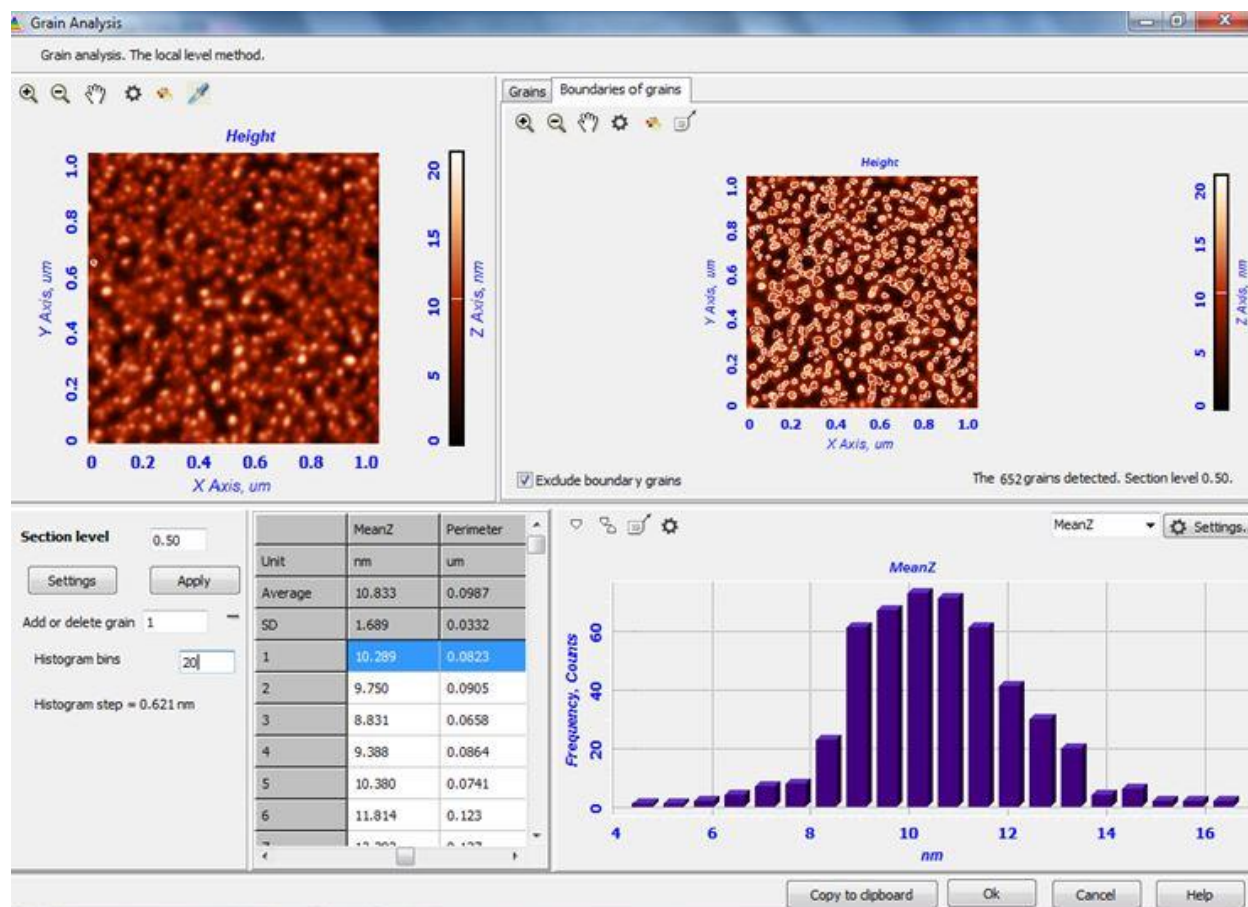


Figure 4.8. AFM particles analysis of deposited catalyst.

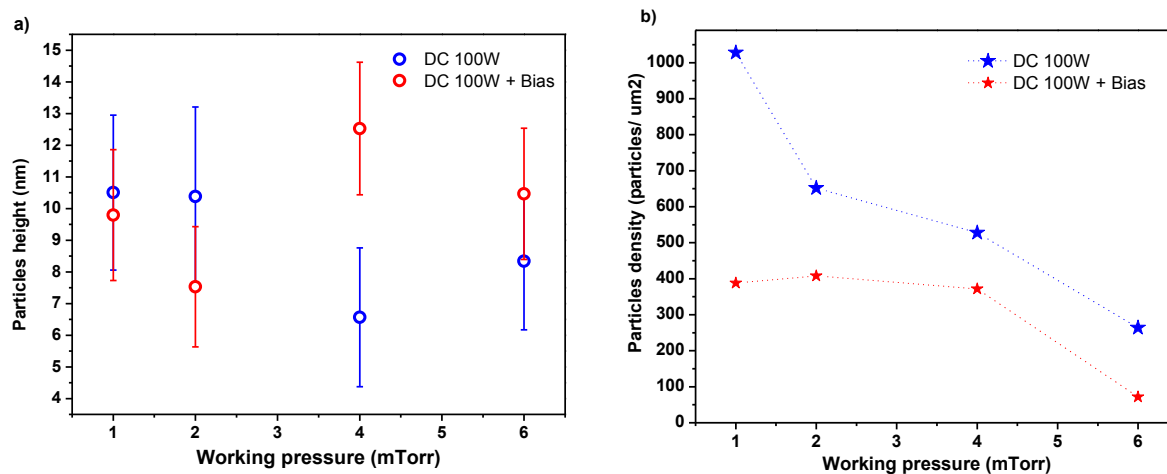


Figure 4.9. Catalyst size (a), and density (b) at different deposition pressure.

4.2 Optimization of Nano-Imprint Lithography Parameters

As mentioned in section 2.4, the quality of thermal imprint process depends on: uniformity and initial thickness of spin-coated thermal resist film; stamp geometry and condition; and imprint temperature, pressure and time.

4.2.1 Spin-coating optimization. The spin-curves for thermal-resists on Si substrates were provided by suppliers with Material Safety Data Sheets (MSDS). In order to check the performance of our equipment and determine the influence of the alumina layer on resist thickness, the resists NRX1025 2.5% and 7% and PMMA mr-I 35k were spin-coated on Si substrate and on 10nm alumina layer deposited by PDC sputtering with the roughness $R_a=0.2$ nm . The resists were spin-coated at various speeds from 2000 rpm to 6000rpm, then after coating, the substrates were baked on a hot plate at 150°C for 5 minutes to remove the residue of solvent. The thickness of resist was measured by XRR technique and profilometry, as described in section 3.4.1. The results of thickness measurements for Nanonex resists, also called the spin-curves are presented in Figure 4.10 for solutions of: a) 2.5% and b) 7%. Figure 4.11 presents the spin-curve for PMMA mr-35k thermal resist on pure Si substrate and on substrate with 10 nm of alumina layer. The presence of alumina layer increases the polymer thickness by 10-20%. The higher spin speed the thinner layer of thermal resist can be achieved; however, the uniformity of coating is better in a range 2000-4000rpm. The 2.5% NRX1025 resist can be spanned down to thickness of 40 nm which is very important for imprinting with no residual layer.

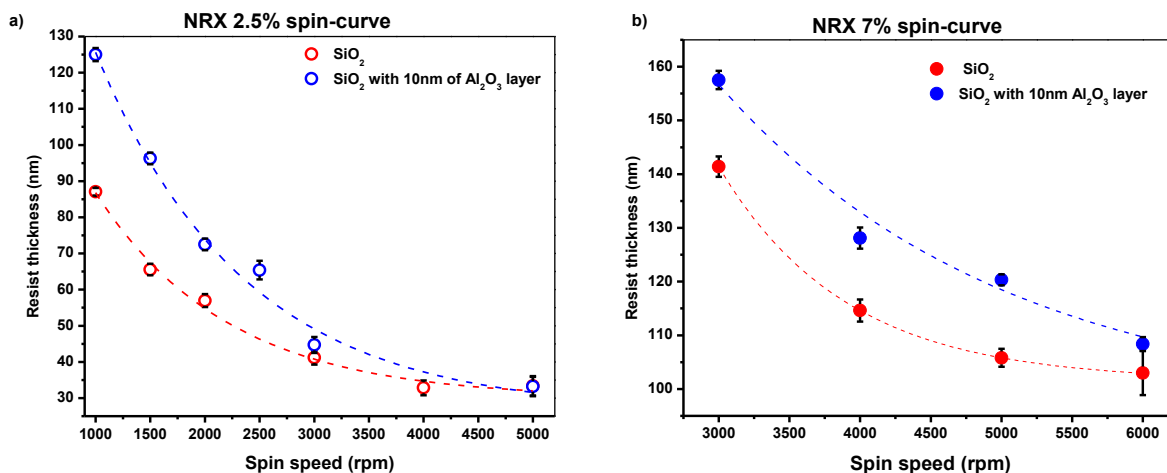


Figure 4.10. Spin-curves for NRX1025 thermal resist from Nanonex.

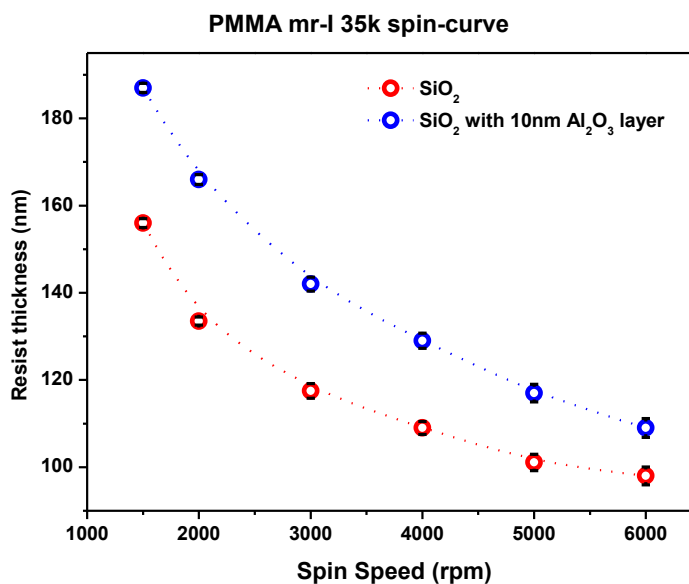


Figure 4.11. Spin-curves for PMMA mr-I 35k thermal resist.

4.2.2 Stamp cleaning and release agent deposition. In order to prevent resist sticking to the stamp during imprint process, the stamps are coated by release agent. Commonly it is thing molecular layers of hydrophobic polymer that has a good adhesion to the stamp material and prevents sticking resist to stamp and improves substrate-stamp separation process after imprinting. After about 200 imprint cycles the stamps require cleaning and re-application of

release agent, some stamp suppliers sell stamps without coating or charge extra 10-20% for it. To avoid an extra cost for cleaning and release agent deposition, the simple setup for vacuum deposition was built (Figure 4.12).

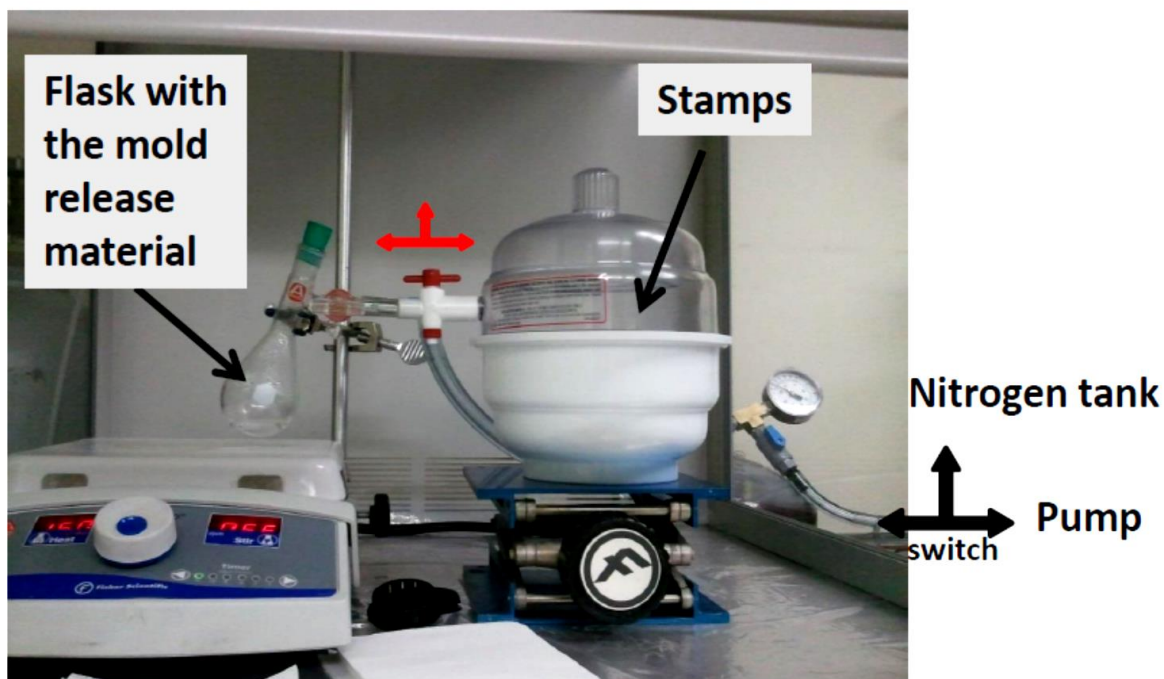


Figure 4.12. Setup for vacuum deposition of mold release agent.

The procedure for stamps' cleaning and release agent deposition includes following steps:

1. Stamps cleaning: plasma cleaning to remove the residue of resist and old mold release materials.
2. Surface activation: "pirana" solution bath at 90°C for 30minutes
3. The deposition system were vacuumed and flushed with the N2 couple times.

Clean and "activated" stamps and pieces of silicon wafer were placed into desiccator and dried out for 2 hours (vacuuming and flushing with N2 every 15 minutes).

4. Deposition: flask with mold release (NRX 110) was heated on air bath at 150°. First 15 minutes the solvent was evaporated (flask connected to pump), then flask connected to vacuumed desiccator and the mold release deposited for 5 minutes.
5. Stamps/silicon placed on a hot plate 90°C for 3 minutes to cure the mold release and remove the excess of solvent.

The quality of release agent coverage was checked by wetting of pieces of silicon substrate with DI water (Figure 4.13). The 10 minutes of deposition is enough to fully cover the surface of stamp.

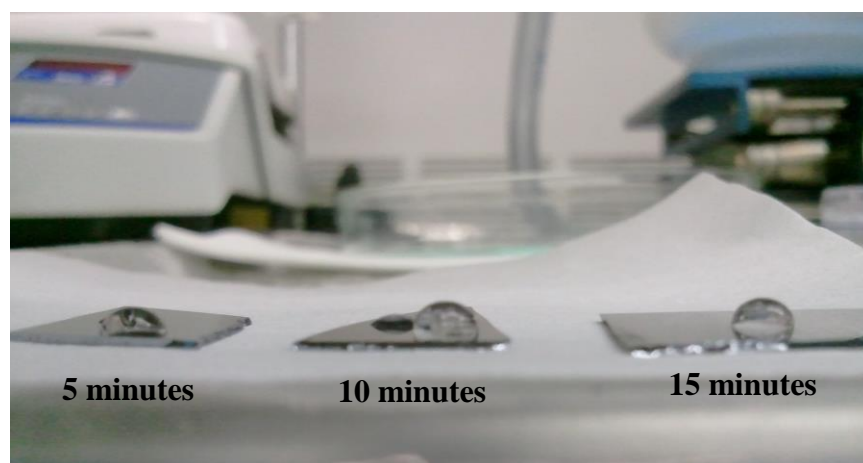


Figure 4.13. Drops of DI water on pieces of silicon before and after 5, 10 and 15 minutes of deposition of release agent.

4.2.3 Imprint time and temperature optimization. For thermal resist NRX1025 2.5% and 7% the recommended by supplier imprint parameters are: imprint temperature is 120-150 °C, pressure of 120psi and 1 minute imprint time. The test imprint was conducted with the stamp lines 100nm, at 140 °C, 120psi for 45, 60 and 90 seconds. The residual layer was measured by AFM on a scratch Figure 4.14. The results show that the imprint time should be at least 1 minute.

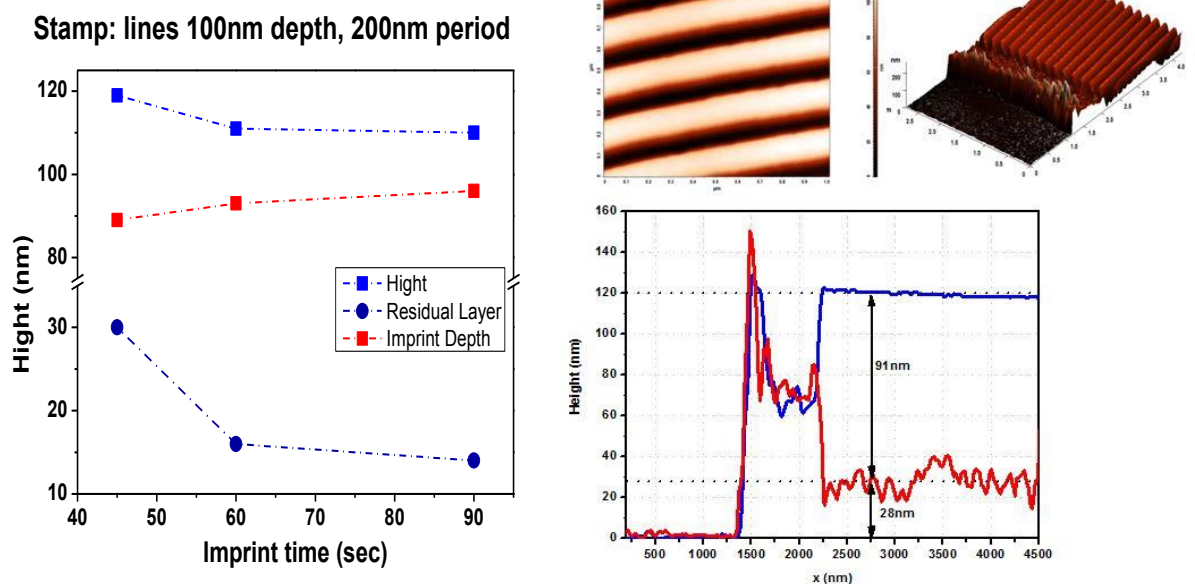


Figure 4.14. AFM study of imprint patterns on silica substrate.

For thermal resist PMMA the recommended by supplier imprint parameters are: imprint temperature is 160-180 °C, pressure of 50 bar (equivalent of 725 psi) for 1 minute imprint time. The Nanonex 2000 imprint machine is limited to the imprint pressure of 250 psi and maximum imprint time of 5 minutes. Based on theoretical background described in chapter 2 and given rheological data for PMMA from (Scheer et al., 2008; Yu et al., 2002), the behavior of residual layer was modeled for line, post and hole stamps using simple excel worksheet and formulas 2.3-2.6, presented in sections 2.4.2-3. The PMMA viscosity recalculated using data from Scheer et al.(2008) and presented in Figure 4.15. The modeled curves of resist layer change for line and post stamps (Appendix A) are presented in Figures 4.16 and 4.17. The modeled curve for imprint with stamp with the holes features is presented in Figure 4.16; the graph includes the test data (details of test provided below). As could be seen, there is a big difference between model and observed data, more than 20%. The reasons as mentioned in section 2.4.1.1 could be: difference in rheology of bulk and thin film of PMMA and/or the stamp defects that can change geometry.

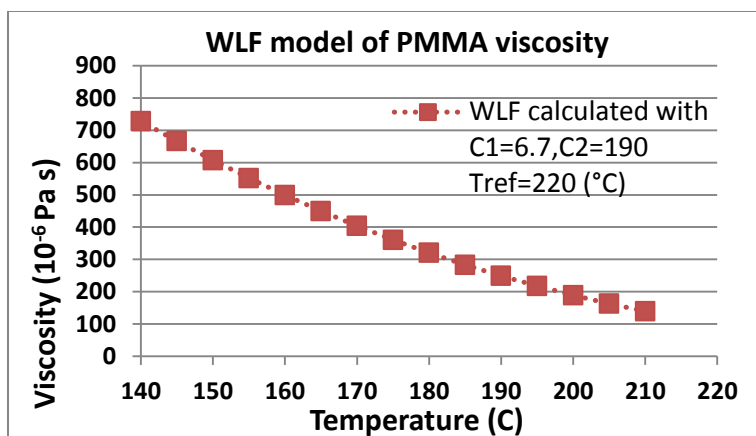


Figure 4.15. Calculation of PMMA viscosity using WLF model.

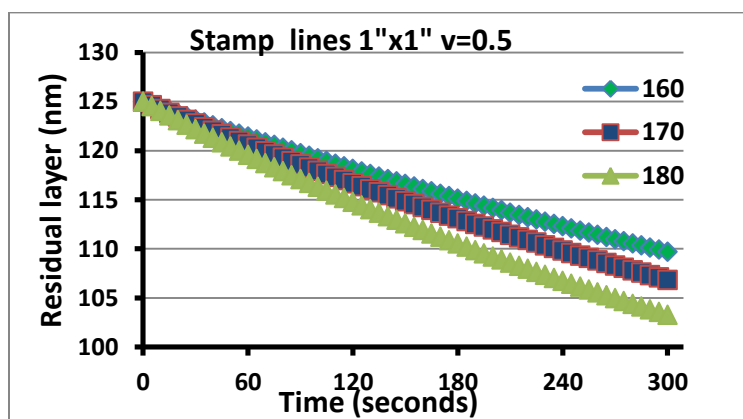


Figure 4.16. Model of residual layer thickness change during imprint of PMMA resist with the lines stamp at different temperature regimes.

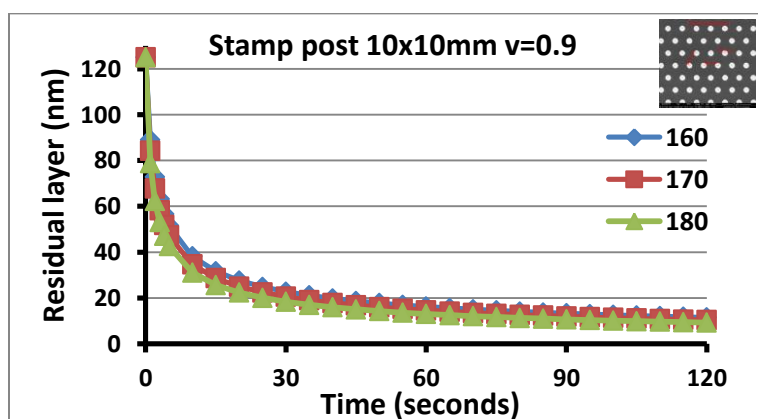


Figure 4.17. Model of residual layer thickness change during imprint of PMMA resist with the post stamp at different temperature regimes.

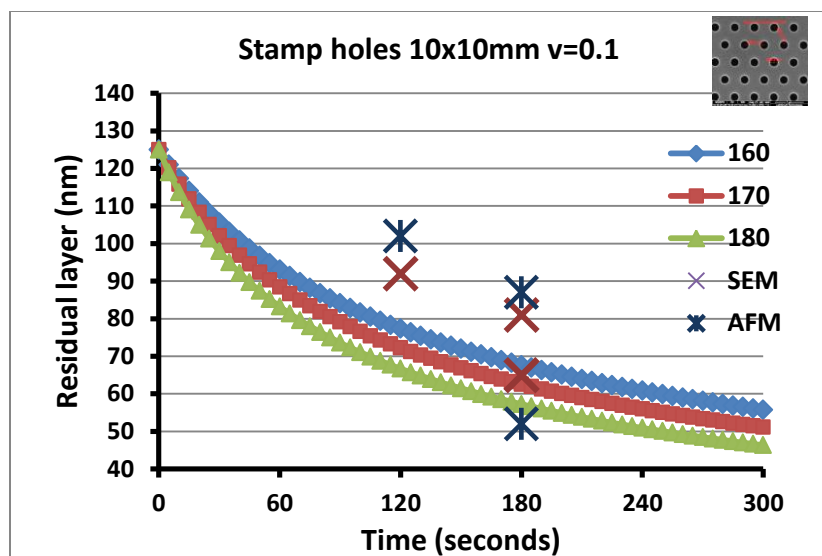


Figure 4.18. Model of residual layer thickness change during imprint of PMMA resist with the stamp with holes at different temperature regimes (model and measured data).

The following experiment was conducted to find the optimum time and temperature for imprinting of PMMA resist: resist was spin-coated on 4" Si wafer at 2500 rpm, which gives an initial thickness of resist layer of 125 nm (Figure 4.11); then wafer was cut into pieces and used for imprinting by stamps with the line features 500 and holes 290 nm. The imprint parameters are given in Table 4.2:

Table 4.2.

Imprint process parameters.

#	Substrate	Resist	Pump time (min)	Pre-processing		Imprint		
				Pressure (psi)	Temperature (°C)	Pressure (psi)	Temperature (°C)	Time (sec)
1	Si	PMMA 125nm	7	100	165	225	170	180
2	Si	PMMA 125nm	7	100	155	225	160	120
3	Si	PMMA 125nm	7	100	155	225	160	180

In order to determine the residual layer of imprinted resist the surface was scratched with the sharp and soft needle and then analyzed with the AFM (Figure 4.19 and Appendix C). For the imprinted PMMA samples additional SEM analysis of the cross-section were conducted. The comparison of AFM and SEM measurements are given in Appendix C, the results obtained by both methods are in a good agreement (the difference between methods from 5 to 10 nm with the measured thicknesses within a range of 50 to 130 nm). The results shows that the optimal conditions for PMMA imprint are: imprint temperature above 160 °C and imprint time no less than 3 minutes.

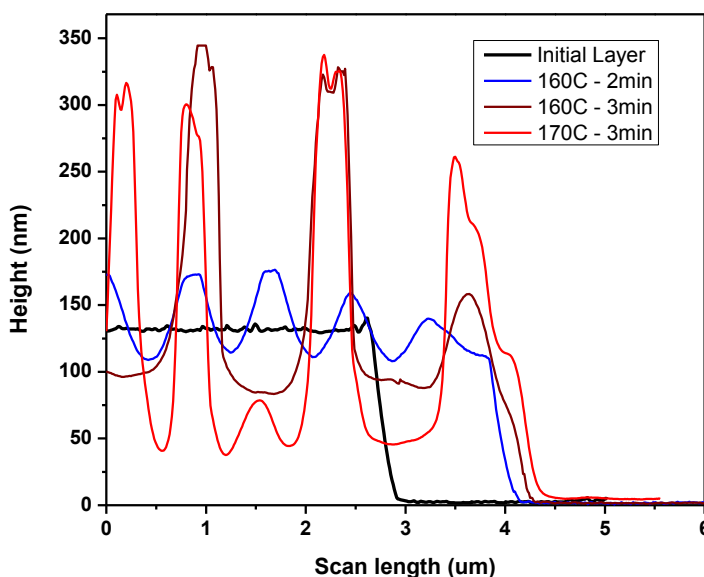


Figure 4.19. AFM studies of PMMA imprint optimization.

4.3.2.1 Effect of thermal resist type and stamp geometry on imprint quality. As discussed in section 2.4 the resist properties (molecular weight and viscosity) are defining the imprint parameters and achievable imprint resolution. As could be seen from Figure 4.20 (a) and (c) the NRX1025 resist shows better uniformity of imprint than PMMA when imprinted with the 70 nm line stamp on Si substrate. The viscosity of PMMA is lower than NRX1025, so the longer time is required for PMMA resist to fill the cavities of stamp. In addition, increasing imprint

temperature can improve the imprint uniformity, but on the other side it initiates cross-linkage of resist (over-curing) and causes problems with the lift-off procedure as discussed further in section 4.4.

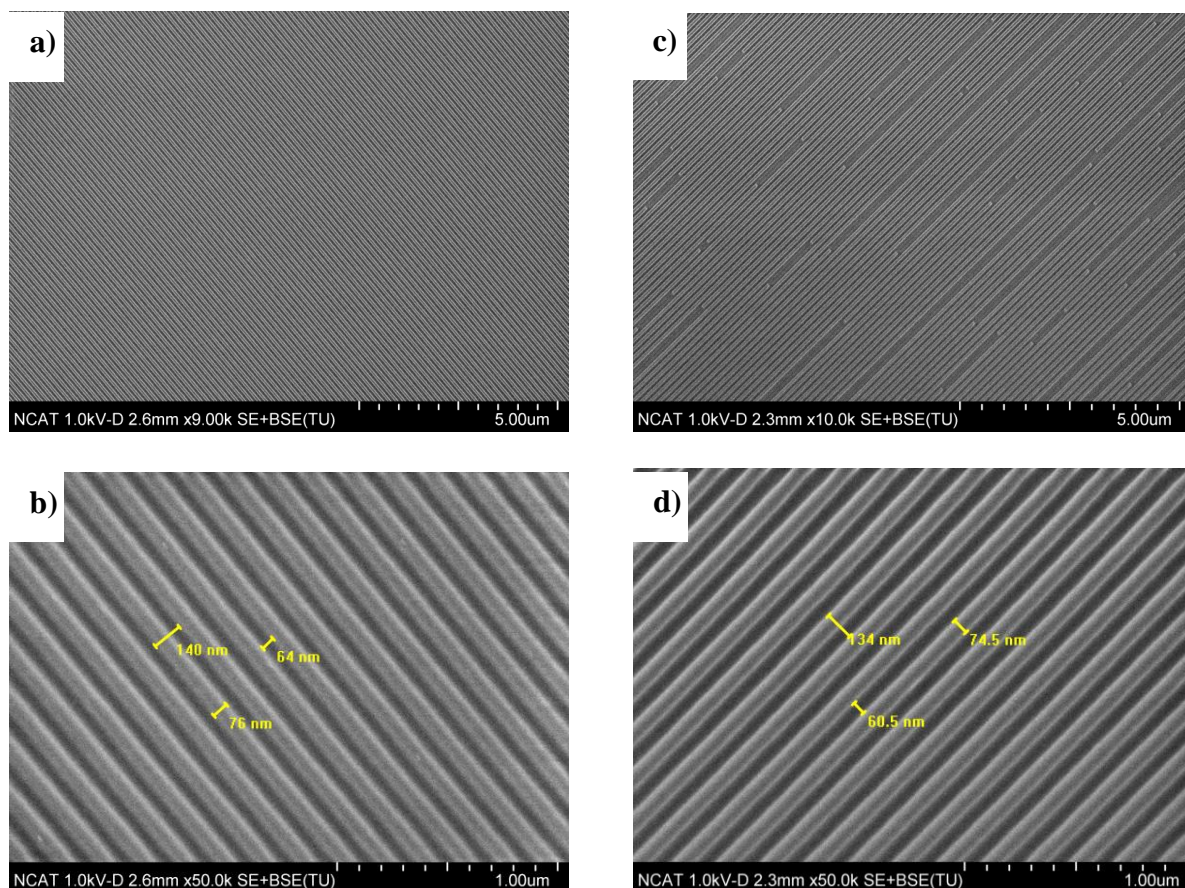


Figure 4.20. Imprint patterns on silica substrate with the 70 nm line stamp: a), b) – low and high magnification of NRX1025 2.5% resist and (c), (d) –PMMA resist.

The stamp geometry (filling factor v and imprint area) should be considered when choosing the resist material NRX or PMMA. The good uniformity and an excellent pattern replication were achieved on PMMA resist imprinted with the stamp NSSP33 with the features size of 50nm at imprint temperature of 170 °C. The SEM images and AFM scans are presented in Figure 4.21. At the same time, the attempt to achieve 20 nm limits using both thermal resists was

not successful at current laboratory setup (Figure 4.22); it's believed that using special tools for stamp –substrate alignment and de-molding process will solve this problem.

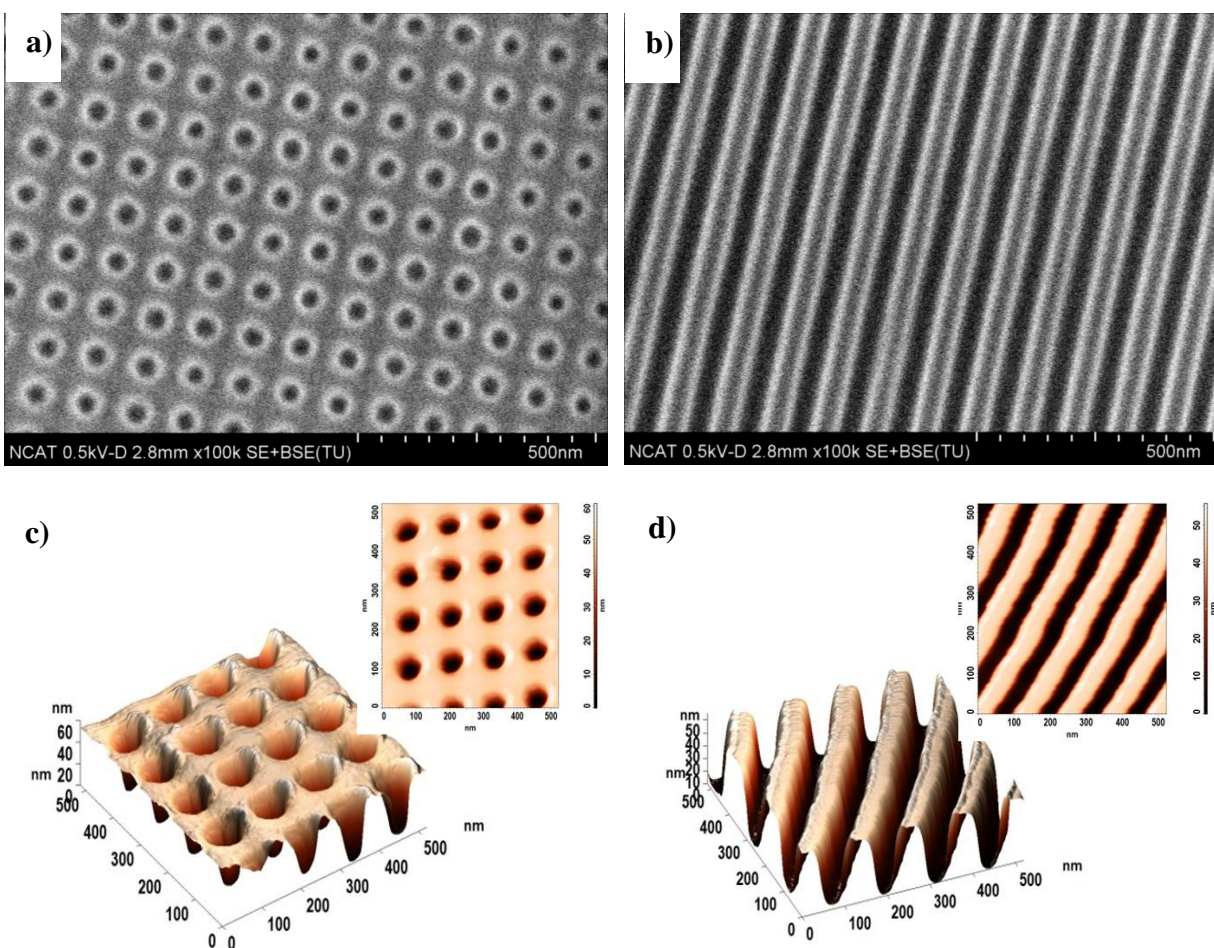


Figure 4.21. Imprint patterns on silica substrate with the NSPP33 stamp: SEM image of two imprint areas 5x5 mm, (a) holes from posts and (b) –lines replication, (c) and (d) – AFM images of holes and lines.

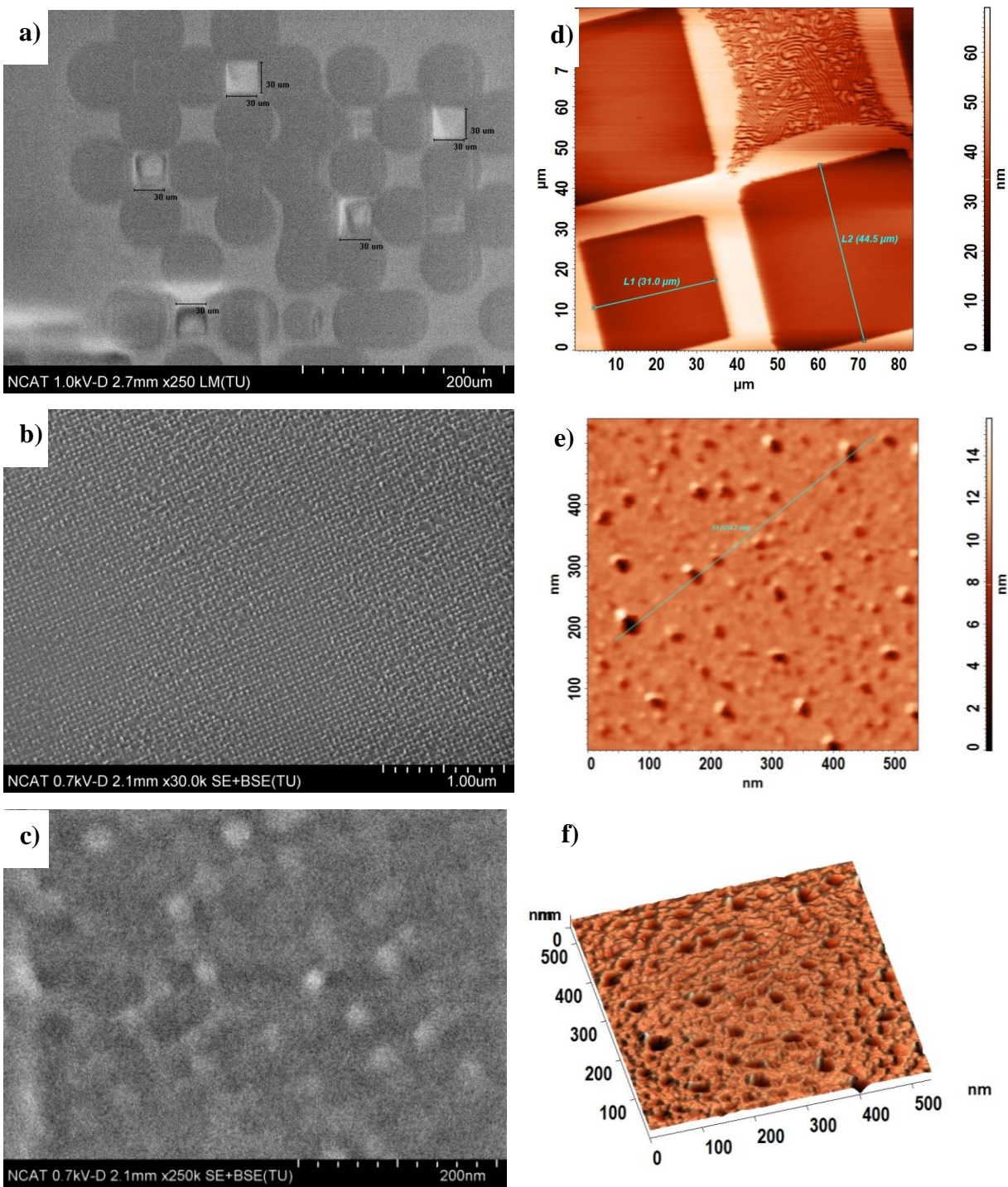


Figure 4.22. Imprint patterns on silica substrate with the stamp features 20nm, imprint areas 30x30 microns: (a - c) SEM images (d-f) – AFM study of imprinted pattern.

4.3.2.1 Effect of alumina layer on imprint quality. Addition of the layer of alumina to silica substrate not only changes the roughness of substrate which affects the spin-coting process, it is also slow down the heating of the resist during the pre-processing due to high thermal resistance of alumina. Figure 4.23 illustrates the difference on imprint quality for PMMA resist imprinted on Si/SiO₂ substrate and substrates with alumina layer imprinted with the line stamps of d 100 nm features. This problem can be easily solved by increasing the imprint temperature by 5-10°C.

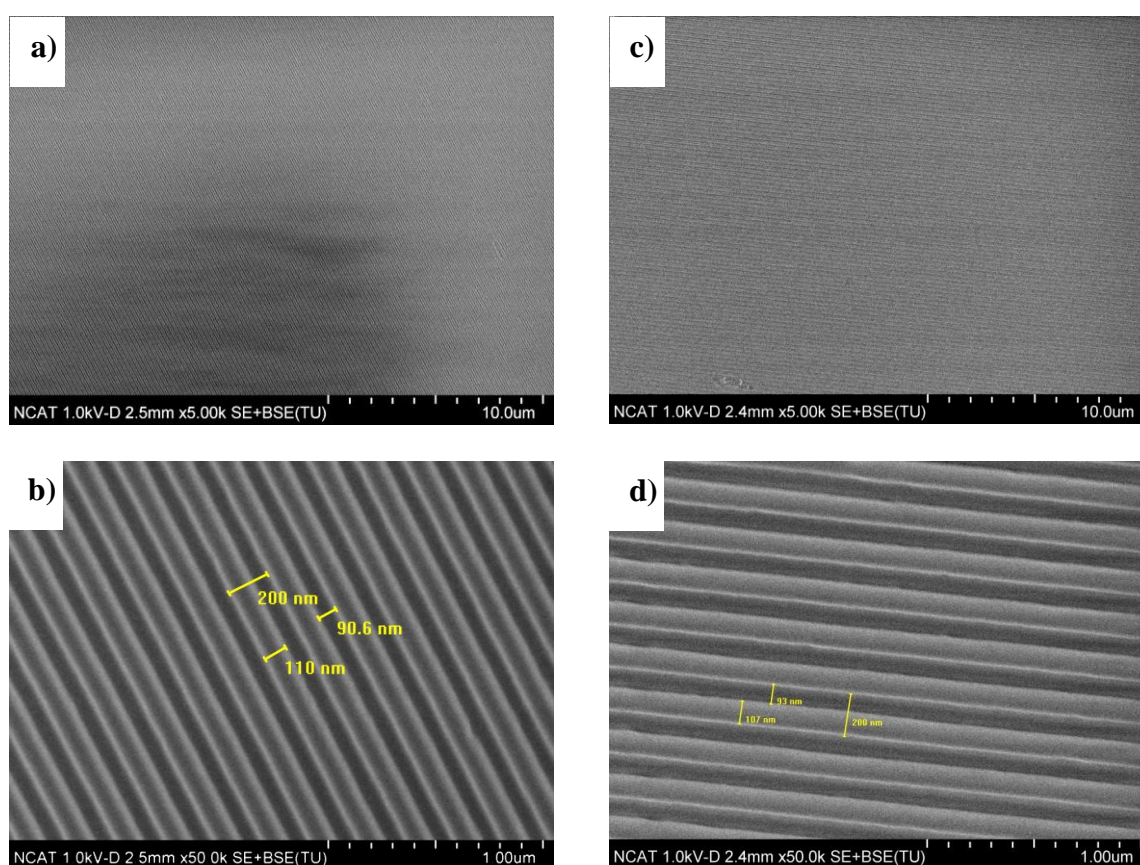


Figure 4.23. Imprint patterns for PMMA resist with the 100nm lines stamp on: a), b) Silica substrate and c), d) substrate with the alumina layer of 10 nm.

4.3 Optimization of Reactive Plasma Etching

The etching rates for thermal resist were determined by measuring thickness of spin-coated films using XRR methods and on imprinted samples using AFM. The effect of pressure, applied power and oxygen content in reactive gas mixture were evaluated.

As seen in Figures 4.24 and 4.25, the etching rate of thermal resist directly proportional to the applied power and inversely proportional to pressure. Increasing the oxygen content in actually decreasing etching rates, the similar effect was observed by Hartney et al. (1988) . The PMMA resist has lower etching rate than NRX.

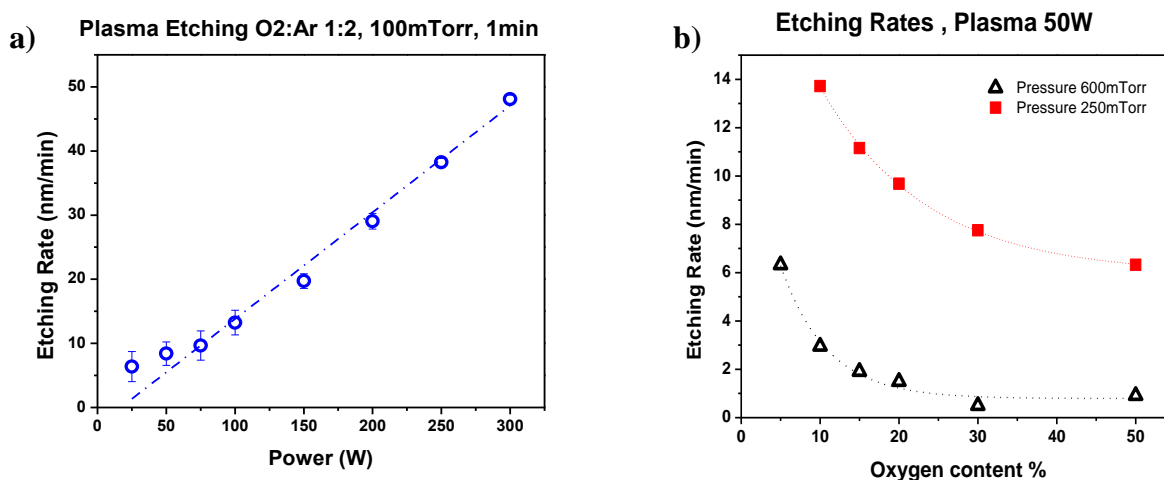


Figure 4.24. Plasma etching rates for NRX1025: a) effect of plasma power b) effect of oxygen content.

The AFM scans of imprinted and etched samples reveals additional effect of plasma etching process on a resist. As seen in Figure 4.26, the resist undergo extra curing under plasma and the polymer chains become clearly visible and someone could detect that the cross-linkage occurs. The over-curing and cross-linkage of resist were found undesirable for the lift-off process of further sample processing.

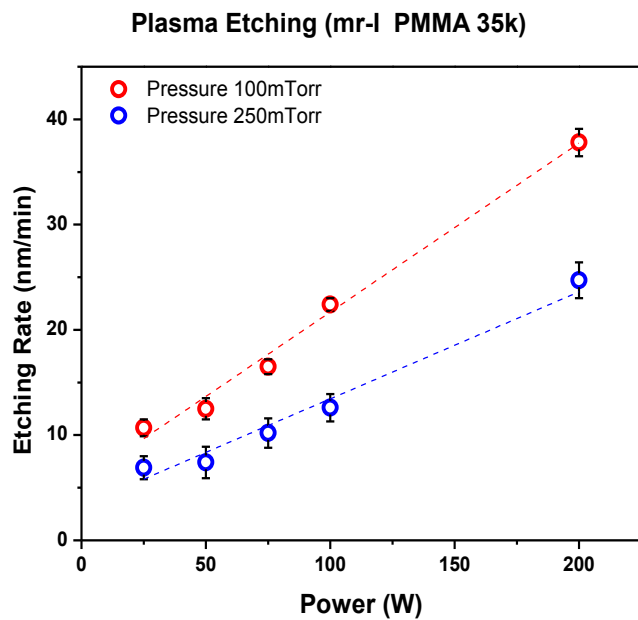


Figure 4.25. Plasma etching rates for PMMA.

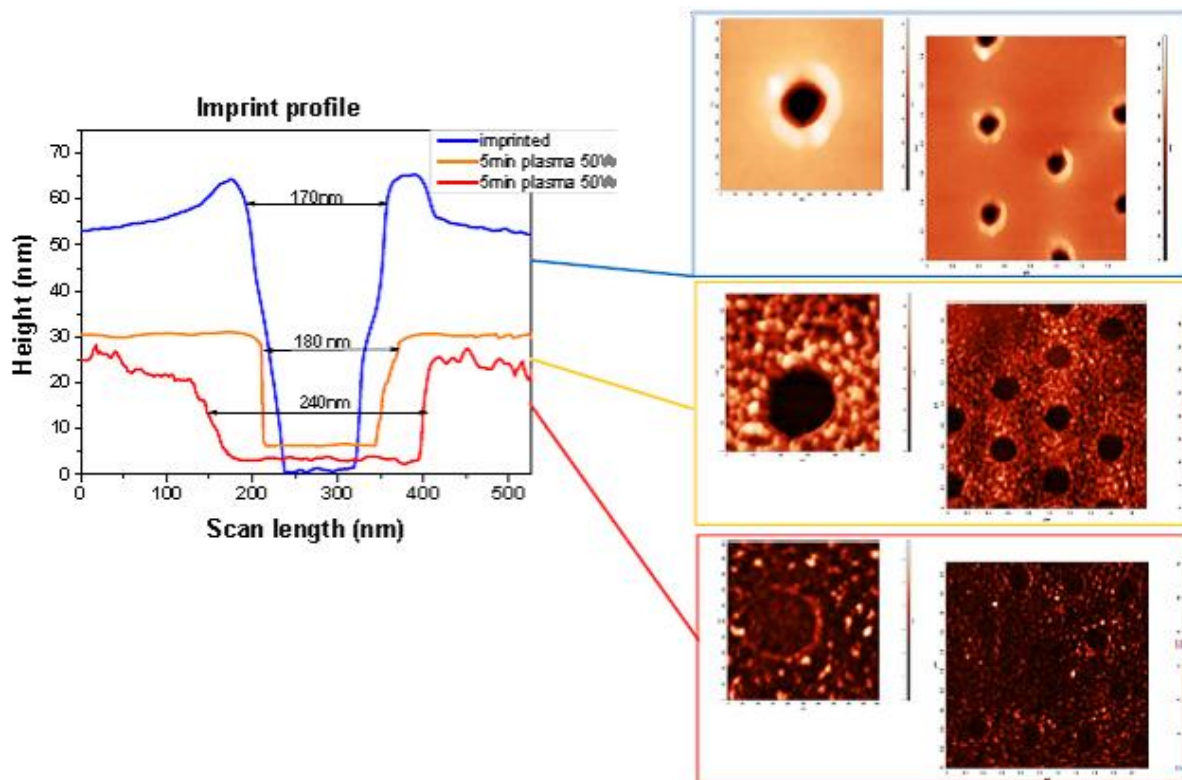


Figure 4.26. AFM study of plasma etching effect.

The AFM and SEM analysis of plasma etched samples confirms that the process is unidirectional and in order to maintain the desired planar sizing of pattern it should be minimized. The other undesirable effect of plasma etching process on pattern were found by observing large areas of processed samples is the spots where the charge accumulated and local charge brake-thought occurs (Figure 4.47 c). To avoid the negative effects of the process the etching should be conducted at the lowers possible pressure and power, for a short time. Thus the near-zero residual layer imprint process are highly desired.

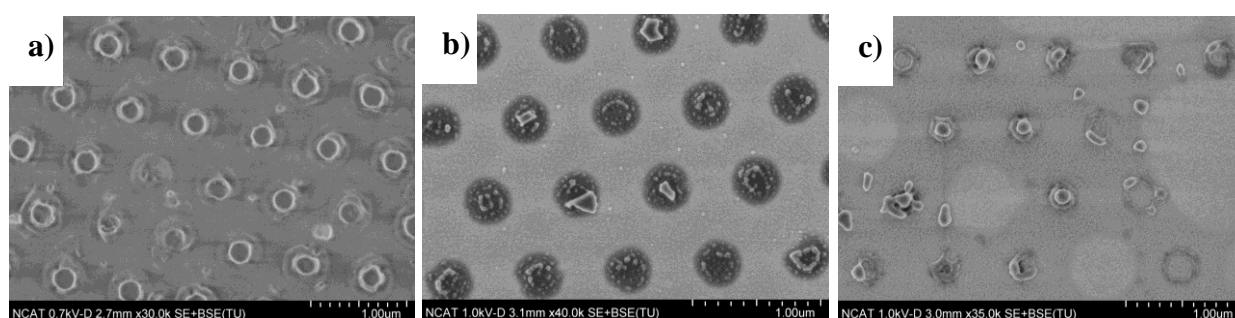


Figure 4.27. SEM study of plasma etching effect a) imprinted; b) etched at for 5 minutes; c) etched for 8 minutes.

4.4 Optimization of Lift- off Procedure

The lift-of process results is a final stage of sample processing. During the process the leftovers of thermal resist are dissolved using chemical solutions at the same time those solution should not affect patterned material. Sometimes this process requires additional treatment such as heating, wiping or ultra-sonic cleaning. The recommended (based on MSDS) lift-of solutions are: acetone or mixture of ammonia and hydrogen peroxide and water (1:1:5) solution. It was found out that for successful results the acetone should be a semiconductor (SMOS) grade, otherwise the samples became contaminated and resist residue poisoning the catalyst during the synthesis in CVD chamber. The heated ammonia in general shown better results than acetone, but the process require longer time of 30 minutes and also suffer from contamination effect. The

sonic cleaning in acetone solution removes the catalyst together with the resist residue. The best results were obtained with gentle wipe with the Chemtronics Foamtips™ tip while sample stay in acetone, followed by rinsing with the fresh acetone Figure 4.28.

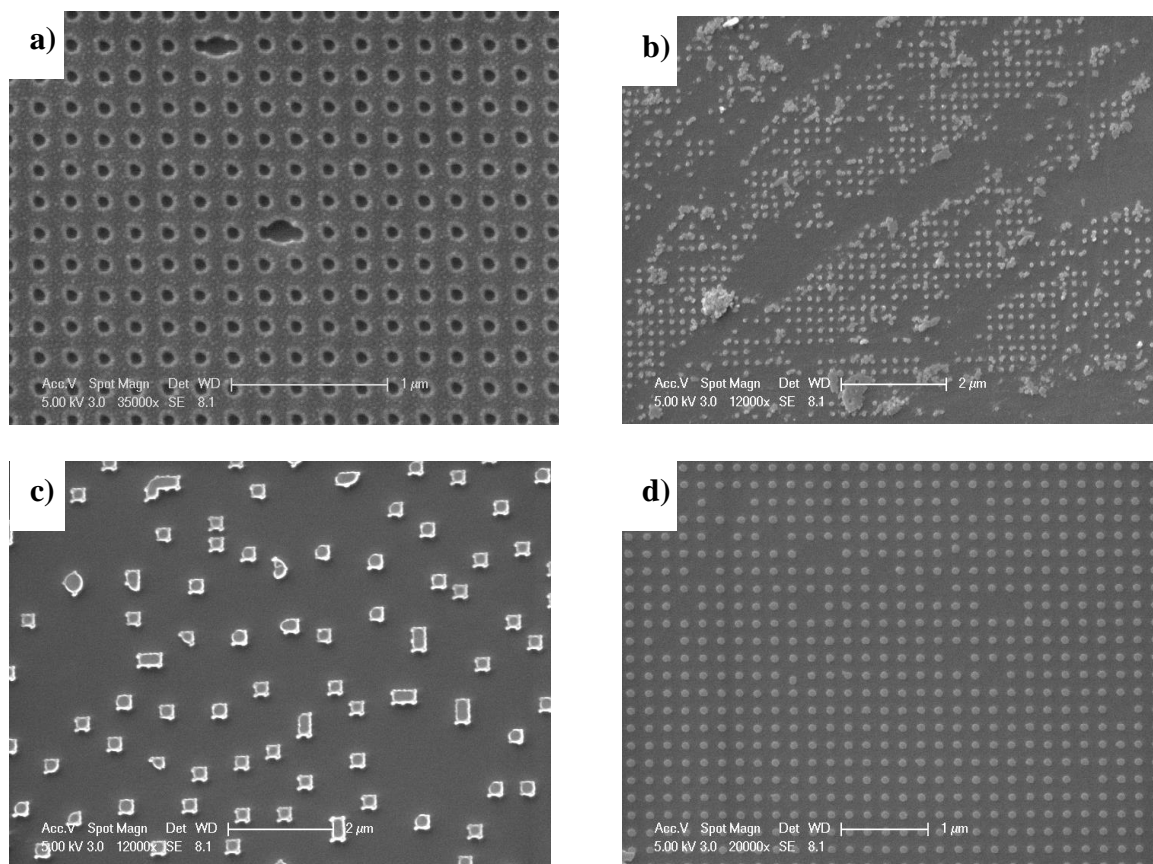


Figure 4.28. SEM study of lift-off process a) imprinted; b) ammonia solvent; c) ultrasonic and d) wipe-off methods.

It was also noticed that lift-off was difficult for the samples with the over-cured resist imprinted at high temperature and/or etched at high power or stored for a long time as shown before. Thus, in order to achieve the best quality of pattern the following processes parameters should be taken into consideration:

- ✓ Imprint at a lowest possible temperature with the time enough to reach zero-residual layer imprint

- ✓ Avoid high-power and long-time plasma etching
- ✓ Process samples immediately, avoid storage of semi-finished products

4.5 Three Process Approaches to Pattern Catalytic Surface

4.5.1 Overview of 3 process approaches. The general processes steps are presented in

Figure 4.29. Details about each approach discussed below.

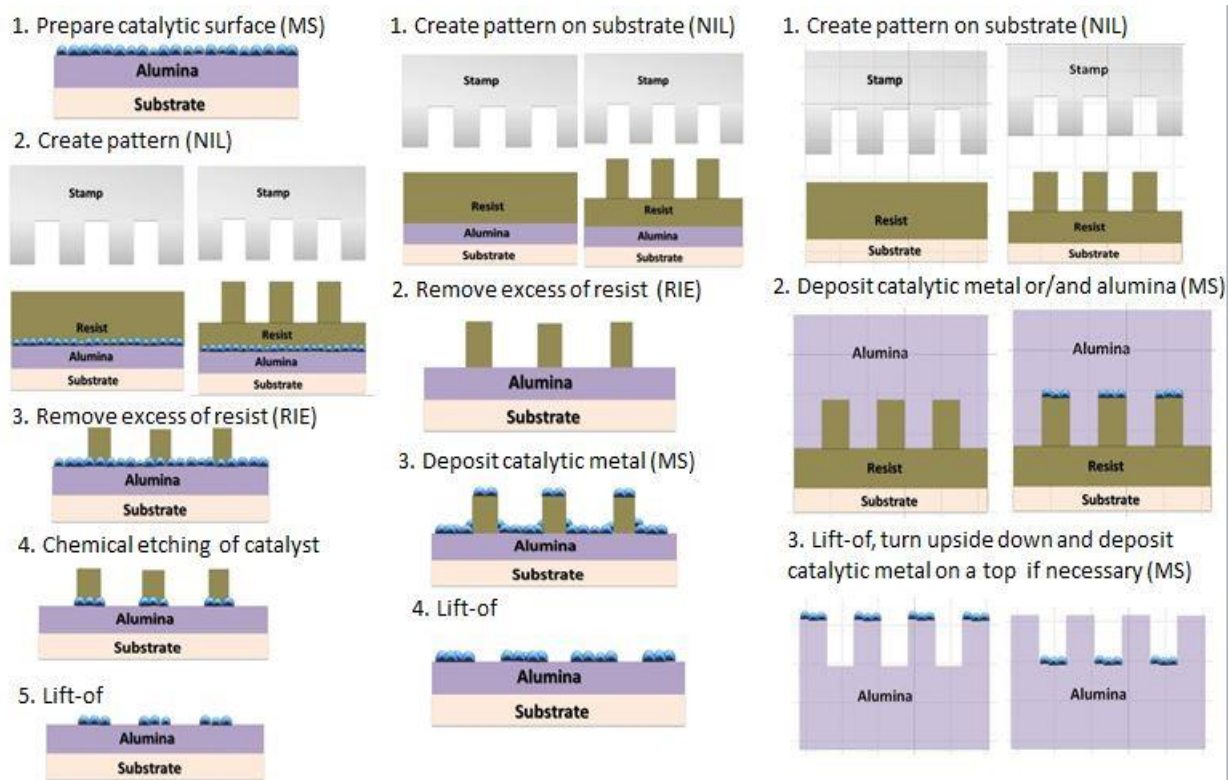


Figure 4.29. Schematic of three process approaches.

4.5.1 Approach 1. The sequence of processes: 1) deposition of alumina and catalytic metal; 2) resist spin-coating and imprint, 3) plasma etching to remove residual layer of resist and open substrate surface; 4) chemical etching with the ceramic etchant; 5) lift-off at the final step. With this combination of process steps we obtain “negative” pattern of catalyst on a substrate. Figure 4.30 is an example that the catalyst pattern can be transferred with good precision. The sample was prepared with the 100 nm lines stamp imprinted on PMMA resist on substrate with

the 10 nm alumina and 2 nm Fe; etched for 2 minutes at 100W and 100 mTorr, lift-off done by wiping with the Chemtronics Foamtips™ in the acetone. Most of the produced samples had patterns' size varying from the stamp dimensions.

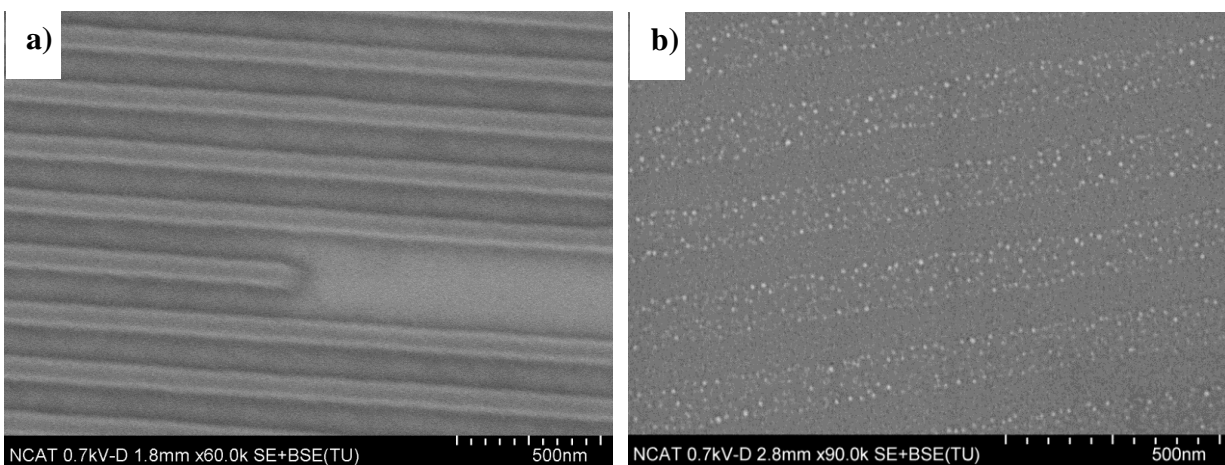


Figure 4.30. Imprinted substrate (a) and (b) catalyst pattern made by first approach.

4.5.2 Approach 2. The sequence of processes 1) resist spin-coating and imprint; 2) plasma etching to remove residual layer of resist and open substrate surface; 3) deposition of alumina and catalytic metal and final step is 4) lift-off procedure. With this combination of process steps we obtain “positive” pattern of catalyst on a substrate. Figure 4.31 represents the CNT pattern on a substrate made by approach #2. It can be clearly seen that the catalyst lines have thinner width than original pattern: the width varies from 50 nm to 75 nm, as the period of pattern stays 200 nm. The sample was prepared with the 100 nm lines stamp imprinted on PMMA resist on Si/SiO₂ substrate and plasma-etched for 5 minutes at 100W and 100 mTorr, then with the 10 nm alumina and 2 nm Fe was deposited on ; and lift-off done in ammonia-hydrogen peroxide solution, then rinsed by acetone.

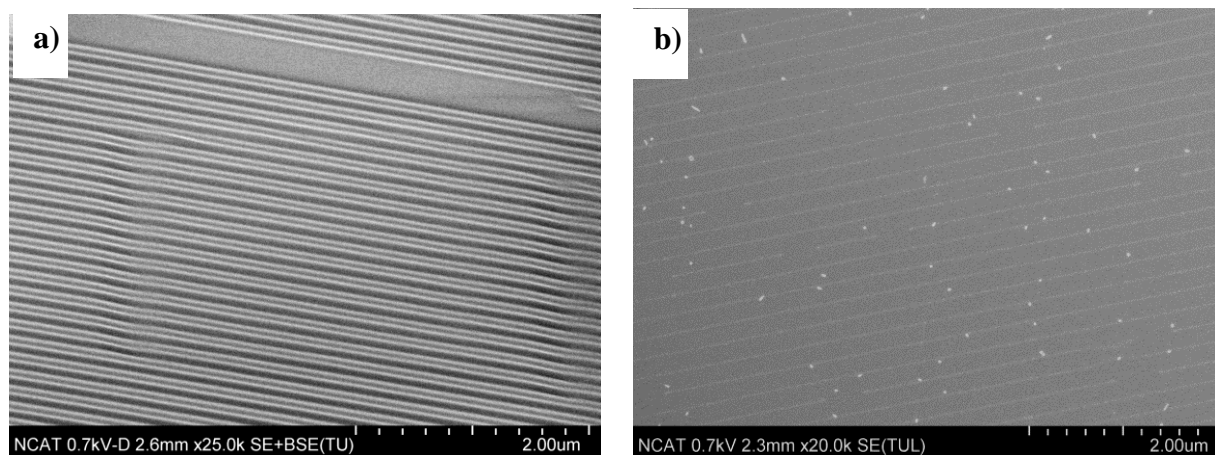


Figure 4.31. Imprinted substrate (a) and (b) catalyst pattern made by second approach.

4.5.3 Approach 3. The two approaches use a plasma etching process to remove the residue of resist and open the substrate surface for further deposition of catalyst or chemical etching of catalyst that was deposited before patterning. The major drawbacks of using plasma etching are: over-cure the resist that brings the further difficulty of lift-of procedure and non-uniformity of etching (plasma/charge sparks that burn the substrate). We found the way to avoid plasma etching step in substrate patterning process. The benefits of new approach:

- ✓ Less steps process
- ✓ No need in plasma etching (no over-cured polymer)
- ✓ No need in thin layer of thermal resist (easier spin-coating) and substrates can be re-used many times with appropriate cleaning procedure.
- ✓ The product is exacts replica of stamp.

As shown in Figure 4.32, the pattern quality is outstanding; replicating almost exacts dimensions of stamp pattern.

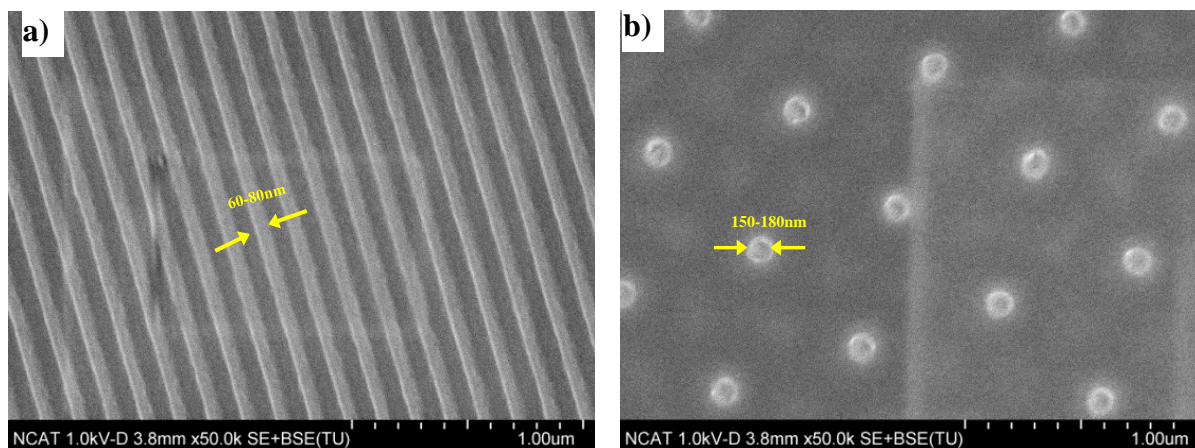


Figure 4.32. The catalyst patterns: a) imprint with the line stamp (70 nm, 143 nm period); b) imprint with the post stamp (160 nm, 500 nm period).

After first try-out we found that the disadvantage of this approach is difficulty to manually operate with the sample during the lift-off. After dipping in acetone the film easily separates from substrate but it breaks easily by touching it with the tweezers. Instead of tweezers we tried a copper tape, stick it to the top and then separate film from substrate Figure 4.33. The copper tape can be used as an electrical connector of future device, but unfortunately the Cu by itself acts as a catalyst for CNT growth and interferes with Fe catalyst during CNT synthesis. In addition, there is a big difference in thermal expansion coefficients of alumina and copper which results in cracks development at the synthesis temperature and brake the pattern (Figure 4.34-a). The results of CNT synthesis presented in Figure 4.34.

The third approach shown promising results in pattern replication, and will be beneficial for manufacturing of metallic/ceramic 3D nano-structures. However, to utilize it successfully for CVD synthesis we will need to find the way how to transfer the patterned catalyst on support substrate. That could be solved by finding the right gluing agent or by the deposition of thick (more than 100 microns) alumina layer.

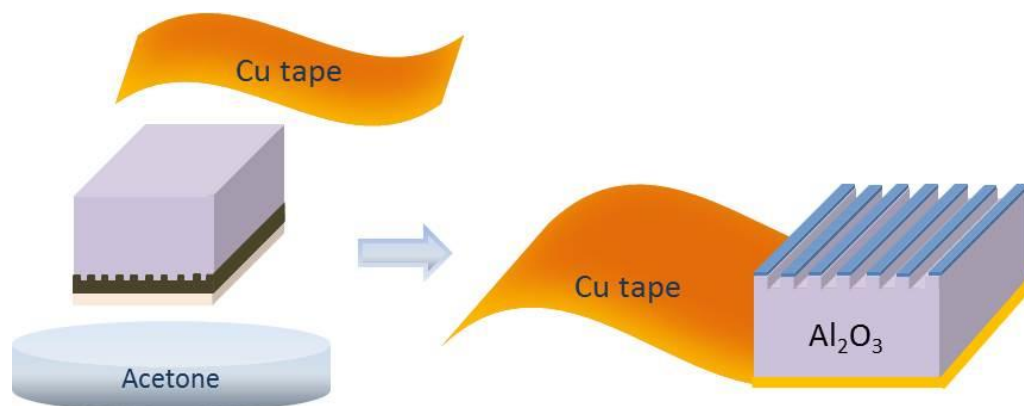


Figure 4.33. Schematic of lift-of (separation) process for approach 3.

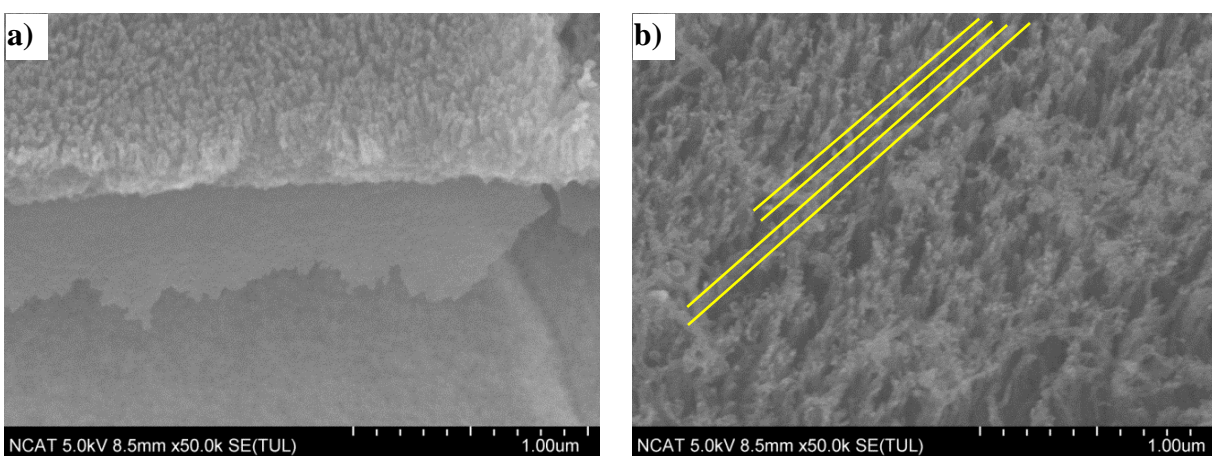


Figure 4.34. CNTs on 70nm lines: a) – side view; b) – top view.

4.6 Carbon Nanotube Grown on Patterned Catalyst

4.6.1 Synthesis of CNT patterns. The CNTs were synthesized at General Nano LLC, the Company is an industrial partner in current research work. The “standard” process recipe for EasyTube™ 3000EXT CVD system was used (details provided in section 3.3). The examples of CNT arrays grown on for a short, 5 minutes synthesis time are presented in Figures 4.35-4.37. As discussed in section 4.5 the CNT patterns grown in “negative” for approach #1 and “positive” for approach #2 replicas. The large areas of uniformly patterned CNT arrays were observed, which is nice evidence that high-quality catalyst patterns were produced in a size below 1 micron. The high-resolution images indicate that individual CNT inside pattern area grown at different rates:

some are short and others 10 times longer and curved without support from neighbors Figure 4.37 and Figure 4.42. This can explain why the wavy CNTs arrays were observed for long-time CVD synthesis and difficulties to detect the pattern of long CNT arrays with the small spacing of pattern Figure 4.38 and Figure 4.39.

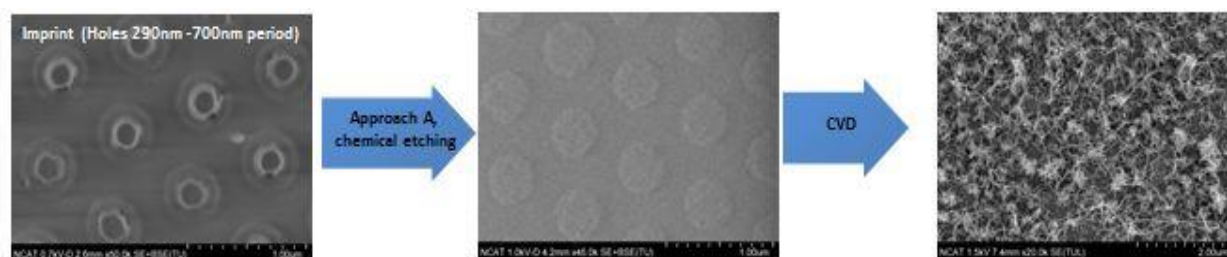


Figure 4.35. SEM images of short CNTs arrays fabricated by first approach with the catalyst patterned by stamp with holes of 290 nm diameter.

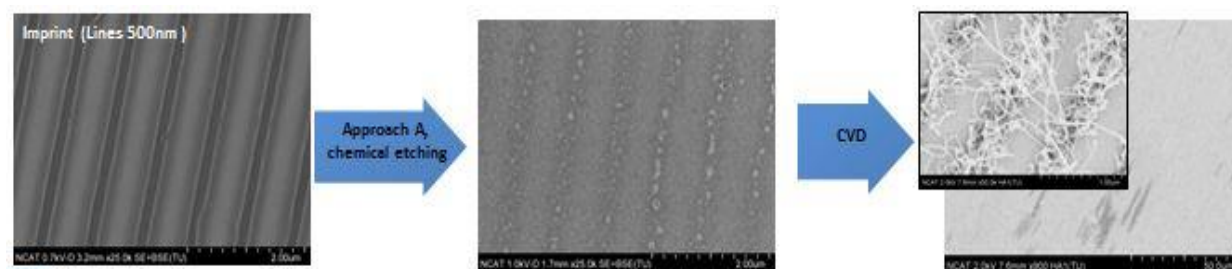


Figure 4.36. SEM images of short CNTs arrays fabricated by first approach with the catalyst patterned by stamp with lines of 500 nm width.

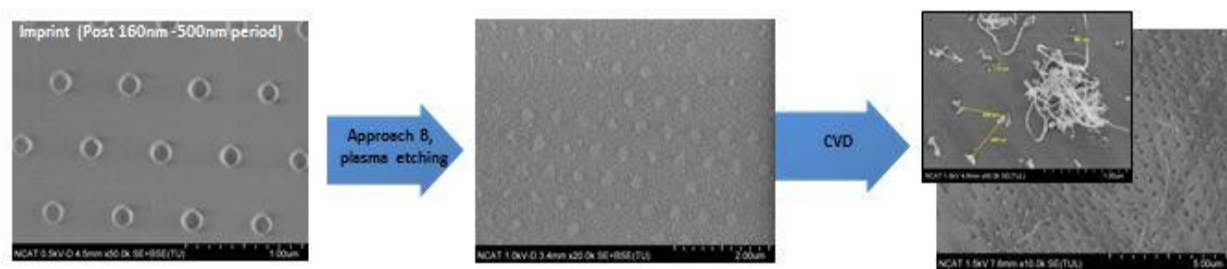


Figure 4.37. SEM images of short CNTs arrays fabricated by second approach with the catalyst patterned by stamp with dots of 160 nm diameter.

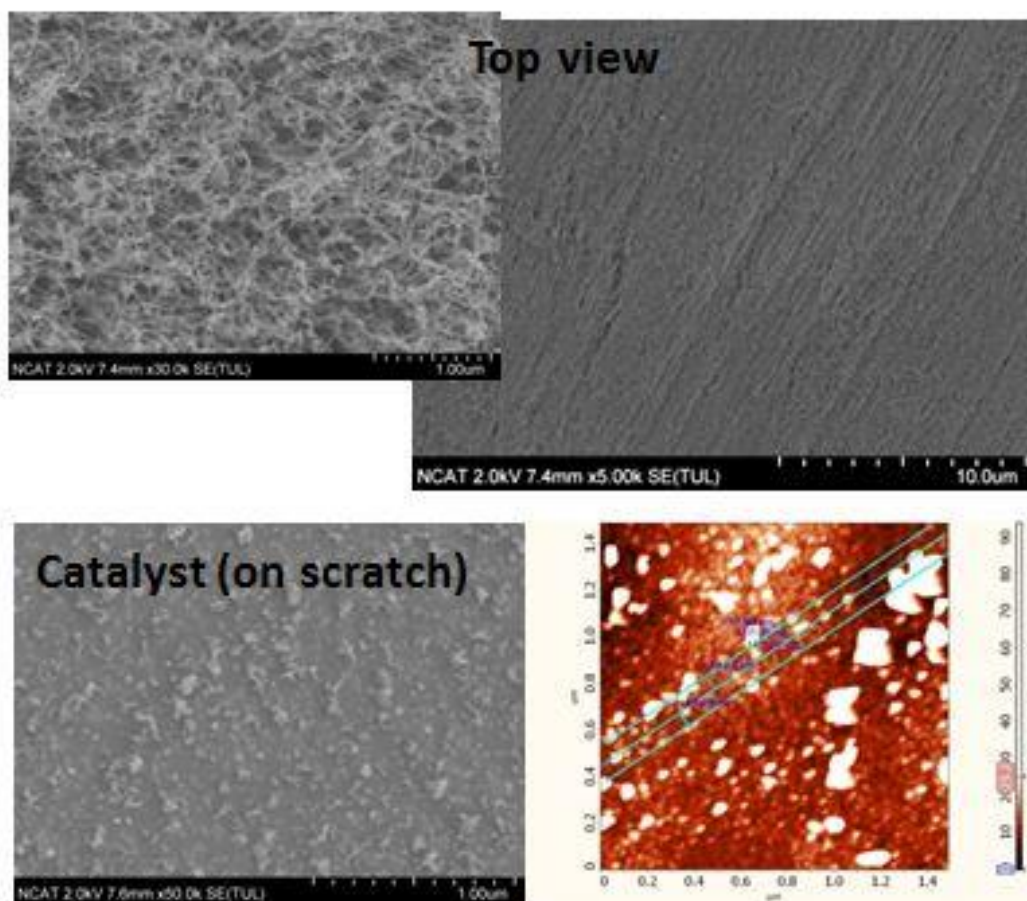


Figure 4.38. SEM images of long CNTs arrays fabricated by first approach with the catalyst patterned by stamp with lines of 70 nm width, 140 nm pattern period.

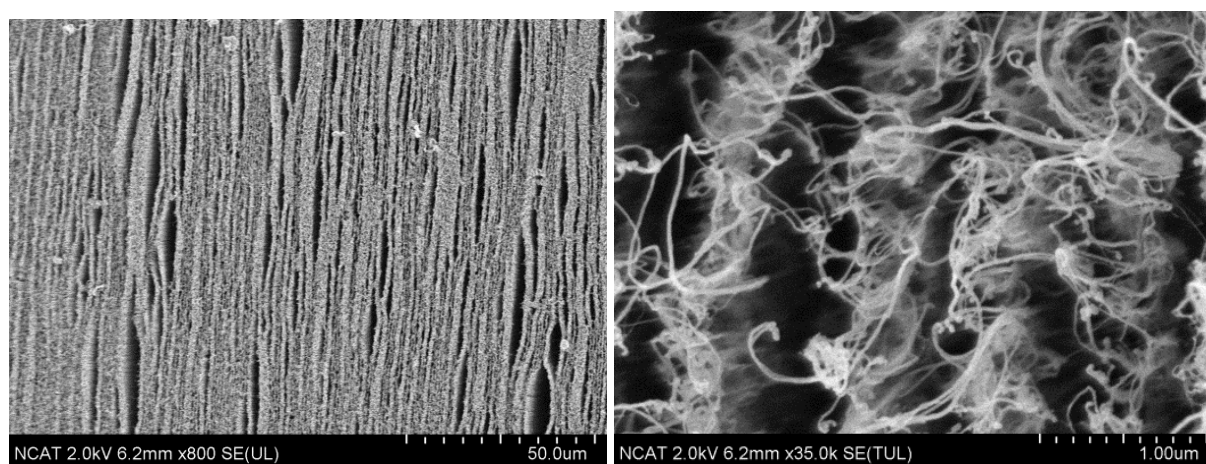


Figure 4.39. SEM images of long CNTs arrays fabricated by second approach with the catalyst patterned by stamp with lines of 455 nm width, 843 nm pattern period.

4.6.2 Characterization of CNT patterns. The SEM imaging and Raman analysis were used to characterize the patterned CNT arrays. The SEM images show the CNT distribution and quality of a pattern. It is also used to estimate diameter of CNT and straightness of arrays. Figure 4.40 presents the HR-SEM images of individual CNTs. It was observed that the individual CNTs have diameter around 20 nm. The quality of CNTs depends on CVD synthesis parameters such as: gas compositions, flow rates, temperature, and catalyst preprocessing regime. The tuning of CVD process was conducted by research group in UC and General Nano and out of scope of this dissertation.

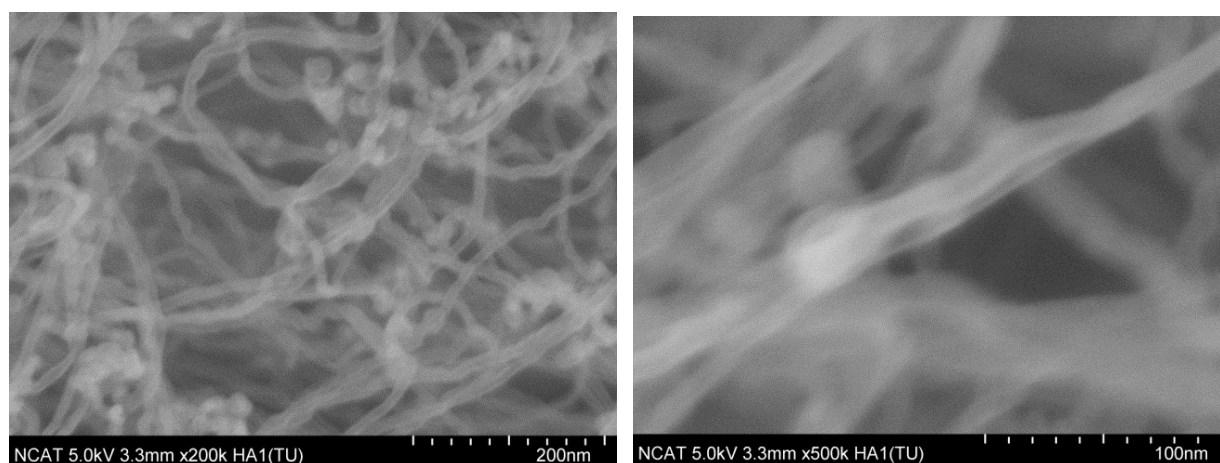


Figure 4.40. HR-SEM images of individual CNTs.

The Raman spectra confirmed the results obtained by SEM analysis. As shown in Figure 4.41 the presence of D and G bands are the same for patterned and reference sample. The I_D/I_G ratio varies from 0.6-0.9 which corresponds to the multiwall CNTs. There was no significant difference between the quality of patterned and reference samples.

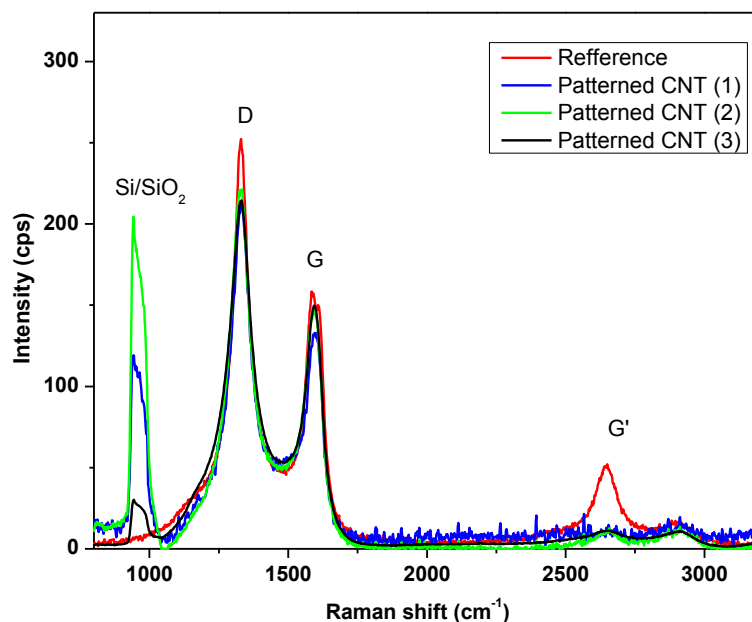


Figure 4.41. Raman spectra of reference and patterned CNT arrays.

The AFM study of patterned CNT array was conducted for the short CNTs and for some samples with long CNTs removed from a substrate to reveal the catalyst structure after CVD synthesis. The non-contact (tapping) mode was used to conduct the measurements, the Si tip NSG10 from NT-MDT with the tip curvature radius of 6 nm were used. In general, the AFM images in a good agreement with the results of SEM analysis (Figure 4.42 and Appendix D).

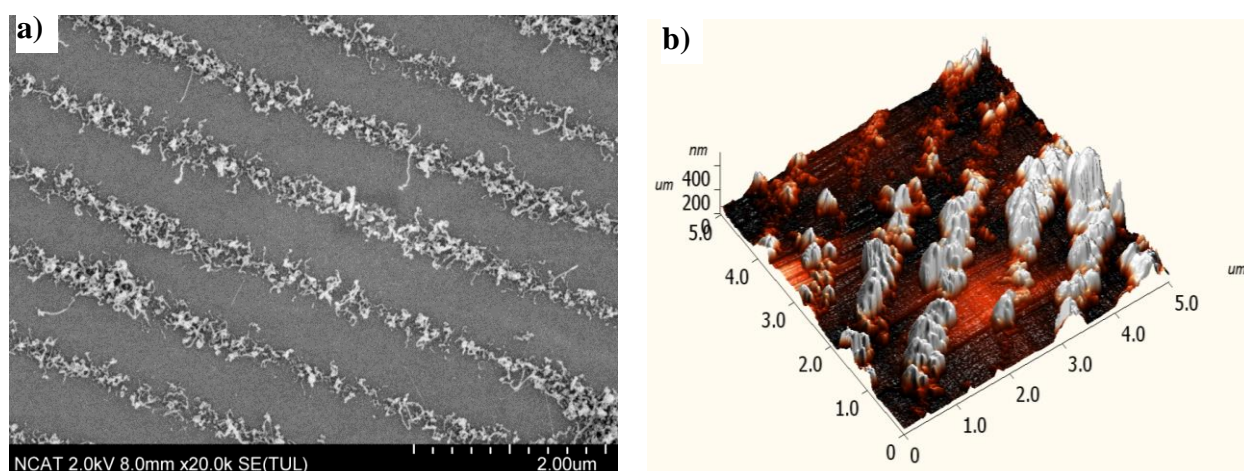


Figure 4.42. SEM (a) and AFM (b) images of CNT pattern.

The additional Scanning Tunneling mode of NT-MDT system was used to estimate the electrical properties of patterned sample. Even the results are hard to interpret since the electrical properties of bulk materials are not valid for the nano-scale model. However, the STM image shows the raising tunneling current peaks on lines where CNTs grown. The STM mode allows detecting the atomic structure of individual CNT, but limited to the size of individual tube and requiring the flat sample with the height no more than couple nanometers.

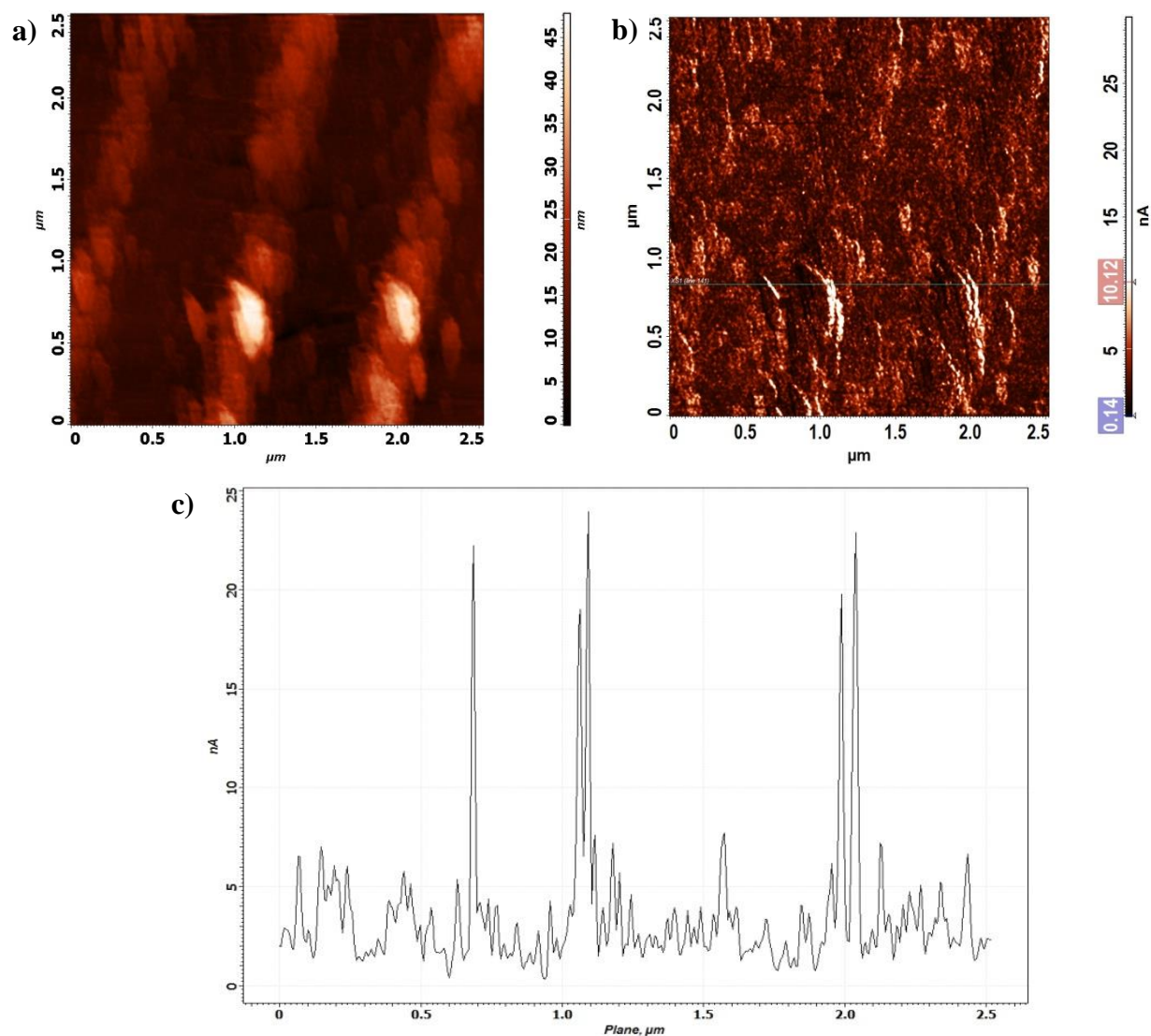


Figure 4.43. STM scan of CNT pattern a) height mode; b) I-low mode and C) I-profile on a scan.

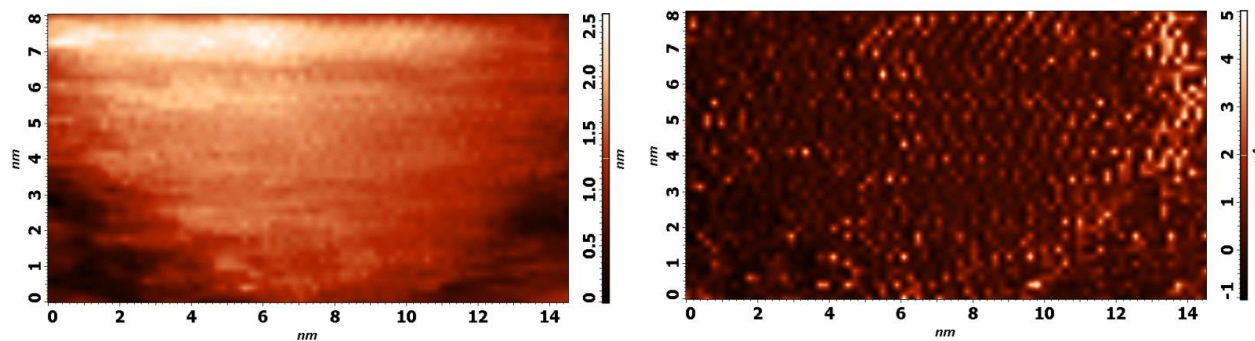


Figure 4.44. Carbon atoms on a single CNT scan.

The summary of all three process approaches presented in Table 4.3. All three approaches had shown the promising results in terms of growing aligned CNTs arrays with the pattern size below 1 micron. The approach #1 shown better repeatability than others, but the chemical etching process require extra safety and environmental precaution and add extra production time and cost to the final product. Approach #2 benefited from absence of chemical etching step, still the exact pattern transfer was not archived due to isotopic plasma etching process and the shadow effect of magnetron sputtering deposition also reduce the quality of the process. Both process' approaches can be significantly improved by using zero-residual layer imprint parameters that will require a special stamp-substrate aligning tool and further investigation of thermal resists rheological properties for accurate imprint process modeling. Finally, the third approach gave outstanding results in a pattern transfer, still the solution for the sample manipulation to be found. The current one – using the copper tape still can be used for production of 3-D nanostructures, such as metals and/or ceramics tubes, lines and porous membranes.

Table 4.3.

Summary of three process approaches.

	Process approach #		
	1	2	3
Number of process steps	5	4	3
Replication of master mold	positive	negative	positive
Benefits	<ul style="list-style-type: none"> ✓ highly repeatable process; ✓ no shadow effect 	<ul style="list-style-type: none"> ✓ no wet-chemistry, so less materials required for process 	<ul style="list-style-type: none"> ✓ exact size replication; ✓ no plasma-etching step and easy lift-off procedure.
Challenges	<ul style="list-style-type: none"> ✓ extra process step; ✓ required wet chemical etching agents and extra safety precautions; ✓ variation of pattern dimensions from stamp due to isotropy of plasma etching process; ✓ over curing of resist during plasma processing and as a result stip lift-off process 	<ul style="list-style-type: none"> ✓ variation of pattern dimensions from stamp due to isotropy of plasma etching process; ✓ variation of pattern replication due to a shadow effect of MS deposition - the catalyst deposited on a wall of a pattern and removed during lift-off procedure; 	<ul style="list-style-type: none"> ✓ the major problem is transfer the pattern on a support substrate

CHAPTER 5

Conclusions and Future Work

This chapter summarizes the results of the presented research work. The recommendations and suggestions for future work are also discussed.

5.1 Conclusions

New fabrication process for catalyst patterning based on combination of nano-imprint lithography, magnetron sputtering and reactive etching techniques was proposed and studied.

The process parameters were defined and optimized for each technology used in samples manufacturing. The deposition rates of alumina and catalyst metals were determined. The optimum working pressure was determined to produce smooth alumina. The effect of deposition pressure and substrate biasing of catalyst particles distribution was studied. The spin-curves and imprint temperature and time were evaluated for two thermal resist materials. The reactive plasma etching rates of thermal resists were determined.

Catalyst patterns of lines, dots and holes ranging from 70 nm to 500 nm were produced and characterized using AFM and SEM.

Vertically aligned CNTs were successfully grown on patterned catalyst using chemical vapor deposition. The produced CNTs arrays repeat the pattern of catalyst and maintain the same quality as synthesized on a regular catalyst substrates.

Finally, the different process approaches/flows were evaluated to determine the best way to scale the lab production to the manufacturing level.

This research works shows that by selecting the appropriate combination of technologies and maintaining the process controls at each step gives a possible solution to manipulate with the shape of CNTs arrays, sizing them to the required dimensions and place them on specified

location. The present study is expected to help better understand the potential of NIL technology in manipulation of the matter on nano-scale level. In summary, these obtained results will undoubtedly play a significant role in the fabrication of novel devices for biosensors in the near future.

5.2 Recommendations for Future Research

Overall, the results presented in this research work do complement the efforts geared towards the development of nano-sized CNT – based devices. However, there are some aspects that require further investigation and possible process improvements that can be realized.

The aligning of patterned CNT arrays can be improved by post-processing such as thermal or chemical treatment. That will be the logical continuation of presented research as much as study of electrical, mechanical and optical properties of produced arrays.

Approach #3 required solution for sample manipulation and pattern transfer on a rigid conductive substrate. Obviously, the third process approach should be exploited for the production of ceramic/metallic 3D nano-structures.

References

- Ago, H., Komatsu, T., Ohshima, S., Kuriki, Y., & Yumura, M. (2000). Dispersion of metal nanoparticles for aligned carbon nanotube arrays. *Applied Physics Letters*, 77(1).
- Allen, B. L., Kichambare, P. D., & Star, A. (2007). Carbon nanotube field-effect-transistor-based biosensors. *Advanced Materials*, 19(11), 1439-1451.
- Arribas, A. S., Bermejo, E., Chicharro, M., Zapardiel, A., Luque, G. L., Ferreyra, N. F., & Rivas, G. A. (2006). Analytical applications of a carbon nanotubes composite modified with copper microparticles as detector in flow systems. *Analytica Chimica Acta*, 577(2), 183-189.
- Balla, T., Spearing, S. M., & Monk, A. (2008). An assessment of the process capabilities of nanoimprint lithography. *Journal of Physics D-Applied Physics*, 41(17).
- Bitirim, V. C., Kucukayan-Dogu, G., Bengu, E., & Akcali, K. . (2013). Patterned carbon nanotubes as a new three-dimensional scaffold for mesenchymal stem cells. *Materials Science and Engineering: C*, 33(5), 3054-3060.
- Bogue, Robert. (2005). Developments in biosensors – where are tomorrow's markets? *Sensor Review*, 25(3), 180-184.
- Cevc, G., & Vierl, U. (2010). Nanotechnology and the transdermal route: A state of the art review and critical appraisal. *J Control Release*, 141(3), 277-299.
- Chai, S.-P., Zein, S. H. , & Mohamed, A. R. (2007). The effect of reduction temperature on Co-Mo/Al₂O₃ catalysts for carbon nanotubes formation. *Applied Catalysis A: General*, 326(2), 173-179.

- Chai, S.-P., Liu, W.-W., Lee, K.-Y., Yeoh, W.-M., Sivakumar, V. M., & Mohamed, A. R. (2009). Effect of FeOx loaded on CoOx/Al₂O₃ catalyst for the formation of thin-walled carbon nanotubes. *Materials Letters*, 63(16), 1428-1430.
- Chen, J., Bao, J. C., & Cai, C. X. (2003). Fabrication, characterization and electrocatalysis of an ordered carbon nanotube electrode. *Chinese Journal of Chemistry*, 21(6), 665-669.
- Chesnokov, V. V., Zaikovskii, V. I., Chichkan, A. S., & Buyanov, R. A. (2009). The role of molybdenum in Fe–Mo–Al₂O₃ catalyst for synthesis of multiwalled carbon nanotubes from butadiene-1,3. *Applied Catalysis A: General*, 363(1–2), 86-92.
- Choong, C.-L., Bendall, J. S., & Milne, W. I. (2009). Carbon nanotube array: A new MIP platform. *Biosensors and Bioelectronics*, 25(3), 652-656.
- Chowdhury, R., Adhikari, S., & Mitchell, J. (2009). Vibrating carbon nanotube based biosensors. *Physica E: Low-dimensional Systems and Nanostructures*, 42(2), 104-109.
- Cremer, R., Witthaut, M., Neuschütz, D., Erkens, G., Leyendecker, T., & Feldhege, M. (1999). Comparative characterization of alumina coatings deposited by RF, DC and pulsed reactive magnetron sputtering. *Surface and Coatings Technology*, 120-121, 213-218.
- Deck, C. P., & Vecchio, K. (2006). Prediction of carbon nanotube growth success by the analysis of carbon–catalyst binary phase diagrams. *Carbon*, 44(2), 267-275.
- Depla, D., Tomaszewski, H., Buyle, G., & De Gryse, R. (2006). Influence of the target composition on the discharge voltage during magnetron sputtering. *Surface and Coatings Technology*, 201(3-4), 848-854.
- Depla, D., Mahieu, S., & De Gryse, R. (2009). Magnetron sputter deposition: Linking discharge voltage with target properties. *Thin Solid Films*, 517(9), 2825-2839.

- Di, J. T., Yong, Z. Z., Yang, X. J., & Li, Q. W. (2011). Structural and morphological dependence of carbon nanotube arrays on catalyst aggregation. *Applied Surface Science*, 258(1), 13-18.
- Dresselhaus, M. S., Dresselhaus, G., & Saito, R. (1995). Physics of carbon nanotubes. *Carbon*, 33(7), 883-891.
- Dresselhaus, M. S., Dresselhaus, G., Jorio, A., Souza, A. G., Pimenta, M. A., & Saito, R. (2002). Single nanotube Raman spectroscopy. *Accounts of Chemical Research*, 35(12), 1070-1078.
- Dresselhaus, M. S., Dresselhaus, G., Charlier, J. C., & Hernandez, E. (2004). Electronic, thermal and mechanical properties of carbon nanotubes. *Philos Transact A Math Phys Eng Sci*, 362(1823), 2065-2098.
- Dresselhaus, M. S., Dresselhaus, G., Saito, R., & Jorio, A. (2005). Raman spectroscopy of carbon nanotubes. *Physics Reports-Review Section of Physics Letters*, 409(2), 47-99.
- Dresselhaus, M. S., Jorio, A., & Rabin, O. (2006). Carbon nanotubes. *Nanoeng. Struct., Funct., Smart Mater.*, 57-97.
- Dresselhaus, M. S., Dresselhaus, G., & Jorio, A. (2007). Raman Spectroscopy of Carbon Nanotubes in 1997 and 2007. *The Journal of Physical Chemistry C*, 111(48), 17887-17893.
- Dresselhaus, M.S., & Dai, H. (2004). Carbon Nanotubes: Continued Innovations and Challenges. *MRS Bulletin*, 29(04), 237-243.
- Gao, M., Dai, L. M., & Wallace, G. G. (2003). Biosensors based on aligned carbon nanotubes coated with inherently conducting polymers. *Electroanalysis*, 15(13), 1089-1094.

- Goldstein, J. (2003). *Scanning Electron Microscopy and X-Ray Microanalysis*: Kluwer Academic/Plenum Publishers.
- Grigorescu, A. E., & Hagen, C. W. (2009). Resists for sub-20-nm electron beam lithography with a focus on HSQ: state of the art. *Nanotechnology*, 20(29).
- Handbook of Nanotechnology*. (2007). (B. Bhushan Ed. 2 ed.): Springer.
- Hart, A. J., Tawfick, S., De Volder, M. F. L., Copic, D., Park, S. J., Oliver, C. R., . . . Roberts, M. J. (2012). Engineering of micro- and nanostructured surfaces with anisotropic geometries and properties. *Adv. Mater.* , 24(13), 1628–1674.
- Hart, A. J., Tawfick, S., De Volder, M. F. L., & Baughman, R. H. . (2013a). Carbon Nanotubes: Present and Future Commercial Applications. *Science*, 339(535).
- Hart, A. J., Tawfick, S., De Volder, M. F. L., Copic, D., Park, S. J., Oliver, C. R., . . . Roberts, M. J. (2013b). Mechanics of Capillary Forming of Aligned Carbon Nanotube Assemblies. *ACS Appl Mater Interfaces*.
- Hartney, M. A., Greene, W. M., Soane, D. S., & Hess, D. W. (1988). Mechanistic studies of oxygen plasma etching. *Journal of Vacuum Science & Technology A*, 6(5).
- Hitachi. (2012). SU8000 Detector System: Variety of Signal Detection System (pp. 1). North Carolina: Hitachi.
- Hwang, S. Y., Jung, H. Y., Yang, K. Y., Jeong, J. H., Choi, K. W., & Lee, H. (2008). Characterization of etch resistance property of imprinting resin. *Electronic Materials Letters*, 4(3), 141-145.
- Iijima, Sumio. (1991). Helical microtubules of graphitic carbon. *Nature (London)*, 354(6348), 56-58.

- Kim, Y. S., Lee, K., Lee, J. S., Jung, G. Y., & Kim, W. B. (2008). Nanoimprint lithography patterns with a vertically aligned nanoscale tubular carbon structure. *Nanotechnology*, *19*(36).
- Krevelen, D.W. van. (1990). *Physical Properties of Polymers*: Elsevier.
- Krinsley, D.H., Pye, K., Sam Boggs, J., & Tovey, N.K. (2005). *Backscattered Scanning Electron Microscopy And Image Analysis of Sediments And Sedimentary Rocks*: Cambridge University Press.
- Kunadian, I., Andrews, R., Qian, D., & Pinar Menguc, M. (2009). Growth kinetics of MWCNTs synthesized by a continuous-feed CVD method. *Carbon*, *47*(2), 384-395.
- Lamouroux, E., Serp, P., & Kalck, P. (2007). Catalytic Routes Towards Single Wall Carbon Nanotubes. *Catalysis Reviews: Science & Engineering*, *49*(3), 65p.
- Li, G., Liao, J. M., Hu, G. Q., Ma, N. Z., & Wu, P. J. (2005, Apr 15). *Study of carbon nanotube modified biosensor for monitoring total cholesterol in blood*.
- Liu, Y. M., Sung, Y., Chen, T. T., Wang, H. T., & Ger, M. D. (2007). Low temperature growth of carbon nanotubes by thermal chemical vapor deposition using non-isothermal deposited Ni-P-Pd as co-catalyst. *Materials Chemistry and Physics*, *106*(2-3), 399-405.
- Minot, E. D., Janssens, A. M., Heller, I., Heering, H. A., Dekker, C., & Lemay, S. G. (2007). Carbon nanotube biosensors: The critical role of the reference electrode. *Applied Physics Letters*, *91*(9).
- Muguruma, H., & Kase, Y. (2006). Structure and biosensor characteristics of complex between glucose oxidase and plasma-polymerized nanothin film. *Biosensors & Bioelectronics*, *22*(5), 737-743.

- Nanotechnology: A Realistic Market Assessment. (2012). *PR Newswire*. Retrieved from <http://search.proquest.com/docview/1095634563?accountid=12711>
- Nasibulin, A. G., Pikhitsa, P. V., Jiang, H., & Kauppinen, E. I. (2005). Correlation between catalyst particle and single-walled carbon nanotube diameters. *Carbon*, *43*(11), 2251-2257.
- National Nanotechnology Initiative's Budget Brief for FY 2013*. (2012). <http://www.nano.gov/node/750>.
- Noda, S., Sugime, H., Osawa, T., Tsuji, Y., Chiashi, S., Murakami, Y., & Maruyama, S. (2006). A simple combinatorial method to discover Co–Mo binary catalysts that grow vertically aligned single-walled carbon nanotubes. *Carbon*, *44*(8), 1414-1419.
- NT-MDT. (2012). Semicontact Mode. Retrieved 5/4/12, from <http://www.ntmdt.com/spm-principles/view/afm>
- Ohring, Milton. (2002). *Materials science of thin films : deposition and structure* (2nd ed.). San Diego, CA: Academic Press.
- Okada, M., Nakamatsu, K., Iwasa, M., Kanda, K., Haruyama, Y., & Matsui, S. (2009). Room Temperature Nanoimprinting Using Release-Agent Spray-Coated Hydrogen Silsesquioxane. *Applied Physics Express*, *2*(1).
- Pérez-Cabero, M., Romeo, E., Royo, C., Monzón, A., Guerrero-Ruiz, A., & Rodríguez-Ramos, I. (2004). Growing mechanism of CNTs: a kinetic approach. *Journal of Catalysis*, *224*(1), 197-205.
- Perez Toralla, K., De Girolamo, J., Truffier-Boutry, D., Gourgon, C., & Zelsmann, M. (2009). High flowability monomer resists for thermal nanoimprint lithography. *Microelectronic Engineering*, *86*(4-6), 779-782.

- Posadowski, W. M., Wiatrowski, A., Dora, J., & Radzimski, Z. J. (2008). Magnetron sputtering process control by medium-frequency power supply parameter. *Thin Solid Films*, 516(14), 4478-4482.
- Pumera, M., Merkoci, A., & Alegret, S. (2007). Carbon nanotube detectors for microchip CE: Comparative study of single-wall and multiwall carbon nanotube, and graphite powder films on glassy carbon, gold, and platinum electrode surfaces. *Electrophoresis*, 28(8), 1274-1280.
- Rahman, M. M., Umar, A., & Sawada, K. (2009). Development of amperometric glucose biosensor based on glucose oxidase co-immobilized with multi-walled carbon nanotubes at low potential. *Sensors and Actuators B-Chemical*, 137(1), 327-333.
- Rao, A. M., Jorio, A., Pimenta, M. A., Dantas, M. S. S., Saito, R., Dresselhaus, G., & Dresselhaus, M. S. (2000). Polarized Raman study of aligned multiwalled carbon nanotubes. *Physical Review Letters*, 84(8), 1820-1823.
- Reimer, L. (1998). *Scanning Electron Microscopy: Physics of Image formation and microanalysis*: Springer.
- Research and Markets Adds Report: Global Carbon Nanotube Market 2011-2015. (2012). *Health & Beauty Close - Up*.
- Roy, S., & Gao, Z. Q. (2009). Nanostructure-based electrical biosensors. *Nano Today*, 4(4), 318-334.
- Sadezky, A., Muckenhuber, H., Grothe, H., Niessner, R., & Pöschl, U. (2005). Raman microspectroscopy of soot and related carbonaceous materials: Spectral analysis and structural information. *Carbon*, 43(8), 1731-1742.

- Sato, K., Saito, R., Oyama, Y., Jiang, J., Cancado, L. G., Pimenta, M. A., . . . Dresselhaus, M. S. (2006). D-band Raman intensity of graphitic materials as a function of laser energy and crystallite size. *Chemical Physics Letters*, *427*, 117-121.
- Scheer, H. C., Bogdanski, N., Wissen, M., & Möllenbeck, S. (2008). Imprintability of polymers for thermal nanoimprint. *Microelectronic Engineering*, *85*(5–6), 890-896.
- Scheerlinck, S., Dubruel, P., Bienstman, P., Schacht, E., Van Thourhout, D., & Baets, R. (2009). Metal Grating Patterning on Fiber Facets by UV-Based Nano Imprint and Transfer Lithography Using Optical Alignment. *Journal of Lightwave Technology*, *27*(10), 1417-1422.
- Schvartzman, M., & Wind, S. J. (2009). Robust Pattern Transfer of Nanoimprinted Features for Sub-5-nm Fabrication. *Nano Letters*, *9*(10), 3629-3634.
- Simon, Y. C., Moran, I. W., Carter, K. R., & Coughlin, E. B. (2009). Silylcarborane acrylate nanoimprint lithography resists. *ACS Appl Mater Interfaces*, *1*(9), 1887-1892.
- Singh, I., Rehni, A. K., Kumar, P., Kumar, M., & Aboul-Enein, H. Y. (2009). Carbon nanotubes: synthesis, properties and pharmaceutical applications. *Fullerenes, Nanotubes, Carbon Nanostruct.*, *17*(4), 361-377.
- Srivastava, P., Malviya, R., Dhamija, K., Gupta, S., & Sharma, P. K. (2010). Nanotechnology: Application and Market. *Drug Invention Today*, *2*(5), 254-257.
- Supplement to the President's 2014 Budget Request*. (2013). www.nano.gov: National Nanotechnology Initiative.
- Trojanowicz, M. (2006). Analytical applications of carbon nanotubes: a review. *Trac-Trends in Analytical Chemistry*, *25*(5), 480-489.

- Truffier-Boutry, D., Galand, R., Beaurain, A., Francone, A., Pelissier, B., Zelsmann, M., & Boussey, J. (2009). Mold cleaning and fluorinated anti-sticking treatments in nanoimprint lithography. *Microelectronic Engineering*, 86(4-6), 669-672.
- Vashist, S. K., Zheng, D., Al-Rubeaan, K., Luong, J. H. T., & Sheu, F.-S. (2011). Advances in carbon nanotube based electrochemical sensors for bioanalytical applications. *Biotechnology Advances*, 29(2), 169-188.
- Wang, X. J., Flicker, J. D., Lee, B. J., Ready, W. J., & Zhang, Z. M. (2009). Visible and near-infrared radiative properties of vertically aligned multi-walled carbon nanotubes. *Nanotechnology*, 20(21).
- Xia, Q. F., Morton, K. J., Austin, R. H., & Chou, S. Y. (2008). Sub-10 nm Self-Enclosed Self-Limited Nanofluidic Channel Arrays. *Nano Letters*, 8(11), 3830-3833.
- Xu, Z., Chen, X., Qu, X. H., Jia, J. B., & Dong, S. J. (2004). Single-wall carbon nanotube-based voltammetric sensor and biosensor. *Biosensors & Bioelectronics*, 20(3), 579-584.
- Yang, W. R., Thordarson, P., Gooding, J. J., Ringer, S. P., & Braet, F. (2007). Carbon nanotubes for biological and biomedical applications. *Nanotechnology*, 18(41).
- Yao, M., Liu, B., Zou, Y. H., Wang, L., Li, D., Cui, T., . . . Sundqvist, B. (2005). Synthesis of single-wall carbon nanotubes and long nanotube ribbons with Ho/Ni as catalyst by arc discharge. *Carbon*, 43(14), 2894-2901.
- Yin, L., Liu, H. , Ding, Y. , Lan, H., & Lu, B. (2009). Fabrication of carbon nanotube arrays for field emission and sensor devices by nanoimprint lithography. *Microelectronics Journal*, 40(3), 604-607.

- Yu, L., Koh, C. G., Lee, L. J., Koelling, K. W., & Madou, M. J. (2002). Experimental investigation and numerical simulation of injection molding with micro-features. *Polymer Engineering & Science*, 42(5), 871-888.
- Yun, Y., Shanov, V., Tu, Y., Schulz, M. J., Yarmolenko, S., Neralla, S., . . . Subramaniam, S. (2006). A multi-wall carbon nanotube tower electrochemical actuator. *Nano Letters*, 6(4), 689-693.
- Yun, Y., Gollapudi, R., Shanov, V., Schulz, M. J., Dong, Z. Y., Jazieh, A., . . . Subramaniam, S. (2007). Carbon nanotubes grown on stainless steel to form plate and probe electrodes for chemical/biological sensing. *Journal of Nanoscience and Nanotechnology*, 7(3), 891-897.
- Yun, Y. H., Shanov, V., Schulz, M. J., Narasimhadevara, S., Subramaniam, S., Hurd, D., & Boerio, F. J. (2005). Development of novel single-wall carbon nanotube-epoxy composite ply actuators. *Smart Materials & Structures*, 14(6), 1526-1532.
- Yun, Y. H., Dong, Z. Y., Shanov, V., Heineman, W. R., Halsall, H. B., Bhattacharya, A., . . . Schulz, M. J. (2007). Nanotube electrodes and biosensors. *Nano Today*, 2(6), 30-37.
- Zarabadi-Poor, P., Badiei, A., Yousefi, A. A., Fahlman, B. D., & Abbasi, A. (2010). Catalytic chemical vapour deposition of carbon nanotubes using Fe-doped alumina catalysts. *Catalysis Today*, 150(1-2), 100-106.
- Zeng, Q., Li, Z., & Zhou, Y. (2006). Synthesis and Application of Carbon Nanotubes. *Journal of Natural Gas Chemistry*, 15(3), 235-246.
- Zhang, X. B., Guo, Q., & Cui, D. (2009). Recent Advances in Nanotechnology Applied to Biosensors. *Sensors*, 9(2), 1033-1053.

Zhu, Z., Song, W., Burugapalli, K., Moussy, F., Li, Y. L., & Zhong, X. H. (2010). Nano-yarn carbon nanotube fiber based enzymatic glucose biosensor. *Nanotechnology*, 21(16), 165501.

Zywitzki, O., & Hoetzsch, G. (1997). Correlation between structure and properties of reactively deposited Al₂O₃ coatings by pulsed magnetron sputtering. *Surface and Coatings Technology*, 94-95, 303-308.

Appendix A

Table A.1.

Stamp inventory.

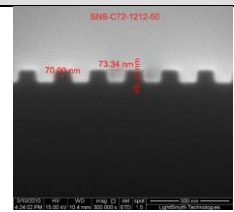
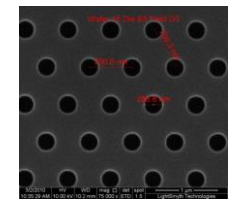
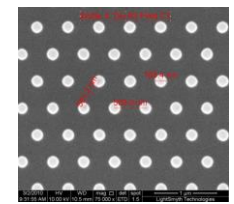
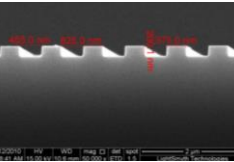
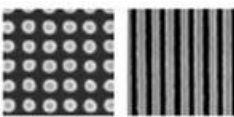
Stamp #	Supplier	Description	Period	Feature size	Height	Pattern area	Image
SNS-C72-2525-50-P	LightSmyth	Line Grating	139nm	69.5nm	50nm	25X25mm	
S2D-24D3-0808-350-P	LightSmyth	Hex holes	700nm	290nm	350nm	8X8mm	
S2D-18C1-0808-350-P	LightSmyth	Hex post	500nm	165nm	350nm	8x8mm	
SNS-C12-2525-200-P	LightSmyth	Line Grating	825nm	375nm	200nm	25x25mm	
P200	Nanonex	Hex Post	500nm	165nm	350nm	8x8mm	
NSSP33	Eulitha	nano-hole and line space array	100nm	35nm	50nm	0.5x0.5mm each	

Table A.2.

Resists and solvents for NIL.

Name	Description
mr-PMMA 100k	thermal resist
Nanonex 1025 2.5%	thermal resist
Nanonex 1025 5.5%	thermal resist
Nanonex 1025 7%	thermal resist
NXT110A&B	mold-release agent
trichloro(perfluorooctyl)-silane	mold-release agent
PGMEA	solvent for nanonex resist
Acetone (SMOS grade)	lift off solvent
ceramic etchant	etchant
Ammonia solution	lift off solvent
Hydrogen peroxide	lift off solvent

Appendix B
X-ray Diffraction Pattern

Pattern: 00-050-0741		Radiation = 1.540598		Quality: Indexed		
γ -Al ₂ O ₃ Aluminum Oxide Also called: γ - Al ₂ O ₃		2θ	i	h	k	l
		19.348	50	1	1	1
		31.855	75	2	2	0
		37.539	90	3	1	1
		39.277	30	2	2	2
		45.668	100	4	0	0
		56.745	50	4	2	2
		60.546	75	5	1	1
		66.602	100	4	4	0
		84.468	30	4	4	4
Lattice: Face-centered cubic		Mol. weight = 101.96				
S.G.: Fd-3m (227)		Volume [CD] = 500.38				
a = 7.93900	Z = 11	Dx = 3.722				
Additional pattern: See 00-010-0425 for additional reflections below 1.146.						
Data collection flag: Ambient.						
Liddell, K., Univ. of Newcastle, Dept. of Mechanical, Materials & Manufacturing Engineering, England, UK., Private Communication (1996)						

Figure B.1. JCPDS data for γ -alumina.

Appendix C

PMMA imprint temperature and time optimisation for stamp S2D-24D3-0808-350-P (holes)

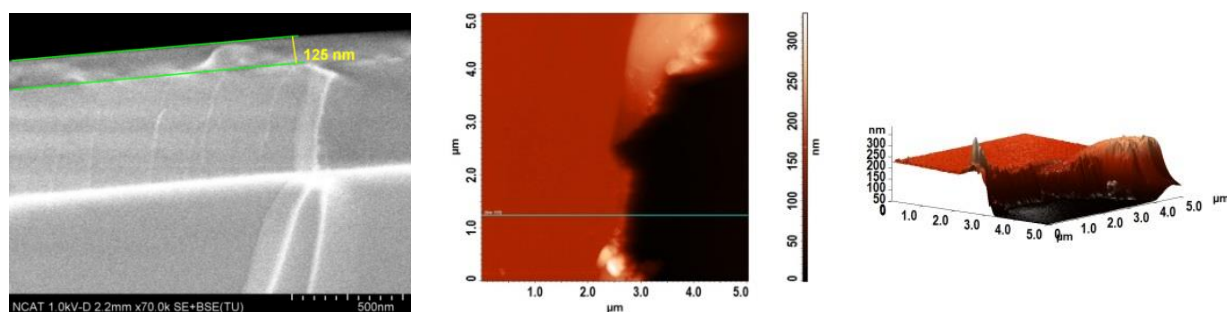


Figure C.1. Initial layer of PMMA resist.

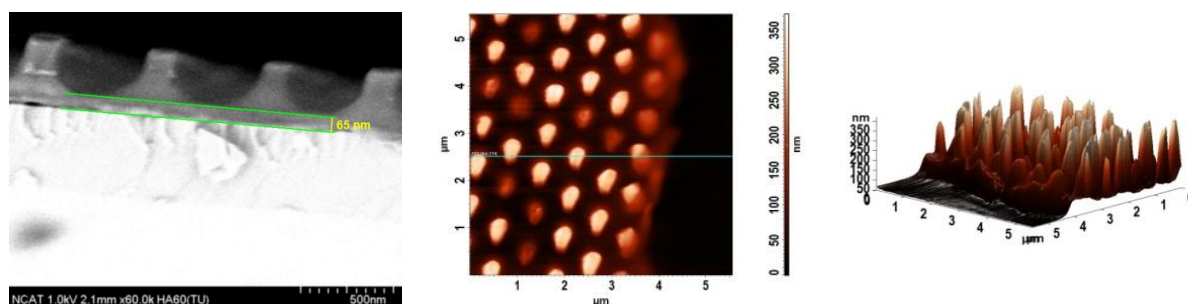


Figure C.2. Cross sectional SEM and AFM scan of imprint at 170°C for 3 minutes.

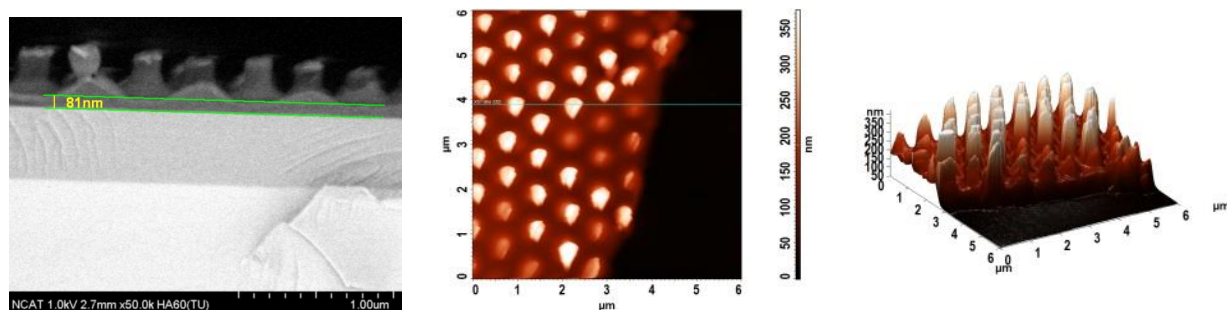


Figure C.3. Cross sectional SEM and AFM scan of imprint at 160°C for 2 minutes.

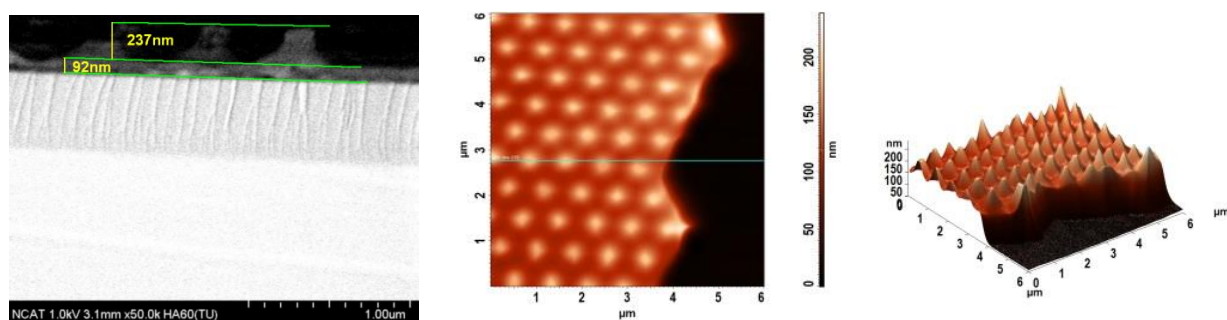
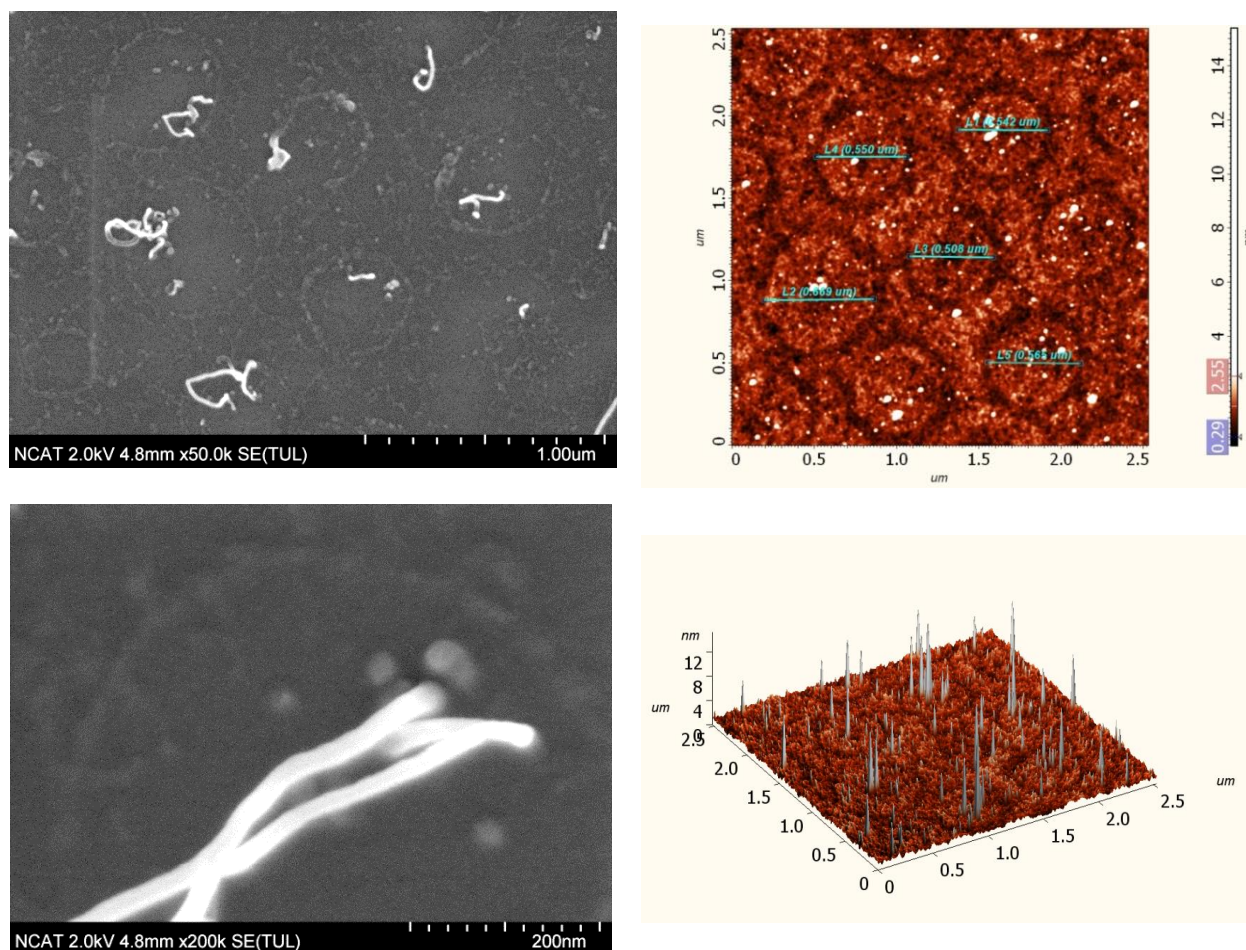


Figure C.4. Cross sectional SEM and AFM scan of imprint at 160°C for 3 minutes.

Appendix D

SEM and AFM images of short CNT patterns



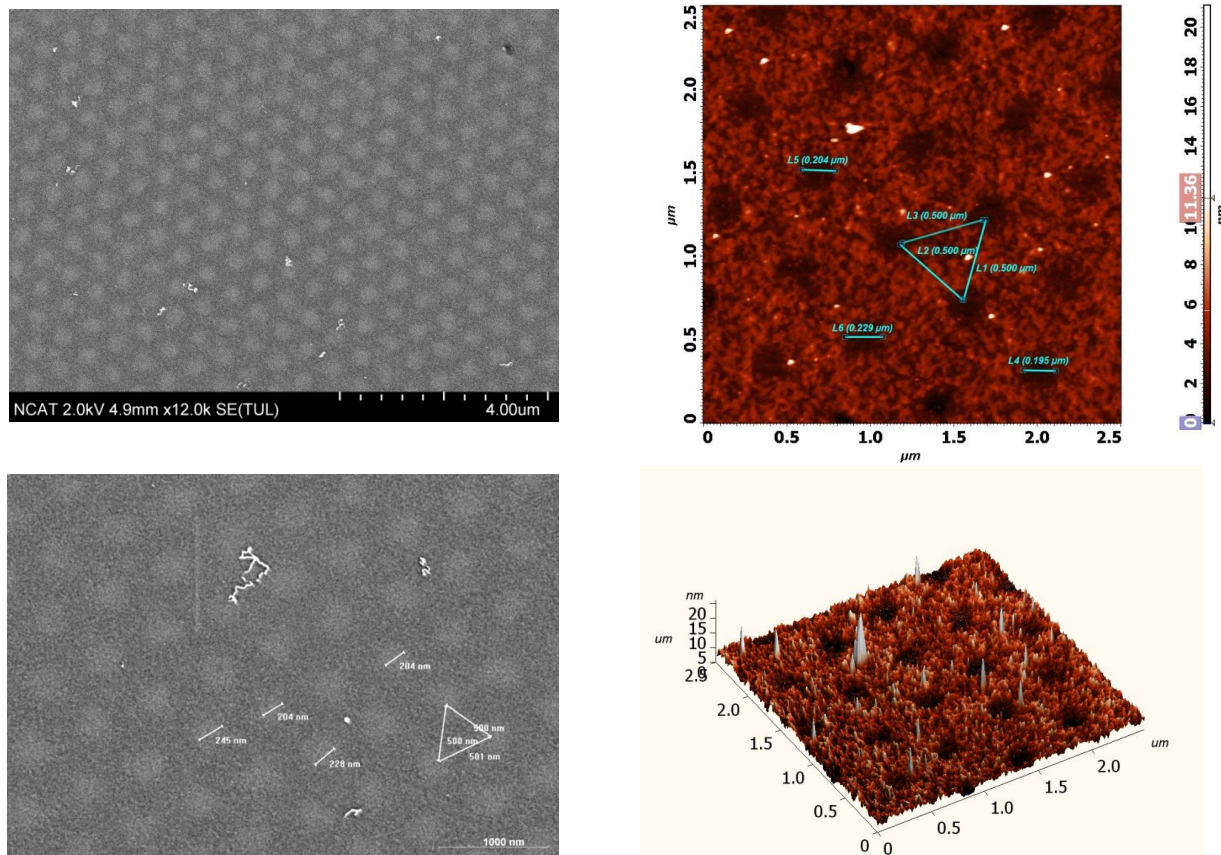


Figure D.2. Sample 11-2, prepared with stamp S2D-18C1-0808-350-P, Approach #1, Chemical etching.